IL-4 Induces CD22 Expression to Restrain the Effector Program of Virtual Memory T Cells

Bin Yang[1], Ophélie Piedfort[1], Guillem Sanchez-Sanchez[2,3,4], Arnaud Lavergne[5], Meijiao Gong[1], Garrie Peng[6,7,8], Ariel Madrigal[9,10], Georgios Petrellis[1], Brunette Katsandegwaza[1], Lucia Rodriguez Rodriguez[1], Alexis Balthazar[1], Sarah J. Meyer[11], Gert Van Isterdael[12,13], Julie Van Duyse[12,13], Fabienne Andris[3], Qiang Bai[14,15], Thomas Marichal[14,16], Bénédicte Machiels[1,16], Lars Nitschke[11], Hamed S. Najafabadi[9,10], Irah L. King[6,7,8], David Vermijlen[2,3,4,16], Benjamin G. Dewals[1,16*]

[1]Department of Infectious and Parasitic Diseases, Faculty of Veterinary Medicine – FARAH, University of Liège, Liège, Belgium.
[2]Department of Pharmacotherapy and Pharmaceutics, Université Libre de Bruxelles (ULB), Brussels, Belgium
[3]Institute for Medical Immunology (IMI), Université Libre de Bruxelles (ULB), Gosselies, Belgium.
[4]ULB Center for Research in Immunology (U-CRI), Belgium.
[5]GIGA-Genomics core facility, University of Liège, Liège, Belgium
[6]Department of Microbiology and Immunology, Meakins-Christie Laboratories, Research Institute of McGill University Health Centre, Montreal, Quebec, Canada
[7]McGill Interdisciplinary Initiative in Infection and Immunity, Montreal, Quebec, Canada
[8]McGill Centre for Microbiome Research, Montreal, Quebec, Canada
[9]Department of Human Genetics, McGill University, Montreal, QC, H3A 0C7, Canada
[10]McGill Genome Centre, Dahdaleh Institute of Genomic Medicine, Montreal, QC, H3A 0G1, Canada
[11]Division of Genetics, Department of Biology, University of Erlangen, 91058 Erlangen, Germany
[12]VIB Flow Core, VIB Center for Inflammation Research, Ghent, Belgium
[13]Department of Biomedical Molecular Biology, Ghent University, Ghent, Belgium.
[14]Laboratory of Immunophysiology, GIGA Institute, ULiège, Liège, Belgium
[15]PhyMedExp, INSERM U1046, University of Montpellier, Montpellier, France
[16]Walloon Excellence in Life Sciences and Biotechnology (WELBIO) Department, WEL Research Institute, Wavre, Belgium.

*corresponding author: bgdewals@uliege.be

One sentence summary

CD22 regulates IL-4-induced expansion and responsiveness of virtual memory T cells during helminth infection.

Abstract

Parasitic helminths induce the production of interleukin (IL)-4 which causes the expansion of virtual memory $CD8^+$ T cells (T_{VM}), a cell subset that contributes to the control of coinfection with intracellular pathogens. However, the mechanisms regulating IL-4-dependent T_{VM} activation and expansion remain ill-defined. Here we used single-cell RNA sequencing of $CD8^+$ T cells to discover pathways that control IL-4-dependent T_{VM} responses. Gene signature analysis of $CD8^+$ T cells identified a cell cluster marked by CD22, a canonical regulator of B cell activation, as a selective surface marker of IL-4-induced T_{VM} cells. $CD22^+$ T_{VM} were enriched for IFN-γ and granzyme A and retained a diverse TCR repertoire, while enriched in self-reactive CDR3 sequences. CD22 intrinsically regulated IL-4-induced $CD8^+$ T cell effector program, resulting in reduced responsiveness of $CD22^+$ T_{VM} and regulatory functions to infection and inflammation. Thus, helminth-induced IL-4 drives the expansion and activation of T_{VM} that is counter-inhibited by CD22.

Introduction

Helminths are widespread parasitic worms responsible for the infection of about a quarter of the human population (*1*). In high burden infections, helminths can induce debilitating and chronic disease with a strong impact on health and welfare (*2*, *3*). However, most helminth infections are of low burden, with a limited number of parasites persisting in their host for several months and even years. Worm persistence can be explained by a finely regulated balance between immune control and evasion to tolerate the parasites, while avoiding critical harm (*4*, *5*). Helminths generally induce a robust and protective type 2 immunity, which is characterized by the production of type 2 cytokines including interleukin (IL)-4, IL-5, and IL-13. Type 2 cytokines are produced by and activate key immune cells such as group 2 innate lymphoid cells (ILC2s), eosinophils, mast cells, macrophages and $CD4^+$ T helper 2 (Th2) cells, which coordinate immune protection (*5*). In addition to these effector mechanisms, helminth infection also induces the expansion of a specific population of memory-phenotype $CD8^+$ T cells in the secondary lymphoid organs that are referred to as virtual memory T cells (T_{VM}) (*6*–*9*).

T_{VM} are memory-phenotype $CD8^+$ T cells that share many characteristics in common with true memory $CD8^+$ T cells (T_{TM}), which arise in the periphery in response to a foreign antigen and are characterized by their ability to develop fast and effective responses after repeated encounters with the same antigen (*10*). Likewise, T_{VM} can also rapidly respond in the early phase of infection with pathogens (*11*–*14*). However, in contrast to T_{TM}, T_{VM} have the particularity to differentiate and develop in absence of foreign antigen (*13*, *15*, *16*). In naive conditions, T_{VM} are $CD8^+$ αβ T cells that are found in substantial proportions in conventionally housed mice, as well as in germ-free (GF) mice (*17*). While T_{VM} exhibit a $CD44^{hi}CD122^+CXCR3^{hi}$ memory phenotype, they differ from T_{TM} since they downregulate the α4 integrin (*Itga4*, CD49d), which is normally upregulated in response to TCR activation (*18*). T_{VM} have been described in human, but there is still a significant lack of specific markers to distinguish them from T_{TM}, in both human and mice (*16*, *19*–*21*). The developmental origin of memory-phenotype T cells in the periphery (i.e. T_{VM}) remains uncertain. In some mouse strains like BALB/c mice, IL-4 producing invariant natural killer (NK) T cells exist in the thymus resulting in the induction of memory-phenotype T cells, named innate memory T cells or T_{IM} (*22*–*24*). Whereas T_{VM} are in the periphery, T_{IM} are induced in the thymus and might contribute to the pool of memory-phenotype T cells in the periphery (*16*). The generation of memory-phenotype T cells have been recently explained by the recognition of self-ligands during maturation in the thymus, driving the upregulation of the transcription factor eomesodermin (EOMES) in T cell precursors (*17*, *25*). Thus, memory-phenotype T cells include both T_{VM} and T_{IM}, by definition.

In addition to self-specificity, T_{VM} differentiation and expansion also requires signals from IL-4 and/or IL-15, depending on the mouse strain (*8*, *16*, *24*, *26*–*28*). Whereas IL-4 or IL-4Rα deficiency results in significantly reduced memory-phenotype T cells in BALB/c mice (*6*, *27*), C57BL/6 mice mainly rely on IL-15 for T_{VM} differentiation and maintenance at steady-state (*8*, *21*, *28*, *29*). Efforts have been made to decipher the development and function of T_{VM} in homeostasis as well as in response to infection or tumor development (*6*, *7*, *17*, *30*–*32*), but the mechanisms regulating helminth-induced T_{VM} expansion, activation and maintenance are yet to be fully uncovered (*6*, *7*, *9*, *30*). Nevertheless, expansion of T_{VM} after helminth infection can result in enhanced $CD8^+$ T cell-mediated control against bystander viral coinfection (*6*), which was also observed in bacterial coinfection (*7*). Thus, the increased numbers of T_{VM} in helminth infection can drive protection against concurrent intracellular pathogens. However, the

mechanisms regulating T_{VM} response to IL-4 during helminth infection remain incompletely defined.

Here, we addressed this question by studying IL-4 signaling and consequences in circulating $CD8^+$ T cells during helminth infection. We employed single-cell RNA sequencing (scRNA-seq) to investigate transcriptomic gene signatures and interrogate cellular heterogeneity to identify unique features of IL-4-induced T_{VM}. Our findings identified a specialized program of differentiation instructed by IL-4 in T_{VM}, including the unanticipated upregulation of CD22, a canonical inhibitory receptor of B lymphocytes. CD22 was upregulated in IL-4-induced self-reactive T_{VM} and CD22 expression resulted in reduced T_{VM} response to IL-4 during helminth infection and regulatory functions against immunopathology.

Results

IL-4Rα is required on peripheral CD8$^+$ T cells for T_{VM} maintenance. To study IL-4-mediated T_{VM} expansion in the periphery, a BALB/c mouse model was generated in which peripheral CD8$^+$ T lymphocytes have impaired expression of the IL-4 receptor α chain (IL-4Rα). Specifically, *E8i^{Cre}* C57BL/6 mice were backcrossed for 9 generations with *Il4ra$^{lox/lox}$* BALB/c mice (WT) to generate IL-4Rα$^{\Delta CD8}$ BALB/c mice. In *E8i^{Cre}* mice, Cre expression is driven through the control of an E8i-CD8α enhancer/promoter construct (*33*). The enhancer E8i is activated in maturating single positive CD8$^+$ T lymphocytes (SP8) before exiting the thymus to the periphery.

In naive conditions, single positive (SP) CD4$^+$ SP4 and CD8$^+$ SP8 expressed similar levels of IL-4Rα (CD124) in both WT and IL-4Rα$^{\Delta CD8}$ mice (**Fig. 1A**). A small subset of CD24$^-$ mature SP8 cells started to lose CD124 expression in IL-4Rα$^{\Delta CD8}$ mice (**Fig. 1B**). Splenic CD3$^+$CD8$^+$ T cells expressed significantly lower levels of CD124 (**Fig. 1C**), whereas CD3$^+$CD8$^-$ T cells and other cell types retained high CD124 expression in IL-4Rα$^{\Delta CD8}$ mice (**Fig. 1C**, **Fig. S1A**). T_{VM} were gated as CD44^{hi}CXCR3$^+$ CD49d^{low}CD3$^+$CD8$^+$ T cells (**Fig. S1B**), and IL-4Rα$^{\Delta CD8}$ mice had significantly less T_{VM} when compared to WT littermate controls (**Fig. 1D**). However, a population of CXCR3$^+$ T_{VM} retained the expression of CD124 in IL-4Rα$^{\Delta CD8}$ mice (**Fig. 1E**), which was confirmed by genotyping (**Fig. S1C-D**). Although T_{VM} were significantly reduced in IL-4Rα$^{\Delta CD8}$ mice, CD124$^+$ cells escaping E8iCre-mediated recombination were enriched in memory-phenotype T cells (**Fig. 1F and Fig. S1E-F**).

Thus, peripheral IL-4 signaling significantly contributes to T_{VM} maintenance, and IL-4Rα$^{\Delta CD8}$ mice are partial knockout in which the remaining T_{VM} population mainly arises from IL-4Rα-expressing CD8$^+$ T cells, escaping genetic deletion driven by the *E8i^{Cre}* transgene.

T_{VM} expansion is reduced in IL-4Rα$^{\Delta CD8}$ mice after IL-4c treatment and helminth exposure. During helminth infection, IL-4 can expand T_{VM} (*6*, *7*). To study the effect of IL-4 signaling on peripheral CD8$^+$ T cells, IL-4Rα$^{\Delta CD8}$ and WT littermate control mice were treated with recombinant IL-4 complexed with a monoclonal antibody to IL-4 (IL-4c), which extends the bioactive half-life of the cytokine and artificially induces an IL-4 dominant environment (**Fig. 1G-I**). Although maturating thymic CD24$^-$ SP8 started to lose CD124, and IL-4c upregulated expression of the transcription factor eomesodermin (EOMES) in SP8, there were no significant difference in CD24$^-$ SP8 proportions or EOMES expression between WT and IL-4Rα$^{\Delta CD8}$ mice (**Fig. 1G**). In the spleen, IL-4c induced the expansion of T_{VM} and upregulated the expression of EOMES in WT mice, while T_{VM} expansion and EOMES expression levels were reduced in IL-4Rα$^{\Delta CD8}$ mice (**Fig. 1H**), confirming significant deletion of the *Il4ra* locus. However, IL-4c treatment increased the proportions of CD124$^+$ CD8$^+$ T cells in IL-4Rα$^{\Delta CD8}$ mice (**Fig. 1I**). When focusing on CXCR3$^+$ T_{VM}, we found that although reduced, a significant proportion of CXCR3$^+$ cells was still present in IL-4Rα$^{\Delta CD8}$ animals. However, the majority of CXCR3$^+$ T_{VM} retained surface expression of CD124 (**Fig. S1G**).

We further explored T_{VM} expansion in IL-4Rα$^{\Delta CD8}$ mice exposed to helminths using injection of *S. mansoni* eggs or infected with the gastro-intestinal nematode *Heligmosomoides polygyrus*. IL-4Rα$^{\Delta CD8}$ mice showed significantly reduced T_{VM} expansion (**Fig. 1J**). Expansion of T_{VM} required IL-4Rα expression by CD8$^+$ T cells, since the majority of T_{VM} in IL-4Rα$^{\Delta CD8}$ mice were found in the CD124$^+$ compartment but significantly lower in CD124$^-$ T cells (**Fig. 1K**), and CD124$^-$ T_{VM} did not expand in response to IL-4c (**Fig. S1H**). However, *H. polygyrus* infection was not affected in IL-4Rα$^{\Delta CD8}$ mice as attested by similar worm burden at day 15 after infection (**Fig. 1L**).

Furthermore, IL-4c treatment resulted in significant early control of the lung replication of a luciferase-expressing viral strain of murid gammaherpesvirus 4 (MuHV-4-Luc) by day 8 after infection (**Fig 1M**), supporting our previous observations (*6*). However, luminescent signals revealing replication levels of MuHV-4-Luc in infected IL-4Rα$^{\Delta CD8}$ mice remained significantly higher than littermate controls.

Together, these data demonstrate that during helminth infection IL-4 directly induces T_{VM} expansion in peripheral CD8$^+$ T cells, impaired in IL-4Rα$^{\Delta CD8}$ mice.

Single-cell transcriptomic analysis reveals peripheral T_{VM} signature. To investigate the transcriptomic program of CD8$^+$ T cell responses to IL-4 during helminth infection, single-cell RNA-seq (scRNA-seq) was performed on CD8$^+$ T cells enriched from the spleen of IL-4Rα$^{\Delta CD8}$ and littermate control WT mice after IL-4c treatment or *H. polygyrus* infection (**Fig. S2A**).

Clustering on the Uniform Manifold Approximation and Projection (UMAP) representation identified 17 distinct clusters (**Fig. 2A, Fig. S2B-C**). Hash tagging allowed separation of cells from individual mice in each dataset to visualize the proportional dispersion of each cluster for each individual mouse (**Fig. S2D**). Based on gene signatures and increased proportions upon IL-4 response, cluster 6 was identified as the cluster in which T_{VM} would be most likely found as memory genes were upregulated and *Itga4* downregulated (**Fig. S2D-F**). To better define the T_{VM} population, SingleR analysis was performed on the same merged datasets to identify naive, memory and effector T cells based on signature genes (**Fig. 2B-C**) (*34*). Cells having a signature of memory or effector T cells were then extracted from the main object and re-analysed with Seurat for clustering (**Fig. 2D-E, Fig. S3A-B**).

In total, 15 clusters were identified and differential gene expression was performed. Cells in cluster 14 expressed genes of terminally effector T cells (*Zeb2, Klrg1, Cx3cr1, Bhlhe40, Gzmb*), while Cluster 1 contained cells upregulating *Gzmm*. Cluster 3 and 4 upregulated genes associated with true memory (*Itga4, Gzmk, Ccl5, Cxcr3)*. Cluster 5 contained cells upregulating *Cd226, Lef1, Ccr9* and *Foxp1.* While cluster 6 upregulated *Ccr7, Il7r* and *Tcf7* and likely includes central memory T cells, the exhaustion gene *Tox* and *Lag3* were differentially upregulated in Cluster 8. Signature genes reminiscent of mucosal associated invariant T cells and/or γδ T cells such as *Cd160*, *Klra7* and *Klrc1*, as well as *Trg-C1*, *Trg-C1* were found in Cluster 9. In addition, *Cd69, Cd83, Icam1* grouped potential tissue resident T cells in Cluster 10, and interferon stimulated genes (*Isg15, Ifit1, Ifit3, Oasl1, Usp18*) were up in Cluster 11. Cluster 12 contained cells in active division potentially representing stem-like memory T cells upregulating *Mki67, Birk5, Ccnb2, Ccna2,* and *Cdk1*. Finally, cluster 2 had a gene signature related to T_{VM}, characterized by the reduced expression of *Itga4* combined with the upregulation of memory/effector genes like *Eomes*, *Ctla2a*, *Ccr2*, *Ccr5*, *Il2rb* and *Gzma* (**Fig. 2D-F**). Confirming that cluster 2 represents T_{VM}, the proportion of cells in cluster 2 was increased upon IL-4c or *H. polygyrus* infection in littermate WT control mice, while less abundant in IL-4Rα$^{\Delta CD8}$ mice (**Fig. S3C-D**).

Thus, transcriptomic heterogeneity of peripheral CD8$^+$ T cell responses to IL-4 was revealed by scRNA-seq analysis, identifying a cluster of cells with T_{VM} gene expression signature.

IL-4-induced T_{VM} upregulate signature genes including *Cd22* during helminth infection. IL-4c and *H. polygyrus* infection enriched memory T cell gene signature with upregulation of *Eomes*, *Cxcr3* and *Il4ra* and reduced *Itga4* (**Fig. 3A-B**), with a more limited effect in IL-4Rα$^{\Delta CD8}$ mice. Trajectory pathway analysis using RNA velocity (*35*) showed main trajectories of differentiation from cluster 0 to clusters 1 and 2, then to cluster 4, 3 and 14 irrespective of the treatment (**Fig. S4A**). These data suggest that T_{VM} cluster 2 originates from memory cluster

0 and that the main pathway of T_{VM} differentiation is conserved upon IL-4 activation. Furthermore, analysis of the regulation of transcription identified cellular stress-associated *Atf6* and *Cebpd* among the top enriched transcription factors expressed in response to IL-4c and *H. polygyrus* (**Fig. S4B**) (*36–39*).

Focusing on the differential gene expression in cluster 2 in response to both IL-4c or *H. polygyrus* infection, we observed a significant upregulation of *Gzma*, *Gzmm*, *Ctla2a, Xcl1, Bcl11b, Fyn, Ccr2, Ccr5* and *Cd22*, whereas *S1pr1, Cd55, Ly6c1, Ly6c2 and Itgb7* were downregulated (**Fig. 3C-D**). Most of the regulated genes were also similarly regulated in data obtained by RNA sequencing on sorted T_{VM} from mice exposed to *S. mansoni* eggs (**Fig. S4C**) (*6*), $CD5^+$ or $CD5^-$ T_{VM} (*21*), and $CCR2^+$ T_{VM} (*14*), further supporting that cluster 2 are T_{VM}. Moreover, differential gene expression analysis in cluster 2 upon IL-4c treatment and at day 15 after *H. polygyrus* infection confirmed the significant increased expression of *Gzma*, *Gzmm*, *Ccr5*, *Xcl1* and *Cd22* (**Fig. 3E**). At day 15 after *H. polygyrus* infection, although frequencies of T_{VM} increased in the spleen (**Fig. 4A**), robust expansion of T_{VM} and IL-4Rα-dependent upregulation of EOMES was found in the mesenteric LN (mesLN) (**Fig. 4B-C**).

To further determine the IL-4Rα-dependent T_{VM} gene signature in the mesLN after *H. polygyrus* infection, we took advantage of the partial deletion of the *Il4ra* locus in IL-4R$\alpha^{\Delta CD8}$ mice. $CD124^+$ and $CD124^-$ $CD8^+$ T cells were FACS-sorted from the mesLN at day 15 after *H. polygyrus* infection of IL-4R$\alpha^{\Delta CD8}$ mice to tag each cell population before re-pooling for scRNA-seq (**Fig. 4D, Fig. S4D**). A total of 6,808 cells were validated with ~60% $CD124^+$ and ~40% $CD124^-$ cells. In $CD124^+$ cells, Seurat analysis identified clusters 1 and 5 as IL-4-induced T_{VM} based on the upregulation of *Eomes, Il2rb,* while reduced expression of *Itga4*. However, cluster 5 displayed additional signature genes of activation such as *Gzma, Ccr2, Ccr5,* and *Cd22* (**Fig. 4E-F, Fig. S4D**), as observed in the spleen (**Fig. 3D-E)**. None of the IL-4-dependent clusters upregulated *Gzmb* or exhaustion markers like *Pdcd1*.

Thus, these results specifically identified the nature of transcriptional changes in IL-4-induced T_{VM} during helminth infection.

CD22 expression is restricted to IL-4-induced T_{VM} cells. CD22 expression is largely restricted to B cells (*40*, *41*). While CD22 has recently been shown to regulate other cell types such as microglia (*42*), the role of CD22 in T lymphocytes remains poorly defined (*43*, *44*). We confirmed our prior observation that *Cd22* RNA expression was mainly restricted to the T_{VM} clusters (**Fig. 5A**) by flow cytometry detection of surface CD22 on $CD8^+$ T lymphocytes after IL-4c or *H. polygyrus* infection (**Fig. 5B**). Specific expression of CD22 by $CD8^+$ T cells was confirmed by ImageStream (**Fig. 5C**), excluding any potential cell doublets. Flow cytometry analysis of $CD22^+CD8^+$ T cells confirmed that IL-4-induced $CD22^+CD8^+$ T cells mainly express T_{VM} markers (**Fig. 5dD**), and the expansion of $CD22^+$ T_{VM} by IL-4c and *H. polygyrus* infection was significantly reduced in IL-4R$\alpha^{\Delta CD8}$ mice (**Fig. 5E-F**).

FlowSOM analysis of concatenated multicolor staining of $CD8^+$ T cells identified cluster C0 as being T_{VM} cells expressing high levels of CD44, CXCR3 and CD22 but lower levels of CD49d (**Fig. S5A-B**). Cluster C0 also expressed high levels of CD124, which was further confirmed as CD22 was only expressed by the E8iCre-escaping $CD124^+$ T cells in IL-4R$\alpha^{\Delta CD8}$ mice, whereas $CD22^+$ cells could not be detected in $CD124^-$ T cells (**Fig. 5G, Fig. S5C**). In addition, expansion of $CD22^+$ T cells was not observed in $CD4^+$ T cells after helminth infection (**Fig. S5D**). $CD22^+$ T_{VM} were also expanded in the mesenteric LN (mesLN) at day 15 after worm infection and were restricted to $CD124^+$ $CD8^+$ T cells (**Fig. 5H),** and upregulated EOMES (**Fig. S5E**).

We could also observe a strong expansion of CD22$^+$ T_{VM} after IL-4c treatment or *H. polygyrus* infection of C57BL/6 mice (**Fig. S5F**). Moreover, CD22$^+$ T_{VM} was observed in the spleen, the mesLN but also in more distant tissues such as the inguinal LN and bone marrow after *H. polygyrus* infection (**Fig. S5F-H**). However, T_{VM} expansion was mostly maintained after a single injection of IL-4c but surface CD22 was transient (**Fig. S5I**). IL-4c did not induce CD22 expression on thymic SP8 cells (**Fig. S5J**), or on virus-specific effector/memory T cells at 30 days after MuHV-4 infection (**Fig. S5K**). Furthermore, we could not detect any significant expression of CD22 on CD8$^+$ T cells from IL-4c treated or *H. polygyrus*-infected BALB/c or C57BL/6 *Il4ra*$^{-/-}$, or C57BL/6 *Stat6*$^{-/-}$ mice (**Fig. 5I**). Similarly, CD22 expression was not increased on *Il4ra*$^{-/-}$ CD8$^+$ T cells from WT:*Il4ra*$^{-/-}$ mixed bone marrow chimeras treated with IL-4c or infected with *H. polygyrus* (**Fig. 5J**).

These data collectively demonstrate that CD22 is specifically upregulated by IL-4 in expanding T_{VM}.

CD22$^+$ T_{VM} induced by IL-4 display an activated phenotype. To further study the specific functional program of CD22$^+$ T_{VM}, an RNA-seq analysis was performed on FACS-sorted CD44^{low} T_{NAIVE}, CD22$^+$, and CD22$^-$ CD44^{hi}CD49^{low} T_{VM} populations from PBS- or IL-4c-treated mice. Principal component analysis (PCA) revealed clustering of each analyzed cell population (**Fig. S6A**). Among genes upregulated in CD22$^+$ T_{VM}, we observed upregulation of *Cd22,* as well as genes related to effector functions and activation such as *Gzma*, *Ifng*, *Eomes, Il2rb*, *Mki67, Ctla2a, Slc16a2, Gzmm, Xcl1, Ccl4, Cxcr3, Ccr2* or *Ccr5* (**Fig. 6A-B)**. We observed significant gene set enrichment in CD22$^+$ T_{VM} of T cell signaling, cell cycle, NK mediated killing, and IL-2/STAT5 signaling (**Fig. 6C**), as well as MAPK and BCR signaling (**Fig. S6B**). Moreover, *Cd22* was the only upregulated siglec gene (**Fig. S6C**), whereas genes related to T cell exhaustion such as *Pdcd1*, *Lag3*, *Havcr2* (TIM3)*, Ctla4* or *Tox* were not significantly upregulated, apart from *Tigit* (**Fig. S6D**).

In comparison to CD22$^-$ T_{VM}, CD22$^+$ T_{VM} significantly upregulated inhibitory receptors such as, *Entpd1* (CD39), *Cd160, Klra3* (Ly49c), *Klra5* (Ly49e)*, Klra7* (Ly49g), *Klrc1* and *Klrd1* (NKG2A/CD94) and downregulated *Klrg1* and *Itga4* (CD49d) (**Fig. 6D, Fig. S6E**). Similar gene signatures with upregulation of *Cd22* together with its known interacting factors *Ptpn6*, *Grb2* and *Lyn*-related *Fyn* as well as upregulation of *Entpd1* or *Klra3* could be identified in the T_{VM} cluster in the mesLN during *H. polygyrus* infection (**Fig. S6F**).

The observed upregulation of EOMES, GZMA, CD39, CCR2, and CD160 were further confirmed by flow cytometry analysis of splenic T_{VM} after IL-4c (**Fig. 6E**) and at 2 weeks post-infection with *H. polygyrus* (**Fig. S7A**). In addition, significantly increased IFN-γ production upon IL-4 stimulation was confirmed in CD22$^+$ T_{VM} using reporter mice (**Fig. S7B-C**). The upregulation of *Mki67* and enrichment of cell cycle pathways suggests that IL-4 drives proliferation of CD22$^+$ T_{VM}, which was confirmed by increased EdU incorporation in dividing CD22$^+$ T_{VM} in mice treated with IL-4c (**Fig. 6F-H**). Moreover, a weak but significant increased activation of caspase 3/7 could be detected (**Fig. S7D**). IL-4c did not induce the conversion of CD44^{low} naïve T cells into T_{VM} but could drive the proliferation of both pre-existing CD22$^+$ T_{VM} and memory-phenotype T cells acquiring CD22 expression during cell division (**Fig. S7E-G**).

During *H. polygyrus* infection, IL-4 signaling via IL-4Rα and STAT6 activation was required to drive the expansion of T_{VM} upregulating CD22, CD39 and GZMA (**Fig. S8A-C**). Whereas T_{VM} exist in germ-free (GF) mice (*17*), microbiota might contribute to CD22 upregulation. However, expansion of T_{VM} co-expressing CD22, CD39 and GZMA also occurred in GF mice infected with axenic *H. polygyrus*, demonstrating that microbiota is not critical for CD22$^+$ T_{VM} expansion (**Fig. S8D**). Moreover, we noticed an increased GATA3$^+$ Th2

response in the mesLN of *H. polygyrus* infected GF mice, which was associated with increased CD39 and GZMA expression by $CD22^+$ T_{VM} (**Fig. S8E**). In addition, absence of IFN-I signaling was shown to be dispensable for the induction of CD22, CD39 and GZMA in T_{VM} during *H. polygyrus* infection (**Fig. S8F**).

Taken together, these data suggest that IL-4 drives the proliferation of $CD22^+$ T_{VM} displaying a phenotype of activation when compared to $CD22^-$ T_{VM}, and that the magnitude of *in vivo* IL-4 signals is a determinant of $CD22^+$ T_{VM} activation.

$CD22^+$ T_{VM} cells possess a diverse TCR repertoire enriched in self-reactive signatures. Memory-phenotype T cells have been shown to mainly arise from a pool of $CD8^+$ T cells that display reactivity towards endogenous self-ligands (*17*, *25*). Thus, we hypothesized that the IL-4 driven expression of the inhibitory molecule CD22 on peripheral T_{VM} cells could be restricted to self-reactive cells. We observed increased expression of *Cd5* in $CD22^+$ T_{VM} which is associated with self-antigen recognition (*45*, *46*) (**Fig. 6D**). Additionally, analysis of a public RNA-seq dataset revealed that $CD5^+$ T_{VM} also upregulate *Cd22* (*21*) (**Fig. 7A**), which was similarly found to be upregulated in $CCR2^+$ T_{VM} (*14*).

To investigate whether self-reactive T_{VM} could be preferentially expanded upon IL-4 signaling and whether CD22 could mark TCRs with higher self-reactivity, TCR sequencing was performed on $CD44^{low}$ T_{NAIVE}, $CD22^+$ T_{VM}, and $CD22^-$ T_{VM} populations from PBS- or IL-4c-treated mice (**Fig. S9A**). Both $CD22^-$ and $CD22^+$ T_{VM} possessed a highly diverse TCR repertoire, indicating a polyclonal expansion (**Fig. 7B-C, Fig. S9B**).

To verify whether this polyclonal expansion was stochastic or whether self-reactive TCRs were favored, CDR3α and CDR3β amino acid composition was further analyzed for several key physicochemical features described to influence self-antigen recognition (*47–49*). CDR3 sequences from IL-4-induced T_{VM}, especially the $CD22^+$ subset, displayed significantly enriched hydrophobic doublets in positions 6 and 7 (**Fig. 7D-E**), were enriched for CDR3 strength and volume, and showed reduced CDR3 polarity (**Fig. 7F-G and Fig. S9C-H**). Cumulative contribution of CDR3 features were assessed by principal component analysis and revealed a significant separation of $CD22^+$ T_{VM} from other groups (**Fig. 7H and Fig. S9I**). Supporting the hypothesis that CD22 expression is restricted to self-reactive TCR populations, IL-4c treatment induced strong T_{VM} expansion and CD22 expression in OT-I TCRtg cells, which are reported to exhibit relatively high levels of autoreactivity (**Fig. 7I**) (*25*, *50*, *51*). Conversely, T_{VM} expansion and CD22 expression were significantly reduced in the non-autoreactive CSP TCRtg mice (*54*) after IL-4c (**Fig. 7I**) (*52*).

Collectively, these data demonstrate that IL-4 drives the expression of CD22 at the surface of expanding self-reactive T_{VM} cells.

The lack of CD22 leads to increased activation of T_{VM} during helminth infection. The expression of the inhibitory receptor CD22 on the most self-reactive T_{VM} might act to regulate T cell activation. Thus, we studied T_{VM} expansion in CD22-deficient mice (*$Cd22^{-/-}$*) (*53*). As expected, $CD22^+$ T_{VM} could not be found in *$Cd22^{-/-}$* mice (**Fig. S10A**). *$Cd22^{-/-}$* mice had significantly more T_{VM} at steady-state and their numbers were significantly increased after IL-4c when compared to WT mice (**Fig. 8A**), but the expression of EOMES was similarly increased (**Fig. 8B**). However, *$Cd22^{-/-}$* T_{VM} produced significantly more CD39 and GZMA in response to IL-4c (**Fig. 8B, Fig. S10D-E**). After *H. polygyrus* infection (**Fig. S10B**), $CD22^+$ T_{VM} strongly expanded in spleen and mesLN of WT mice, but the expansion of T_{VM} was surprisingly not affected in *$Cd22^{-/-}$* mice (**Fig. 8C**) and no difference in parasite burden was observed (**Fig. S10C**). Th2 responses including IL-4 production was significantly impaired in

Cd22$^{-/-}$ mice **(Fig. S10F-G)**, likely explaining the reduced activation of T_{VM} in *Cd22*$^{-/-}$ mice infected with *H. polygyrus*.

Since CD22 is strongly expressed in B lymphocytes to regulate B cell responses, the absence of CD22 expression on B cells in *Cd22*$^{-/-}$ mice could indirectly interfere with T_{VM} responses. Thus, mixed bone marrow WT:*Cd22*$^{-/-}$ chimeras were generated to investigate in a competitive setting how a cell-intrinsic lack of CD22 could impact T_{VM} responses (**Fig. S11A**). CXCR3^{+}CD49d^{low} T_{VM} expansion upon IL-4c treatment or *H. polygyrus* infection was significantly increased in the *Cd22*$^{-/-}$ CD8^{+} T cell compartment (**Fig. 8D**). WT and *Cd22*$^{-/-}$ T_{VM} expressed similar levels of EOMES but the levels of expression of GZMA and CD39 were significantly increased after both IL-4c treatment or *H. polygyrus* infection in *Cd22*$^{-/-}$ T_{VM} (**Fig. 8D, Fig. S11B**). When comparing the levels of CD22, CD39 and GZMA expression in T_{VM} of chimeric mice, the highest CD22 expression were observed in mice displaying higher CD39 and GZMA expression as well (**Fig. S11C**).

These data indicate that CD22 regulates the magnitude of the response to IL-4 activation and T_{VM} expansion. If so, we reasoned that mutation of the cytoplasmic ITIM motifs in CD22 should mimic the absence of CD22. To address this, we used transgenic *Cd22*^{Y2,5,6F} knock-in mice in which the ITIM signaling domains were mutated to prevent CD22 downstream signaling (*54*) (**Fig. S11D**). Mixed bone marrow WT:*Cd22*^{Y2,5,6F} chimeras were generated to investigate IL-4-dependent T_{VM} expansion. Again, whereas EOMES expression was not affected in T_{VM} by the absence of CD22 signaling, IL-4 activation of *Cd22*^{Y2,5,6F} CD8^{+} T cells resulted in a significant increased CD49d^{low} T_{VM} expansion, expressing higher levels of CD39 and GZMA (**Fig. 8E, Fig. S11E**). Next, we further examined the role of CD22 in regulating TCR and/or bystander activation upon *ex vivo* stimulation of IL-4-expanded T_{VM}. We observed that CD22 deficiency resulted in a significant increase of IFN-γ production upon restimulation *ex vivo* (**Fig. S11F, G**). Moreover, impaired CD22 signaling in T_{VM} resulted in an altered "effector-like" T_{VM} response, with increased KLRG1, CD39, and GZMA and increased CD44^{+}CD62L^{low} effector T cells, as well as increased CD107a detection during stimulation (**Fig. S11H-I**). To further investigate how the absence of CD22^{+} T_{VM} would affect the CD8^{+} T cell response to respiratory viral infection, WT:*Cd22*$^{-/-}$ chimeras were infected with strain PR8 of influenza virus (IAV) after IL-4c treatment (**Fig. 8F-H, Fig. S12A-B**). At day 6 after IAV infection, we observed a significant infiltration of CD8^{+} T cells in the airway (**Fig. S12B**), displaying a similar chimerism as observed in peripheral blood before IAV infection (**Fig. 8F**). However, significantly higher proportions of GZMA^{+}, GZMB^{+} and CD39^{+} T cells were observed in the *Cd22*$^{-/-}$ T cell compartment after IAV infection (**Fig. 8G**), together with an increased ability to produce IFN-γ upon restimulation (**Fig. 8H**).

Then we generated mixed bone marrow chimeras by engrafting in B and T cell-deficient *Rag2*$^{-/-}$ mice a 1:1 ratio of bone marrow cells *Cd22*$^{-/-}$ and *Cd3e*$^{-/-}$, and compared their response to IL-4c treatment and IAV infection with *Rag2*$^{-/-}$ mice engrafted with WT and *Cd3e*$^{-/-}$ bone marrow cells (**Fig. S12C**). Using these chimeric mice, we could confirm the increased T_{VM} response in CD22-deficient CD8^{+} T cells in response to IL-4 (**Fig. S12D**). Moreover, *Cd22*$^{-/-}$*:Cd3e*$^{-/-}$ chimeric mice lost significantly more weight upon IAV infection when compared to WT*:Cd3e*$^{-/-}$ chimeric mice (**Fig. 8I**), which was associated with increased production of IFN-γ and GZMB (**Fig. 8J-K**), and expression of CD39 and CD49d in lung CD8^{+} T cells (**Fig. S12E**).

Next, we investigated the ability of CD22^{+} or CD22^{-} T_{VM} to contribute to the antigen-specific CD8^{+} T cell response to murine cytomegalovirus (MCMV) infection, which induces a virus-specific CD8^{+} T cell response known as memory inflation (*55*). We took advantage of CSP TCRtg Thy1.1^{+} mice (**Fig. 7I**), to investigate the expansion of IL-4-induced CSP-specific CD22^{+} and CD22^{-} T_{VM} after adoptive transfer and infection with a MCMV-ie2^{CSP} recombinant

virus. Then, weekly monitoring of circulating CSP-specific Thy1.1^{+}Thy1.2^{-} CD8^{+} T cells, revealed a significantly reduced expansion of CD22^{+} CSP TCRtg cells (**Fig. 8L, Fig. S12F-H**). In addition to CD22, CD22^{+} T_{VM} also upregulated several inhibitory receptors that could mediate regulatory activities against immunopathology (**Fig 6D**). We also confirmed that a significant proportion of CD22^{+} T_{VM} express Ly49 (**Fig. 8M**), a killer cell lectin-like receptor involved in regulatory functions of self-tolerant CD8^{+} T cells (*56*, *57*). Thus, CD22^{+} T_{VM} might be less responsive to stimulation because they have regulatory functions. Confirming this hypothesis, co-transfer of naïve CD4^{+} T cells with CD22^{+} T_{VM} significantly protected Rag-deficient mice from inflammatory bowel disease, in contrast to CD22^{-} T_{VM} (**Fig. 8N**).

Thus, these data demonstrate that CD22 limits IL-4-driven T_{VM} expansion, resulting in reduced responsiveness to stimulation of CD22^{+} T_{VM} and regulation of immunopathology.

Discussion

Overall, our results reveal the unexpected finding that CD22 is specifically expressed by IL-4-driven self-specific T_{VM} to control their expansion and activation during helminth infection. Specifically, we have demonstrated that IL-4 signaling during *H. polygyrus* infection in peripheral $CD8^+$ T cells drives the engagement of a specific gene signature program of activation, together with CD22 and other counter-inhibitory receptors that are not related to T cell exhaustion.

We found that IL-4R$\alpha^{\Delta CD8}$ mice, although partially knockout for *Il4ra*, had significantly reduced T_{VM} population in the spleen, whereas CD124 expression was not affected in the thymus. We could demonstrate the selective expression of the Cre recombinase in mature $CD8^+$ T cells exiting the thymus in IL-4R$\alpha^{\Delta CD8}$ mice and the requirement of IL-4 signaling in $CD8^+$ T cells to drive the expansion and functional changes in peripheral T_{VM}. Indeed, T_{VM} expansion and upregulation of signature markers of IL-4-induced T_{VM} like CD22, CD39, and GZMA were specifically found in $CD124^+$ T_{VM} after *H. polygyrus* infection. Moreover, we could not observe the upregulation of these markers in *Il4ra*$^{-/-}$ or in *Stat6*$^{-/-}$ mice, irrespective of the strain background. These findings clearly highlight the requirement of IL-4 signaling in driving a specific program in T_{VM} upon helminth infection. These findings are important as IL-15 signaling has also been shown to expand T_{VM} upon *H. polygyrus* infection (*9*). As both cytokines signal through the common gamma chain (γc), they might trigger overlapping intracellular activation pathways in T_{VM} (*58*).

Our study enhanced the description of IL-4-induced T_{VM} during helminth infection using scRNA-seq, thereby adding to our understanding of memory/effector $CD8^+$ T cell diversity previously reported in other settings (*59*, *60*). Further, gene signature analyses highlighted that IL-4-induced T_{VM} differ from classical T_{TM} or exhausted T cells and are rather characterized by a unique gene expression signature. While confirming previous transcriptomic characterizations of T_{VM} (*6*, *14*, *21*), our scRNA-seq data suggests similar trajectories of differentiation followed by IL-4 or *H. polygyrus*-induced T_{VM}, and further provides unique information about the expanding T_{VM} subset. Although we also observed changes in the expression of these signature genes in IL-4R$\alpha^{\Delta CD8}$, the magnitude of their differential expression was overall reduced when compared to WT littermate controls in the spleen, likely because IL-4R$\alpha^{\Delta CD8}$ are partially knockout and a remaining population of $CD124^+CD8^+$ T cells exist. Indeed, when single cell transcriptomes were studied in sorted $CD124^+$ or $CD124^-$ $CD8^+$ T cells from the mesLN of *H. polygyrus* infected mice, IL-4-induced T_{VM} signature was only found in IL-4Rα-competent cells. When computing the significant differentially expressed genes in both IL-4 and *H. polygyrus*-induced T_{VM}, effector genes were upregulated, but we also unexpectedly observed the upregulation of *Cd22*.

CD22 is a canonical inhibitory receptor of B lymphocytes which contributes to control autoimmune disease (*40*), and its expression on other cell types has only been scarcely reported (*42–44*, *61*). CD22 is upregulated by microglia in aging brains, where it inhibits phagocytosis (*42*), and one report identified functional CD22 in primary T cells but with a very low surface expression level (*43*). CD22 was the only sialic acid-binding immunoglobulin-type lectin (siglec) gene upregulated in T cells upon IL-4 signaling and we demonstrated that CD22 is expressed at the surface of IL-4-induced T_{VM} specifically, whereas IL-4 did not upregulate CD22 in virus-specific effector/memory T cells, thymocytes or $CD4^+$ T cells. At the cell surface of B lymphocytes, CD22 creates homo-oligomers and also binds to CD45 *in cis* via interactions with α2,6-linked sialic acids (*41*, *62*). However, the B cell receptor (BCR) does not interact

with CD22 via sialic acids and both BCR and CD22 are rather found in separate membrane domains (*41*). In mouse models where CD22 cannot bind sialic acid (*54*), less CD22 homo-oligomers are formed, resulting in increased association with the BCR. We have not investigated to which ligand(s) T_{VM} CD22 binds, but we did observe that the $CD22^+$ T_{VM} had a distinct functional phenotype and expressed a diverse TCR repertoire enriched in features of self-reactivity when compared to naive T cells and from $CD22^-$ T_{VM}. Previous reports showed that IL-4-responding antigen-specific T_{TM} had an altered effector phenotype with reduced NKG2D or CCL5 expression (*63*), but our results highlighted that IL-4 production in response to helminth infection drives an enrichment of genes involved in TCR signaling, cytotoxicity, cell cycle, and the STAT-5 activation pathway, and we could also further demonstrate that IL-4-driven $CD22^+$ T_{VM} expansion does not result from conversion of naïve T cells, but can rather result from active division of pre-existing $CD22^+$ T_{VM} or proliferation of $CD22^-$ T_{VM} which acquire CD22 while dividing.

TCR activation is supported by the enriched features of CDR3 sequences associated with self-reactivity, similar to that observed in regulatory T cells (Tregs) (*17*, *25*, *49*). EOMES has been involved during the maturation of precursors of self-reactive memory-phenotype T cells (*17*). Thus, it is possible that IL-4 induces an effector/memory program in self-specific T_{VM} via EOMES activation which is then counter-regulated by CD22 expression. This possibility is also supported by the observed upregulation of the proto-oncogene Src tyrosine protease *Fyn*, related to the oncogene *Lyn* which is required for CD22 inhibitory activity in B lymphocytes as well as increased expression of the adaptor protein-encoding gene *Grb2* and *Ptpn6* (encoding phosphatase SHP-1), both interacting with the immunoreceptor tyrosine-based inhibitory motif (ITIM) of CD22 (*64*). However, CD22 might not be the only inhibitory strategy to counter-regulate IL-4-responding T_{VM}, since increased expression of CD39, CD160, or inhibitory Ly49 molecules were also observed in $CD22^+$ T_{VM}. CD39 was even more strongly expressed in $Cd22^{-/-}$, suggesting the absence of CD22 might be at least partially compensated by upregulation of alternative regulatory receptors.

We found that naive germline $Cd22^{-/-}$ mice had higher numbers of T_{VM} in steady-state when compared to WT mice, without affecting worm control. However, $Cd22^{-/-}$ mice responded to helminth infection with significantly reduced Th2 responses while expanding similar levels of T_{VM}, which suggests CD22 on T cells controls IL-4-driven T_{VM} expansion and activation. Confirming this hypothesis, $Cd22^{-/-}$ or $Cd22^{Y2,5,6F}$ T_{VM} in mixed-bone marrow chimeras strongly responded to IL-4 with an increased expansion of T_{VM} producing higher levels of CD39 and GZMA, reporting an increased activation phenotype. When $Cd22^{-/-}$ or $Cd22^{Y2,5,6F}$ T_{VM} were subjected to TCR-triggering stimulation or bystander IL-12/IL-18 treatment, T_{VM} responded by producing higher levels of IFN-γ as well as increased expression of activation markers like KLRG1 and CD39 with an enrichment of $CD44^{hi}CD62L^{low}$ effector T cells. In addition, IAV infection of mixed-bone marrow chimeras resulted in a stronger activation and cytotoxic potential of $Cd22^{-/-}$ $CD8^+$ T cells in the airway. Moreover, in bone marrow chimeric mice in which all T cells are CD22-deficient, $CD8^+$ T cell activation in the lung significantly increased in response to IAV infection and was associated with an exacerbation of viral disease. Thus, CD22 intrinsically controls T cell activation, which was also confirmed after adoptive transfer of TCR transgenic T cells before MCMV infection where CD22 expression in antigen-specific T_{VM} resulted in a lower response to the cognate antigen.

Besides the observation that $CD22^+$ T_{VM} display reduced responsiveness to stimulation, the expression of CD22 together with other regulatory receptors like Ly49 could result in regulatory functions of $CD22^+$ T_{VM}. Indeed, $CD8^+$ T cells expressing inhibitory Ly49 or related killer cell

immunoglobulin-like (KIR) receptors in mouse or human, respectively, have been reported to ensure immunoregulation and control immunopathology (*56*, *57*, *65*). Thus, in addition to intrinsic effects of CD22 to limit T cell activation, IL-4-induced $CD22^+$ T_{VM} could also suppress pathogenic processes (*66*). It is interesting to note that such immunoregulatory mechanism mediated by $CD22^+$ T_{VM} would be absent in *Cd22*$^{-/-}$:*Cd3e*$^{-/-}$ chimeric mice and these mice displayed an exacerbated lung disease after IAV infection, suggesting $CD22^+$ T_{VM} might also be contributing in suppressing lung disease. Further supporting the regulatory function of $CD22^+$ T_{VM}, $CD4^+$ T cell-induced inflammatory bowel disease was controlled by $CD22^+$ T_{VM}, but not by $CD22^-$ T_{VM}.

However, while these findings demonstrate that CD22 is expressed in T_{VM} upon IL-4 stimulation and regulates T cell activation, the exact mechanisms driving the regulatory functions of $CD22^+$ T_{VM} are yet to be elucidated. In addition, whereas mouse T_{VM} upregulate CD22 in response to IL-4-driven expansion, it remains unknown such self-specific T_{VM} population harboring regulatory functions also expands upon helminth infection or IL-4-driven inflammation in human.

Despite these limitations, our findings identify CD22 as an inhibitory receptor that limits IL-4-driven stimulation of T_{VM} during worm infection in mice, resulting in significantly reduced responsiveness of $CD22^+$ T_{VM} and robust regulatory functions. It now remains to be determined whether IL-4-mediated activation of self-reactive T_{VM} and induction of CD22 is a transient phenomenon or has long-term effects on $CD22^+$ T_{VM}, resulting in trained immunity to support disease tolerance.

Materials and methods

Study design

In this study, we investigated the IL-4-mediated expansion, transcriptional regulation, identity, and functional changes in T_{VM} populations during enteric helminth infection. To this end, we used flow cytometry, imaging flow cytometry, single-cell and bulk transcriptomic approaches, TCR-sequencing, bone-marrow chimeras, gene targeting, and adoptive transfer. Allocation of sex- and age-matched mice into experimental groups was done randomly in each experiment. No data were excluded from the analyses. The specific numbers of mice, the number of experimental replicates, and the statistical tests performed are all included in the respective figure legends.

Mice

The experiments, maintenance and care of mice and rats complied with the guidelines of the European Convention for the Protection of Vertebrate Animals used for Experimental and other Scientific Purposes (CETS n° 123). The protocol was approved by the Committee on the Ethics of Animal Experiments of the University of Liège, Belgium (Permit nos. 2001 and 2371). All efforts were made to minimize suffering. Female BALB/cAnNCrl and C57BL/6NCrl wild-type mice, 6–8 weeks old, were purchased from Charles River. Details about the transgenic mouse strains can be found in the Supplementary Materials. Six- to eight-week-old female littermates were randomly assigned to experimental groups. During experiments, 4 to 5 mice were cohoused per cage, food and water was provided ad libitum. All the animals were bred and/or housed at the University of Liège, GIGA-ULiège and Department of Infectious Diseases or at the McGill University Health Centre Research Institute.

Reconstitution of germ-free mice

To colonize GF mice with specific-pathogen-free microbiota (exGF), fresh fecal pellets from C57BL/6 WT mice were homogenized in PBS to a concentration of 62.5 g mL^{-1}. The fecal slurry was centrifuged at 700 × g for 5 min to remove large debris. The supernatant was collected and diluted by ten-fold in PBS before being administered to 6-8 week old GF mice (150 µL per mouse by gavage). exGF were used 3-4 weeks after microbial reconstitution.

Parasites

The lifecycle of *H. polygyrus* was maintained in male C57BL/6 mice as described (*67*). Briefly, 6-8-week-old male C57BL/6 mice were infected with 300 *H. polygyrus* L3 larvae in 200 µL of distilled water by oral gavage. After 14 days post infection, the mice were placed on a grid and fecal pellets collected after several hours. Then, the feces were mixed with granulated charcoal at a ratio of at least a 1:1, to achieve a consistency just damp enough with distilled water to adhere to filter paper. A thin layer was smeared on the center of dampened filter paper in a petri dish placed in a humid box in the dark. The larvae form a ring around the edge of the filter paper and were collected from day 7 onwards for at least three occasions before the paper was discarded. The larvae were collected in distilled water in a 15 mL tube and washed in cold dH_2O and centrifuged at 150 x *g* for 5 min a total of ten times. The purified *H. polygyrus* L3 larvae were stored in distilled water at 4 °C for up to 6 months. For experiments, L3 larvae were washed in distilled water 3 times before administration of 200 × L3 larvae in 200 µL distilled water by gavage. For infection of GF and exGF mice, the *H. polygyrus* lifecycle was maintained in axenic conditions as described (*68*).

IL-4 complex treatment
Mice received 2 intraperitoneal injections of IL-4c: 5 µg of recombinant IL-4 (BioLegend, carrier-free) and 25 µg of anti-IL-4 antibody (BioLegend, clone 11B11, Ultra LEAF purified) per mouse at day 0 and day 2.

Cell preparation.
Spleen, thymus and lymph nodes were harvested, cut in small pieces using scissors and filtered through a 100 µm cell strainer with a sterile syringe plunger. Erythrocytes were lysed in red cell lysis solution (155 mM NH_4Cl, 0.12 mM EDTA, 10 mM $KHCO_3$), and leukocytes suspended in PBS and filtered through a 40 µm cell strainer. Airways were flushed twice with 1 mL of ice-cold PBS, and cells were harvested by centrifugation of the BAL fluid. After section of the vena cava, lungs were perfused with 5 mL of ice-cold PBS through the right ventricle. Lungs were dissociated with the gentleMACS dissociator (Miltenyi Biotec) in C-tube (Miltenyi Biotec), incubated in HBSS (Gibco), 5% FCS, 1 mg mL^{-1} of collagenase D (Roche) and 0.1 mg mL^{-1} of DNase I (Roche) for 30 min at 37°C under agitation and further dissociated with the gentleMACS dissociator. The resulting suspension was washed in cold PBS/2mM EDTA and filtered on a 100µm cell strainer (Falcon). Cells were counted in a Neubauer cytometer chamber in 0.4% buffered trypan blue dye for exclusion of dead cells.

Antibodies and flow cytometry.
Incubations were performed in FACS buffer (PBS containing 0.1% BSA and 0.05% NaN3) at 4°C. Cells were first incubated with anti-mouse CD16/32 antibody (clone 93, 1 µg mL^{-1}, isotype Rat IgG2a, $^{21,22}\lambda$, BioLegend) before fluorochrome-conjugated antibodies against surface antigens were added and incubated during 20 min at 4 °C, followed by staining of dead cells (see Supplementary Materials for details). For detection of intracellular cytoplasmic proteins, cells were fixed in paraformaldehyde 2% in PBS on ice for 20 min, before permeabilized and stained in FACS buffer containing 0.1% saponin for 30 min at 4°C (see Supplementary Materials for antibody details). In experiments in which intranuclear staining for transcription factors was needed, cells were fixed and permeabilized using Foxp3/Transcription factor staining buffer set (eBioscience) following manufacturer's instruction and incubated 30 min at 4°C (see Supplementary Materials for antibody details). Samples were analyzed on a Fortessa X-20 or FACSymphony A5SE flow cytometer (BD Biosciences). Flow cytometry acquisitions were analyzed using FlowJo 10.8 or 10.9. In some analyses, samples were concatenated and further analyzed using the built-in plugins UMAP and FlowSOM. In some experiments, samples were analyzed using an ImageStream X Mk II (Amnis, VIB Flow Core Facility, UGhent).

***In vivo* EdU incorporation and cell proliferation assay**
Mice were injected intraperitoneally with EdU (500 µg/mouse in PBS, ThermoFisher Scientific) daily for 3 days before endpoint (3×). Mice were euthanized and spleen were processed as described above. Surface and viability stainings were performed before cell were subjected to click-it chemistry using the Click-iT Plus EdU Pacific Blue Flow Cytometry assay kit (Thermo Fisher). In some experiments, T cell population were FACS-sorted and labeled with CellTrace Violet Cell Proliferation Kit (Thermo Fisher) before adoptive transfer in recipient congenic mice.

Detection of apoptotic cells
Apoptotic cells were detected by flow cytometry using the CellEvent Caspase-3/7 Green Flow Cytometry assay kit (ThermoFisher).

Mixed bone-marrow chimeric mouse models.
Mixed bone-marrow chimeric mice were produced by treating Thy1.1^{+}Thy1.2^{+} BALB/c mice, CD45.1^{+}CD45.2^{+} C57BL/6 (CD45.1.2) or *Rag2*$^{-/-}$ mice with intraperitoneal injection of busulfan (25 μg g^{-1} of mouse body weight per day for 3 consecutive days, Cayman Chemical) for myeloablation, according to a published protocol (*69*). Then, mice were reconstituted by intravenous injection of 2×10^6 bone marrow cells at 24h after the last busulfan injection. Bone marrow cells were obtained from femurs and tibias of donor mice and mixed at a 1:1 ratio (CD45.1^{+} WT and CD45.2^{+} *Il4ra*$^{-/-}$, CD45.1^{+} WT and CD45.2^{+} *Cd22*$^{-/-}$or *Cd22*^{Y2,5,6F}, WT or *Cd22*$^{-/-}$and *Cd3e*$^{-/-}$*)* before intravenous injection in 100 μL sterile PBS into recipient mice. Mice were left untreated for 6 weeks to allow complete reconstitution and chimerism of circulating CD8^{+} T cells was then confirmed by flow cytometry, before used in experiments.

T cell transfer-induced colitis.
Single-cell suspension was obtained from spleens of naive C57BL/6 WT mice before enrichment of CD4^{+} T lymphocytes using the MojoSort Mouse CD4 T Cell Isolation Kit (Biolegend) and LS columns (Miltenyi Biotec). Then, CD45RB^{hi}CD25^{-} CD4^{+} T cells were FACS-sorted and administered intraperitoneally into sex and age-matched *Rag2*$^{-/-}$ mice (5×10^5 cells per mouse) with 5×10^5 cells per mouse of sorted CD22^{+} or CD22^{-} T_{VM} from the spleens of IL-4c-treated C57BL/6 WT mice. Mice were weighed and monitored for signs of disease every 3-4 days.

Cell isolation for single-cell RNA-seq assay and library preparation
Single-cell suspension were obtained from harvested spleen or mesLN before enrichment of CD8^{+} T lymphocytes using the MojoSort Mouse CD8 T Cell Isolation Kit (Biolegend) and LS columns (Miltenyi Biotec). For spleen samples, enriched CD8^{+} T cells isolated from mice of the same genotype and having received the same treatment were individually stained with 0.5 μg per 1.5 million cells of TotalSeq anti-mouse hashtag antibodies (A0301 to A0305, Biolegend) and incubated at 4°C during 20 min before pooling (n=4 to 5). Pools were then filtered through a 40 μm cell strainer and the concentration adjusted to 700 to 1000 cells μL^{-1} before single cell capture using the Chromium controller (10x Genomics). For mesLN samples, enriched CD8^{+} T cells from IL-4RαΔ^{CD8} mice were pooled and further sorted to high purity based on the expression of CD124. Then, CD124^{+} or CD124^{-} were stained with 20 μL per 1 million cells of Sample Tag 1 or Sample Tag 2 from the Mouse Immune Single-Cell Multiplexing Kit (BD Biosciences) and pooled before filtered through a 40 μm cell strainer, before being subjected to single cell capture and quality control using the BD Rhapsody Express and BD Rhapsody Scanner (BD Biosciences). Spleen samples were processed using the 10x genomics Chromium Single Cell 3' v3 chemistry as per the manufacturer's recommendations (10x Genomics). Samples obtained from mesLN were processed using the BD Rhapsody Whole Transcriptome Analysis cDNA synthesis and amplification kit as per the manufacturer's recommendations (BD Biosciences). Barcoded RNA was collected and processed following the manufacturer's recommendations. After quantification, equal molar concentrations of each library were pooled and sequenced using the NovaSeq S4 300 cycles XP workflow (GIGA ULiege, Belgium).

RNA sequencing
Single-cell suspensions were obtained from harvested spleens before enrichment of CD8^{+} T lymphocytes using the MojoSort Mouse CD8 T Cell Isolation Kit (Biolegend) and LS columns (Miltenyi Biotec). Then, around 100,000 cells were sorted in IMDM 50% FCS using a FACS Aria IIIu (BD biosciences). Total RNA was purified using the RNAeasy Micro Kit (Qiagen)

and eluted in 14µL of water. RNA integrity was further verified using a 2100 Agilent Bioanalyzer and RIN > 9 were used for further analyses. Total RNA was then used as input for the SMART-seq HT cDNA synthesis kit (Takara) an libraires prepared (see Supplementary Materials for details).

TCR sequencing

Single-cell suspensions were obtained from harvested spleens before enrichment of $CD8^+$ T lymphocytes using the MojoSort Mouse CD8 T Cell Isolation Kit (Biolegend) and LS columns (Miltenyi Biotec). Then, 200,000 cells were sorted in IMDM 50% FCS using a FACS Aria IIIu (BD biosciences). RNA extraction was carried out using the RNeasy Micro Kit (Qiagen, 217084). High-throughput sequencing was performed as previously described with template-switch anchored RT-PCR but using oligodT during the cDNA generation and the following mouse-specific Cα and Cβ primers for the PCR amplification: TRAC '5-*GTCTCGTGGGCTCGGAGATGTGTATAAGAGACAG*GTCCTGAGACCGAGGATCTTT and TRBC '5-*GTCTCGTGGGCTCGGAGATGTGTATAAGAGACAG*GGGTAGCCTTTTG-TTTGTTTG (adapters in italic). Details for CDR3 sequence analysis can be found in the Supplementary Materials.

Statistical analysis

Statistical evaluation of different groups was performed either by analysis of variance (ANOVA) followed by the Dunnett, Tukey or Sidak multiple comparisons test or by unpaired t test or non-parametric Mann-Whitney test, as indicated. A p-value < 0.05 was considered significant. Statistical analyses were performed using Prism v9 (GraphPad, La Jolla, CA). * or $^{\#}P < 0.05$, ** or $^{\#\#}P < 0.01$, ***or $^{\#\#\#}P < 0.001$, **** or $^{\#\#\#\#}P < 0.0001$

List of Supplementary materials

Supplementary materials and methods
Figure S1-S11
Table S1-S2
Supplementary data file S1. Raw data file

References

1. R. L. Pullan, J. L. Smith, R. Jasrasaria, S. J. Brooker, Global numbers of infection and disease burden of soil transmitted helminth infections in 2010. *Parasit Vectors* **7**, 37 (2014).
2. P. J. Hotez, P. J. Brindley, J. M. Bethony, C. H. King, E. J. Pearce, J. Jacobson, Helminth infections: the great neglected tropical diseases. *J Clin Invest* **118**, 1311–1321 (2008).
3. P. M. Jourdan, P. H. L. Lamberton, A. Fenwick, D. G. Addiss, Soil-transmitted helminth infections. *The Lancet* **391**, 252–265 (2018).
4. N. L. Harris, P. Loke, Recent Advances in Type-2-Cell-Mediated Immunity: Insights from Helminth Infectionfile:///Applications/Mendeley%20Reference%20Manager.app/Contents/Resources/app.asar/dist/production.html#/library. *Immunity* **47**, 1024–1036 (2017).
5. F. Vacca, G. le Gros, Tissue-specific immunity in helminth infections. *Mucosal Immunology 2022 15:6* **15**, 1212–1223 (2022).
6. M. Rolot, A. M. Dougall, A. Chetty, J. Javaux, T. Chen, X. Xiao, B. Machiels, M. E. Selkirk, R. M. Maizels, C. Hokke, O. Denis, F. Brombacher, A. Vanderplasschen, L. Gillet, W. G. C. Horsnell, B. G. Dewals, Helminth-induced IL-4 expands bystander memory CD8+ T cells for early control of viral infection. *Nat Commun* **9**, 4516 (2018).
7. J. S. Lin, K. Mohrs, F. M. Szaba, L. W. Kummer, E. A. Leadbetter, M. Mohrs, Virtual memory CD8 T cells expanded by helminth infection confer broad protection against bacterial infection. *Mucosal Immunol*, doi: 10.1038/s41385-018-0100-x (2018).
8. P. Tripathi, S. C. Morris, C. Perkins, A. Sholl, F. D. Finkelman, D. A. Hildeman, IL-4 and IL-15 promotion of virtual memory CD8+ T cells is determined by genetic background. *Eur J Immunol* **46**, 2333–2339 (2016).
9. T. Hussain, A. Nguyen, C. Daunt, D. Thiele, E. S. Pang, J. Li, A. Zaini, M. O'Keeffe, C. Zaph, N. L. Harris, K. M. Quinn, N. L. La Gruta, Helminth Infection–Induced Increase in Virtual Memory CD8 T Cells Is Transient, Driven by IL-15, and Absent in Aged Mice. *The Journal of Immunology* **210**, 297–309 (2023).
10. B. J. Laidlaw, J. E. Craft, S. M. Kaech, The multifaceted role of CD4(+) T cells in CD8(+) T cell memory. *Nat Rev Immunol* **16**, 102–111 (2016).
11. I. H. Seo, H. S. Eun, J. K. Kim, H. Lee, S. Jeong, S. J. Choi, J. Lee, B. S. Lee, S. H. Kim, W. S. Rou, D. H. Lee, W. Kim, S. H. Park, E. C. Shin, IL-15 enhances CCR5-mediated migration of memory CD8+ T cells by upregulating CCR5 expression in the absence of TCR stimulation. *Cell Rep* **36**, 109438 (2021).
12. J. Y. Lee, S. E. Hamilton, A. D. Akue, K. A. Hogquist, S. C. Jameson, Virtual memory CD8 T cells display unique functional properties. *Proc Natl Acad Sci U S A* **110**, 13498–13503 (2013).
13. C. Haluszczak, A. D. Akue, S. E. Hamilton, L. D. Johnson, L. Pujanauski, L. Teodorovic, S. C. Jameson, R. M. Kedl, The antigen-specific CD8+ T cell repertoire in unimmunized mice includes memory phenotype cells bearing markers of homeostatic expansion. *J Exp Med* **206**, 435–448 (2009).
14. S. Hou, T. Shao, T. Mao, J. Shi, J. Sun, M. Mei, X. Tan, H. Qi, Virtual memory T cells orchestrate extralymphoid responses conducive to resident memory. *Sci Immunol* **6** (2021).
15. S. C. Jameson, D. Masopust, Understanding Subset Diversity in T Cell Memory. *Immunity* **48**, 214–226 (2018).
16. J. T. White, E. W. Cross, R. M. Kedl, Antigen-inexperienced memory CD8+ T cells: where they come from and why we need them. *Nat Rev Immunol* **17**, 391–400 (2017).

17. C. H. Miller, D. E. J. Klawon, S. Zeng, V. Lee, N. D. Socci, P. A. Savage, Eomes identifies thymic precursors of self-specific memory-phenotype CD8+ T cells. *Nat Immunol*, 1–11 (2020).
18. V. Martinet, S. Tonon, D. Torres, A. Azouz, M. Nguyen, A. Kohler, V. Flamand, C. A. Mao, W. H. Klein, O. Leo, S. Goriely, Type I interferons regulate eomesodermin expression and the development of unconventional memory CD8(+) T cells. *Nat Commun* **6**, 7089 (2015).
19. T. Hussain, K. M. Quinn, Similar but different: virtual memory CD8 T cells as a memory-like cell population. John Wiley and Sons Inc. [Preprint] (2019). https://doi.org/10.1111/imcb.12277.
20. K. M. Quinn, A. Fox, K. L. Harland, B. E. Russ, J. Li, T. H. O. Nguyen, L. Loh, M. Olshanksy, H. Naeem, K. Tsyganov, F. Wiede, R. Webster, C. Blyth, X. Y. X. Sng, T. Tiganis, D. Powell, P. C. Doherty, S. J. Turner, K. Kedzierska, N. L. La Gruta, Age-Related Decline in Primary CD8(+) T Cell Responses Is Associated with the Development of Senescence in Virtual Memory CD8(+) T Cells. *Cell Rep* **23**, 3512–3524 (2018).
21. J. T. White, E. W. Cross, M. A. Burchill, T. Danhorn, M. D. McCarter, H. R. Rosen, B. O'Connor, R. M. Kedl, Virtual memory T cells develop and mediate bystander protective immunity in an IL-15-dependent manner. *Nat Commun* **7**, 11291 (2016).
22. S. C. Jameson, The naming of memory t-cell subsets. *Cold Spring Harb Perspect Biol* **13**, 1–12 (2021).
23. Y. J. Lee, K. L. Holzapfel, J. Zhu, S. C. Jameson, K. A. Hogquist, Steady-state production of IL-4 modulates immunity in mouse strains and is determined by lineage diversity of iNKT cells. *Nat Immunol* **14**, 1146–1154 (2013).
24. M. A. Weinreich, O. A. Odumade, S. C. Jameson, K. A. Hogquist, T cells expressing the transcription factor PLZF regulate the development of memory-like CD8+ T cells. *Nat Immunol* **11**, 709–716 (2010).
25. A. Drobek, A. Moudra, D. Mueller, M. Huranova, V. Horkova, M. Pribikova, R. Ivanek, S. Oberle, D. Zehn, K. D. McCoy, P. Draber, O. Stepanek, Strong homeostatic TCR signals induce formation of self-tolerant virtual memory CD8 T cells. *EMBO J* **37** (2018).
26. M. A. Weinreich, K. Takada, C. Skon, S. L. Reiner, S. C. Jameson, K. A. Hogquist, KLF2 transcription-factor deficiency in T cells results in unrestrained cytokine production and upregulation of bystander chemokine receptors. *Immunity* **31**, 122–130 (2009).
27. K. R. Renkema, J. Y. Lee, Y. J. Lee, S. E. Hamilton, K. A. Hogquist, S. C. Jameson, IL-4 sensitivity shapes the peripheral CD8+ T cell pool and response to infection. *J Exp Med* **213**, 1319–1329 (2016).
28. T. Sosinowski, J. T. White, E. W. Cross, C. Haluszczak, P. Marrack, L. Gapin, R. M. Kedl, CD8alpha+ dendritic cell trans presentation of IL-15 to naive CD8+ T cells produces antigen-inexperienced T cells in the periphery with memory phenotype and function. *J Immunol* **190**, 1936–1947 (2013).
29. G. Lauvau, S. Goriely, Memory CD8+ T Cells: Orchestrators and Key Players of Innate Immunity? *PLoS Pathog* **12**, e1005722 (2016).
30. C. Shimokawa, T. Kato, T. Takeuchi, N. Ohshima, T. Furuki, Y. Ohtsu, K. Suzue, T. Imai, S. Obi, A. Olia, T. Izumi, M. Sakurai, H. Arakawa, H. Ohno, H. Hisaeda, CD8+ regulatory T cells are critical in prevention of autoimmune-mediated diabetes. *Nat Commun* **11**, 1922 (2020).

31. M. Rifa'i, Y. Kawamoto, I. Nakashima, H. Suzuki, Essential roles of CD8+CD122+ regulatory T cells in the maintenance of T cell homeostasis. *J Exp Med* **200**, 1123–1134 (2004).
32. N. L. Smith, R. K. Patel, A. Reynaldi, J. K. Grenier, J. Wang, N. B. Watson, K. Nzingha, K. J. Yee Mon, S. A. Peng, A. Grimson, M. P. Davenport, B. D. Rudd, Developmental Origin Governs CD8(+) T Cell Fate Decisions during Infection. *Cell*, doi: 10.1016/j.cell.2018.05.029 (2018).
33. Y. Maekawa, Y. Minato, C. Ishifune, T. Kurihara, A. Kitamura, H. Kojima, H. Yagita, M. Sakata-Yanagimoto, T. Saito, I. Taniuchi, S. Chiba, S. Sone, K. Yasutomo, Notch2 integrates signaling by the transcription factors RBP-J and CREB1 to promote T cell cytotoxicity. *Nat Immunol* **9**, 1140–7 (2008).
34. D. Aran, A. P. Looney, L. Liu, E. Wu, V. Fong, A. Hsu, S. Chak, R. P. Naikawadi, P. J. Wolters, A. R. Abate, A. J. Butte, M. Bhattacharya, Reference-based analysis of lung single-cell sequencing reveals a transitional profibrotic macrophage. *Nature Immunology 2019 20:2* **20**, 163–172 (2019).
35. G. La Manno, R. Soldatov, A. Zeisel, E. Braun, H. Hochgerner, V. Petukhov, K. Lidschreiber, M. E. Kastriti, P. Lönnerberg, A. Furlan, J. Fan, L. E. Borm, Z. Liu, D. van Bruggen, J. Guo, X. He, R. Barker, E. Sundström, G. Castelo-Branco, P. Cramer, I. Adameyko, S. Linnarsson, P. V. Kharchenko, RNA velocity of single cells. *Nature 2018 560:7719* **560**, 494–498 (2018).
36. Y. Cao, J. Trillo-Tinoco, R. A. Sierra, C. Anadon, W. Dai, E. Mohamed, L. Cen, T. L. Costich, A. Magliocco, D. Marchion, R. Klar, S. Michel, F. Jaschinski, R. R. Reich, S. Mehrotra, J. R. Cubillos-Ruiz, D. H. Munn, J. R. Conejo-Garcia, P. C. Rodriguez, ER stress-induced mediator C/EBP homologous protein thwarts effector T cell activity in tumors through T-bet repression. *Nat Commun* **10**, 1280 (2019).
37. P. Walter, D. Ron, The Unfolded Protein Response: From Stress Pathway to Homeostatic Regulation. *Science (1979)* **334**, 1081–1086 (2011).
38. K. Haze, H. Yoshida, H. Yanagi, T. Yura, K. Mori, Mammalian Transcription Factor ATF6 Is Synthesized as a Transmembrane Protein and Activated by Proteolysis in Response to Endoplasmic Reticulum Stress. *Mol Biol Cell* **10**, 3787–3799 (1999).
39. P. Gade, G. Ramachandran, U. B. Maachani, M. A. Rizzo, T. Okada, R. Prywes, A. S. Cross, K. Mori, D. V. Kalvakolanu, An IFN-γ–stimulated ATF6–C/EBP-β–signaling pathway critical for the expression of Death Associated Protein Kinase 1 and induction of autophagy. *Proceedings of the National Academy of Sciences* **109**, 10316–10321 (2012).
40. J. Müller, L. Nitschke, The role of CD22 and Siglec-G in B-cell tolerance and autoimmune disease. *Nature Reviews Rheumatology 2014 10:7* **10**, 422–428 (2014).
41. S. J. Meyer, A. T. Linder, C. Brandl, L. Nitschke, B Cell Siglecs–News on Signaling and Its Interplay With Ligand Binding. *Front Immunol* **9** (2018).
42. J. v. Pluvinage, M. S. Haney, B. A. H. Smith, J. Sun, T. Iram, L. Bonanno, L. Li, D. P. Lee, D. W. Morgens, A. C. Yang, S. R. Shuken, D. Gate, M. Scott, P. Khatri, J. Luo, C. R. Bertozzi, M. C. Bassik, T. Wyss-Coray, CD22 blockade restores homeostatic microglial phagocytosis in ageing brains. *Nature* **568**, 187–192 (2019).
43. J. G. Sathish, J. Walters, C. L. Jin, K. G. Johnson, F. G. LeRoy, P. Brennan, K. P. Kim, S. P. Gygi, B. G. Neel, R. J. Matthews, CD22 is a functional ligand for SH2 domain-containing protein-tyrosine phosphatase-1 in primary T cells. *Journal of Biological Chemistry* **279**, 47783–47791 (2004).
44. W. H. Hudson, J. Gensheimer, M. Hashimoto, A. Wieland, R. M. Valanparambil, P. Li, J. X. Lin, B. T. Konieczny, S. J. Im, G. J. Freeman, W. J. Leonard, H. T. Kissick, R. Ahmed, Proliferating Transitory T Cells with an Effector-like Transcriptional Signature

Emerge from PD-1+ Stem-like CD8+ T Cells during Chronic Infection. *Immunity* **51**, 1043-1058.e4 (2019).
45. A. Tarakhovsky, S. B. Kanner, J. Hombach, J. A. Ledbetter, W. Müller, N. Killeen, K. Rajewsky, A Role for CD5 in TCR-Mediated Signal Transduction and Thymocyte Selection. *Science (1979)* **269**, 535–537 (1995).
46. H. S. Azzam, A. Grinberg, K. Lui, H. Shen, E. W. Shores, P. E. Love, CD5 Expression Is Developmentally Regulated By T Cell Receptor (TCR) Signals and TCR Avidity. *Journal of Experimental Medicine* **188**, 2301–2311 (1998).
47. B. D. Stadinski, K. Shekhar, I. Gómez-Touriño, J. Jung, K. Sasaki, A. K. Sewell, M. Peakman, A. K. Chakraborty, E. S. Huseby, Hydrophobic CDR3 residues promote the development of self-reactive T cells. *Nature Immunology 2016 17:8* **17**, 946–955 (2016).
48. S. R. Daley, H. F. Koay, K. Dobbs, M. Bosticardo, R. C. Wirasinha, F. Pala, R. Castagnoli, J. H. Rowe, L. M. Ott de Bruin, S. Keles, Y. N. Lee, R. Somech, S. M. Holland, O. M. Delmonte, D. Draper, S. Maxwell, J. Niemela, J. Stoddard, S. D. Rosenzweig, P. L. Poliani, V. Capo, A. Villa, D. I. Godfrey, L. D. Notarangelo, Cysteine and hydrophobic residues in CDR3 serve as distinct T-cell self-reactivity indices. *Journal of Allergy and Clinical Immunology* **144**, 333–336 (2019).
49. N. N. Logunova, V. V Kriukova, P. V Shelyakin, E. S. Egorov, A. Pereverzeva, N. G. Bozhanova, M. Shugay, D. S. Shcherbinin, M. V Pogorelyy, E. M. Merzlyak, V. N. Zubov, J. Meiler, D. M. Chudakov, A. S. Apt, O. V Britanova, MHC-II alleles shape the CDR3 repertoires of conventional and regulatory naïve CD4+ T cells. *Proc Natl Acad Sci U S A* **117**, 13659–13669 (2020).
50. T. Hogan, A. Shuvaev, D. Commenges, A. Yates, R. Callard, R. Thiebaut, B. Seddon, Clonally diverse T cell homeostasis is maintained by a common program of cell-cycle control. *J Immunol* **190**, 3985–3993 (2013).
51. Q. Ge, A. Bai, B. Jones, H. N. Eisen, J. Chen, Competition for self-peptide-MHC complexes and cytokines between naïve and memory CD8+ T cells expressing the same or different T cell receptors. *Proc Natl Acad Sci U S A* **101**, 3041–3046 (2004).
52. G. Sano, J. C. Hafalla, A. Morrot, R. Abe, J. J. Lafaille, F. Zavala, Swift development of protective effector functions in naive CD8(+) T cells against malaria liver stages. *J Exp Med* **194**, 173–180 (2001).
53. L. Nitschke, R. Carsetti, B. Ocker, G. Köhler, M. C. Lamers, CD22 is a negative regulator of B-cell receptor signalling. *Current Biology* **7**, 133–143 (1997).
54. J. Muller, I. Obermeier, M. Wohner, C. Brandl, S. Mrotzek, S. Angermuller, P. C. Maity, M. Reth, L. Nitschke, CD22 ligand-binding and signaling domains reciprocally regulate B-cell Ca2+ signaling. *Proc Natl Acad Sci U S A* **110**, 12402–12407 (2013).
55. S. Grassmann, L. Mihatsch, J. Mir, A. Kazeroonian, R. Rahimi, S. Flommersfeld, K. Schober, I. Hensel, J. Leube, L. O. Pachmayr, L. Kretschmer, Q. Zhang, A. Jolly, M. Z. Chaudhry, M. Schiemann, L. Cicin-Sain, T. Höfer, D. H. Busch, M. Flossdorf, V. R. Buchholz, Early emergence of T central memory precursors programs clonal dominance during chronic viral infection. *Nat Immunol* **21**, 1563–1573 (2020).
56. M. E. Badr, Z. Zhang, X. Tai, A. Singer, CD8 T cell tolerance results from eviction of immature autoreactive cells from the thymus. *Science (1979)* **382**, 534–541 (2023).
57. J. Li, M. Zaslavsky, Y. Su, J. Guo, M. J. Sikora, V. van Unen, A. Christophersen, S. H. Chiou, L. Chen, J. Li, X. Ji, J. Wilhelmy, A. M. McSween, B. A. Palanski, V. V. A. Mallajosyula, N. A. Bracey, G. K. R. Dhondalay, K. Bhamidipati, J. Pai, L. B. Kipp, J. E. Dunn, S. L. Hauser, J. R. Oksenberg, A. T. Satpathy, W. H. Robinson, C. L. Dekker, L. M. Steinmetz, C. Khosla, P. J. Utz, L. M. Sollid, Y. H. Chien, J. R. Heath, N. Q. Fernandez-Becker, K. C. Nadeau, N. Saligrama, M. M. Davis, KIR+CD8+ T cells

suppress pathogenic T cells and are active in autoimmune diseases and COVID-19. *Science (1979)* **376** (2022).
58. S. C. Jameson, Y. J. Lee, K. A. Hogquist, Innate memory T cells. *Adv Immunol* **126**, 173–213 (2015).
59. G. Galletti, G. de Simone, E. M. C. Mazza, S. Puccio, C. Mezzanotte, T. M. Bi, A. N. Davydov, M. Metsger, E. Scamardella, G. Alvisi, F. de Paoli, V. Zanon, A. Scarpa, B. Camisa, F. S. Colombo, A. Anselmo, C. Peano, S. Polletti, D. Mavilio, D. M. Baird, E. Gostick, S. Llewellyn-lacey, K. Ladell, D. A. Price, Two subsets of stem-like CD8+ memory T cell progenitors with distinct fate commitments in humans Giovanni. *Nat Immunol*, doi: 10.1038/s41590-020-0791-5.
60. T. Sekine, A. Perez-Potti, S. Nguyen, J.-B. Gorin, V. H. Wu, E. Gostick, S. Llewellyn-Lacey, Q. Hammer, S. Falck-Jones, S. Vangeti, M. Yu, A. Smed-Sörensen, A. Gaballa, M. Uhlin, J. K. Sandberg, C. Brander, P. Nowak, P. A. Goepfert, D. A. Price, M. R. Betts, M. Buggert, "TOX is expressed by exhausted and polyfunctional human effector memory CD8 + T cells" (2020).
61. T. Wen, M. K. Mingler, C. Blanchard, B. Wahl, O. Pabst, M. E. Rothenberg, The Pan-B Cell Marker CD22 Is Expressed on Gastrointestinal Eosinophils and Negatively Regulates Tissue Eosinophilia. *The Journal of Immunology* **188**, 1075–1082 (2012).
62. C. Akatsu, A. A. Deh Sheikh, N. Matsubara, H. Takematsu, A. Schweizer, H. H. M. Abdu-Allah, T. F. Tedder, L. Nitschke, H. Ishida, T. Tsubata, The inhibitory coreceptor CD22 restores B cell signaling by developmentally regulating Cd45−/− immunodeficient B cells. *Sci Signal* **15** (2022).
63. E. Ventre, L. Brinza, S. Schicklin, J. Mafille, C.-A. A. Coupet, A. Marcais, S. Djebali, V. Jubin, T. Walzer, J. Marvel, Negative regulation of NKG2D expression by IL-4 in memory CD8 T cells. *J Immunol* **189**, 3480–3489 (2012).
64. K. G. C. Smith, D. M. Tarlinton, G. M. Doody, M. L. Hibbs, D. T. Fearon, Inhibition of the B cell by CD22: a requirement for Lyn. *J Exp Med* **187**, 807–811 (1998).
65. H. J. Kim, X. Wang, S. Radfar, T. J. Sproule, D. C. Roopenian, H. Cantor, CD8+ T regulatory cells express the Ly49 Class I MHC receptor and are defective in autoimmune prone B6-Yaa mice. *Proc Natl Acad Sci U S A* **108**, 2010–2015 (2011).
66. A. Levescot, N. Cerf-Bensussan, Regulatory CD8 $^{+}$ T cells suppress disease. *Science (1979)* **376**, 243–244 (2022).
67. T. Bouchery, B. Volpe, K. Shah, L. Lebon, K. Filbey, G. LeGros, N. Harris, The Study of Host Immune Responses Elicited by the Model Murine Hookworms *Nippostrongylus brasiliensis* and *Heligmosomoides polygyrus*. *Curr Protoc Mouse Biol* **7**, 236–286 (2017).
68. G. A. Russell, G. Peng, C. Faubert, E. F. Verdu, S. Hapfelmeier, I. L. King, A protocol for generating germ-free Heligmosomoides polygyrus bakeri larvae for gnotobiotic helminth infection studies. *STAR Protoc* **2**, 100946 (2021).
69. E. Montecino-Rodriguez, K. Dorshkind, Use of Busulfan to Condition Mice for Bone Marrow Transplantation. *STAR Protoc* **1**, 100159 (2020).

Acknowledgements

We thank S. Li for his help in GSEA analyses, L. Gillet for insightful discussions, and the technician and administrative team of the Immunology-Vaccinology laboratory, and L. Karim and members of the GIGA Genomics platform. The MCMV BAC clone pSM3r 3.3 was obtained under material transfer agreement from L. Cicin Sain. We also thank C. Faubert at the MI4 Gnotobiotic Animal Research Platform for her expertise and assistance with the germ-free helminth infections. The following tetramers were obtained through the NIH Tetramer Facility: H-2D^{b}-ORF6$^{487-495}$, H-2K^{b}-ORF61$^{524-531}$. *B. glabrata* snails were provided by Dr J. Vicogne, Institut Pasteur Lille, France.

Funding: B.Y. is supported by the Chinese Scholarship Council. G.S.S. is supported by Télévie-FNRS (7.4586.19 and 922 7.6529.21). A.M.A. is supported by a doctoral training award from FRQS. D.V. FNRS CDR (CDR_J.0225.20) and WELBIO (WELBIO-CR-2022 A – 15). B.G.D. is supported by FNRS CDR (CDR/OL J.0062.20), ULiège (FSR-S-SS-19/43 and ARC 19-23/11) and WELBIO (WELBIO-ADV X.1515.24). This work was supported by the Canadian Institutes of Health Research (PJT-362757). H.S.N. holds a Canada Research Chair in Systems Biology of Gene Regulation. I.L.K. holds a Canada Research Chair in Barrier Immunity. G.P. and L.R.R. are Research fellows, and B.G.D. is an honorary Senior Research Associate of the Fonds de la Recherche Scientifique (F.R.S.-FNRS).

Author Contributions: B.Y. designed and performed the experiments, analyzed the data, and wrote the paper. G.S.S. performed TCR sequencing, CDR3 analyses and contributed to the manuscript preparation. O.P., M.G., G.P., G.P., L.R.R. and B.K. performed the experiments and analyzed the data. G.V.I. and J.V.D. performed the ImageStream analyses. S.J.M. prepared bone marrow cells from *Cd22*$^{-/-}$ and *Cd22*^{Y2,5,6F} mice. A.L., A.M and Q.B. provided support for the analysis of RNA sequencing data. B.M. supervised mouse breeding and provided the GREAT mice and contributed to manuscript preparation. T.M. contributed to manuscript preparation. D.V., H.S.N., I.K. contributed the design of experiments and to the manuscript preparation. L.N. supervised mouse breeding and provided the CD22 knockout mice and contributed to manuscript preparation. B.G.D. planned and supervised the work, acquired funding, designed experiments, prepared the figures and wrote the paper.

Competing interests: The authors have no competing interests.

Data and materials availability: Sequencing data have been deposited to GEO under accession number GSE228564. All other data needed to support the conclusions of the paper are present in the paper or the Supplementary Materials. Underlying tabulated data for all figures can be found in supplementary data file S1.

Figure legends

Figure 1. Impaired peripheral T_{VM} expansion in IL-4Rα$^{\Delta CD8}$ mice during helminth infection.

(**A**) Representative flow plot of TCRβ$^+$ thymocytes (left) and CD124 MFI (right)
(**B**) Representative flow plot of SP8 thymocytes and representative histogram of CD24$^-$ SP8 thymocytes (left) and quantification (right).
(**C**) Representative flow plot and histogram of CD3$^+$CD8$^+$ T splenocytes (left) and quantification of CD124 MFI (right).
(**D**) Quantification of indicated populations (cell numbers).
(**E**) Representative flow plot of splenic CD8$^+$ T lymphocytes.
(**F**) Representative flow plot of splenic CD8$^+$ T lymphocytes (left) and quantification of CD124$^+$ and CD124$^-$ percentages in CD44^{low} T_{NAIVE} or CD49d^{low}CXCR3$^+$ T_{VM} (right)
(**G-H**) Quantification of cell numbers, percentages, and MFI of EOMES of the indicated populations in the thymus (**G**) or the spleen (**H**) in mice at d4 post injection with IL-4c.
(**I**) Quantification of CD124$^+$ and CD124$^-$ CD8$^+$ T cells from the spleen.
(**J**) Quantification of T_{VM} percentages in the spleen after injection with IL-4c, at d15 after *H. polygyrus* infection, and at d22 after injection of *S. mansoni* eggs.
(**K**) Quantification of T_{VM} percentages in CD124$^+$ and CD124$^-$ CD8$^+$ T cells in IL-4Rα$^{\Delta CD8}$ mice, based on the results in (**J**).
(**L**) Intestinal worm burden at d15 after *H. polygyrus* infection.
(**M**) Quantification of thoracic luminescence signals after MuHV-4-Luc infection after PBS or injection with IL-4c.
Statistical significance calculated using Mann-Whitney test (A), unpaired t-test (B-D, L) or two-way analysis of variance (ANOVA) and Tukey's (F-I, M) or Sidak's (K) multiple comparisons test. Data are representative of 2 to 3 independent experiments with 3-8 mice per group. Mean ± s.e.m., each symbol represents one individual mouse. MFI = median fluorescence intensity. $^{\#}$: when compared with PBS group.

Figure 2. Single-cell RNA sequencing reveals a T_{VM} cluster.

(**A**) UMAP visualization of unsupervised Seurat clustering analysis of combined 33,553 single CD8$^+$ T cell transcriptomes of IL-4Rα^{WT} or IL-4Rα$^{\Delta CD8}$ mice based on the experimental design in Fig. S2a.
(**B**) Supervised SingleR clustering analysis to identify naive, memory and effector T cell clusters. The pie chart shows the cell number proportion of each cluster.
(**C**) Heat map of row-wise *z*-score-normalized expression for 394 cluster-specific differentially expressed genes used to establish the SingleR clustering in (b). Rows are ordered by hierarchical clustering. Genes for biologically relevant example genes for each cluster are shown.
(**D**) UMAP visualization of unsupervised Seurat clustering analysis of combined 8,198 single memory and effector CD8$^+$ T cell transcriptomes of IL-4Rα^{WT} or IL-4Rα$^{\Delta CD8}$ mice (n=29), based on SingleR clustering in (b). Cluster labels indicate selected differentially expressed genes.
(**E**) Heat map of row-wise *z*-score-normalized expression for 1266 cluster-specific differentially expressed genes used to establish the Seurat clustering analysis in (d). Columns represent the average expression for each cluster.
(**F**) Violin plots show normalized expression in each cluster of 14 cluster-specific signature genes.
Data represent one experiment including 29 mice (4-5 mice per group).

Figure 3. Single-cell transcriptomic analysis of spleen T_{VM} upon IL-4 response.
(**A**) Split UMAP visualization of supervised SingleR clustering analysis of combined $CD8^+$ T cell transcriptomes of IL-4Rα^{WT} and IL-4R$\alpha^{\Delta CD8}$ mice, following treatment with PBS, IL-4c, or *H. polygyrus* infection. Percent of cells in cluster T-memory is indicated for each dataset.
(**B**) Violin plots show normalized expression in the T-memory cluster of selected signature genes. Each dot represents a single cell included in the T-memory cluster and expressing the given gene. The color scale represents the percentage of cells within each cluster expressing the given gene, excluding cells with no expression.
(**C**) Split UMAP visualization of T-memory and T-effector SingleR clustering, highlighting cluster 2 (C2) as identified in Fig. 2d.
(**D**) Scatter plot shows the $\log_2$ fold change of selected biologically relevant genes between IL-4c vs. PBS (x-axis) and *H. polygyrus* vs. PBS (y-axis) mice among cells in cluster 2 from memory/effector SingleR analysis in Fig. 2D. Data are from IL-4Rα^{WT} mice. Each dot represents one gene. The color scale indicates normalized expression. The size of the dot indicates statistical significance.
(**E**) Violin plots show normalized expression in cluster 2 of six selected signature genes. Each dot represents a single cell included in cluster 2 and expressing the given gene. Data are from IL-4Rα^{WT} mice. The color scale represents the percentage of cells within each cluster expressing the given gene, excluding cells with no expression.
Data represent one experiment including 29 mice (4-5 mice per group). *P* values were obtained using the FindMarkers function in Seurat (see Supplementary Materials).

Figure 4. Gene expression signature of T_{VM} in the mesLN after helminth infection.
(**A-B**) Quantification of total leukocytes (top), $CD8^+$ T cell numbers (middle) and T_{VM} percentages (bottom) in the spleen (**A**) and mesLN (**B**) at d15 after *H. polygyrus* infection.
(**C**) Representative contour plots of CD124 expression of concatenated samples, based on the experimental condition. Quantification of median fluorescence intensities (MFI) of EOMES expression in $CD124^+$ or $CD124^-$ cells are shown.
(**D**) Split UMAP visualization of combined 6,808 single $CD8^+$ T cell transcriptomes obtained by scRNA-seq analysis of FACS-sorted then pooled sample tagged $CD124^+$ and $CD124^-$ $CD8^+$ T cells from mesLN of IL-4R$\alpha^{\Delta CD8}$ mice at d15 after *H. polygyrus* infection (n=3).
(**E**) UMAP visualization of Seurat clustering analysis. Clusters 1 and 5 labels indicate selected differentially expressed genes.
(**F**) Dot plot representation of the top 5 upregulated gene expression in each cluster, based on (E).
(**G**) FeaturePlot representation of selected gene expression in single $CD8^+$ T cells, based on (F).
Statistical significance calculated using two-way analysis of variance (ANOVA) and Tukey's multiple comparison-test (A-C). Data are representative of three independent experiments with 3-4 mice per group. Mean ± s.e.m., each symbol represents one individual mouse. Data are representative of two independent experiments including 3-5 mice per group.

Figure 5. Specific CD22 expression in IL-4-induced T_{VM}.
(**A**) Feature plot of *Cd22* expression in memory/effector single $CD8^+$ T cell transcriptome.
(**B**) Representative flow plot of CD22 surface staining on spleen T_{VM} from BALB/c mice. Numbers indicate percent of events in each gate.
(**C**) Imaging cytometry of single splenic $CD8^+$ T cells co-stained for CD3ε, CD8α and CD22 (×60, scale bar, 7 μm)
(**D**) Representative flow cytometry analysis of spleen cells from PBS or IL-4c-treated WT BALB/c mice. Back-gating of $CD22^+CD8^+$ T cells (left) and quantification of $CD22^+$ cells in T cell subpopulations (right) are shown.

(**E-F**) Quantification of $CD22^+$ T cell percentages (left) and numbers (right) in spleen (E) and mesLN (F).
(**G**) Representative flow plot of CD22 and CD124 co-expression of spleen T_{VM}. Numbers indicate percent of events in each quadrant.
(**H**) Quantification of $CD22^+$ T_{VM} percentages based on the expression of IL-4Rα (CD124). In IL-4R$\alpha^{\Delta CD8}$ mice, percentages of $CD22^+$ T_{VM} were reported to $CD124^-$ $CD8^+$ T cells.
(**I**) Quantification of $CD22^+$ T_{VM} percentages in the spleen of WT and *Il4ra*$^{-/-}$ BALB/c mice (left), and WT, *Il4ra*$^{-/-}$ and *Stat6*$^{-/-}$ C57BL/6 mice (right).
(**J**) Quantification of donor T_{VM} (left) and $CD22^+$ T_{VM} (right) percentages in the spleen of BM mixed chimeric mice. BM chimeras were generated by transferring WT ($CD45.1^+Thy1.2^+$) and *Il4ra*$^{-/-}$ ($CD45.2^+Thy1.2^+$) BML cells into $CD45.2^+Thy1.1^+$ BALB/c mice.
Data at d4 after injection with PBS or IL-4c, and at d15 after *H. polygyrus* infection are shown. Statistical significance calculated using two-way analysis of variance (ANOVA) and Tukey's (E-I) or Sidak's (J) multiple comparisons test. Data are representative of 2 to 3 independent experiments with 3-9 mice per group (mean ± s.e.m.).

Figure 6. $CD22^+$ T_{VM} are transcriptionally distinct from $CD22^-$ T_{VM} and naive T cells.
(**A-D**) WT BALB/c mice were treated with PBS or IL-4c before spleen harvest and purification of $CD44^{low}$ T_{NAIVE} and $CD22^-$ and $CD22^+$ $CD44^{high}CD49d^{low}$ T_{VM} for RNA-seq analysis.
(**A**) Unsupervised hierarchical clustering of the top 250 differentially expressed genes. Specific biologically relevant example genes are listed on the left. Heatmap color scale indicates *z*-score.
(**B**) Heatmap of biologically relevant example gene expression. Color scale indicates normalized mean expression.
(**C**) GSEA enrichment score plots for the indicated KEGG or HALLMARK gene sets between $CD22^-$ and $CD22^+$ T_{VM} in IL-4c treated mice.
(**D**) MA plot of differentially expressed genes between $CD22^-$ and $CD22^+$ T_{VM} in IL-4c treated mice. Each dot represents one gene. Manually curated genes are indicated.
(**E**) Flow plots of concatenated results of 4 mice and quantification of the MFI of selected markers in spleen $CD44^{low}$ T_{NAIVE}, $CD22^-$ T_{VM} and $CD22^+$ T_{VM} of IL-4c-treated WT BALB/c mice.
(**F**) Experimental design of IL-4c and EdU administration before spleen harvest.
(**G**) Flow plot of $CD8^+$ T cells and $CD49d^{low}$ T_{VM}, obtained from concatenated results of 4 to 5 mice, split by experimental conditions. Numbers indicate percent of events in each gate.
(**H**) Quantification of percentage of EdU^+ cells in $CD8^+$ T cells (top), T_{VM} (middle), and $CD22^{+/-}$ T_{VM} (bottom) are shown.
Statistical significance calculated using two-way analysis of variance (ANOVA) with Tukey's (E) or Sidak's (H, bottom) multiple comparison test or unpaired t test (H). Each symbol represents an individual mouse. Data are representative of one (A-D) to three independent (E-H) experiments with 4-5 mice per group. MFI: median fluorescence intensity.

Figure 7. Enriched self-reactive CDR3 sequences in IL-4-induced $CD22^+$ T_{VM}.
(**A**) Heatmap of biologically relevant genes from publicly accessible dataset (*21*). Color scale indicates normalized mean expression.
(**B-H**) WT BALB/c mice were treated with PBS or IL-4c before spleen harvest and purification of $CD44^{low}$ T_{NAIVE} and $CD22^-$ and $CD22^+$ $CD44^{high}CD49d^{low}$ T_{VM} for RNA extraction. CDR3α and CDR3β sequences were extracted from RNA-seq and TCR-seq.
(**B**) Tree maps of CDR3 clonotype usage. Each rectangle represents one CDR3 clonotype and its size corresponds to its relative frequency in the repertoire (colors are chosen randomly and do not match between plots).
(**C**) Normalized Shannon diversity index of TRA and TRB. Mean ± s.e.m. is indicated.

(**D-E**) Quantification of hydrophobic doublets in positions 6 and 7 of CDR3α and CDR3β in T cell subsets from all experimental conditions (D) or of paired samples in IL-4c-treated mice (E).
(**F-G**) Quantification of CDR3 strength based on the presence of bulky amino acid side chains for CDR3α and CDR3β in T cell subsets from all experimental conditions (F) or of paired samples in IL-4c-treated mice (G).
(**H**) Cumulative contribution of 18 CDR3-derived parameters in PCA for the repertoires of the studied T cell subsets, plotted as two-dimensional PCA projections of 5,000 functional CDR3 read sequences, randomly selected.
(**I**) Representative flow plot (left) and quantification (right) of $CD22^+$ T_{VM} percentages in WT, CSP- or OT-I TCR transgenic mice.
CDR3 sequence reads were obtained by TCR-seq (B-C) or combined RNA-seq and TCR-seq (D, H). Statistical significance calculated using one-way analysis of variance (ANOVA) and Holm-Sidak's (C,I), Dunnet's (D,F), or Tukey's (E,G) multiple comparison test. Sequencing data are representative of two independent experiments with 6 (TCR-seq) and 4 (RNA-seq) mice per group. Panel I is representative of two independent experiments with 2-4 mice per group (mean ± s.e.m.).

Figure 8. CD22 controls the effector program of activation of T_{VM}.
(**A-B**) Quantification of T_{VM} numbers (**A**) and $EOMES^+$, $CD39^+$ or $GZMA^+$ T_{VM} percentages (**B**) after injection with IL-4c.
(**C**) Quantification of T_{VM} numbers at d15 after *H. polygyrus* infection.
(**D**) Quantification of T_{VM} (left), and $EOMES^+$, $CD39^+$ and $GZMA^+$ T_{VM} in the donor compartment of WT:$Cd22^{-/-}$ mixed BM chimeric mice.
(**E**) Quantification of T_{VM} (left), $CD22^+$ T_{VM}, $EOMES^+$, $CD39^+$ and $GZMA^+$ cells in T_{VM} in the donor compartment of WT:$Cd22^{Y2,5,6F}$ mixed BM chimeric mice.
(**F-H**) WT:$Cd22^{-/-}$ mixed BM chimeric mice were injected with PBS or IL-4c before IAV infection. (**F**) $CD8^+$ T cells chimerism before (left) or at d6 after infection (right). (**G**) Quantification of $GZMA^+$, $GZMB^+$ and $CD39^+$ T cells in the BALF at d6 after infection. (**H**) Quantification of IFN-γ^+ T cells after *ex vivo* stimulation of lung cells at d6 after infection.
(**I-K**) WT:$Cd3e^{-/-}$ and $Cd22^{-/-}$:$Cd3e^{-/-}$ BM chimeric mice were injected with IL-4c before IAV infection. (**I**) Relative body weight changes after infection. (**J-K**) Quantification of $CD8^+$ T cell numbers (**K**) and IFN-γ^+ T cells (**K**) after *ex vivo* stimulation of lung cells at d7 after infection.
(**L**) Quantification of $Thy1.1^+V\beta8.1^+$ cells after T-cell transfer and MCMV-$ie2^{CSP}$ viral infection.
(**M**) Representative flow plots (left) and quantification of splenic $Ly49^+$ T cells and T_{VM}. Numbers indicate percent of events in each gate.
(**N**) Relative body weight changes of $Rag2^{-/-}$ mice co-transferred with $CD25^-CD45RB^{hi}CD4^+$ T cells and IL-4-induced $CD22^+$ or $CD22^-$ T_{VM}.
Statistical significance calculated using Mann-Whitney test (A,J,K), two-way analysis of variance (ANOVA) and Tukey's (B,C,L,N) or Sidak's (D-I) multiple comparison test, or unpaired t test (M). Each symbol represents an individual mouse. Data are representative of 2 to 3 independent experiments including 3 to 6 mice per group (means ± s.e.m.). Lines in panels D-F connect data of both CD45.1 or CD45.2 compartments of an individual mouse.

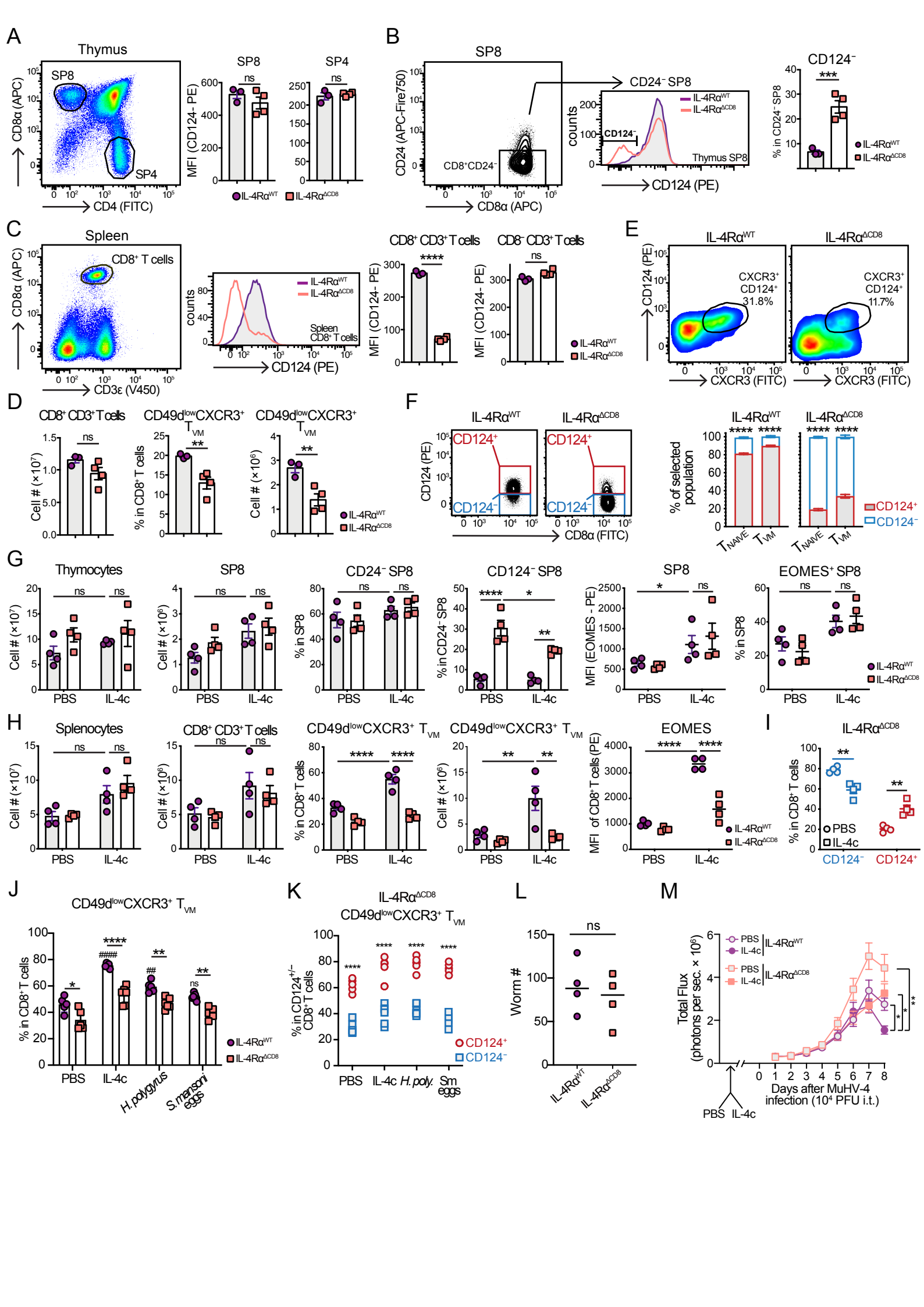
A
Thymus
SP8
SP4
CD8α (APC)
CD4 (FITC)
SP8
SP4
MFI (CD124- PE)
ns
IL-4Rα^WT
IL-4Rα^ΔCD8
B
SP8
CD24 (APC-Fire750)
CD8α (APC)
CD8⁺CD24⁻
CD24⁻ SP8
counts
CD124⁻
Thymus SP8
CD124 (PE)
CD124⁻
***
% in CD24⁻ SP8
C
Spleen
CD8⁺ T cells
CD8α (APC)
CD3ε (V450)
counts
Spleen CD8⁺ T cells
CD124 (PE)
CD8⁺ CD3⁺ T cells
CD8⁻ CD3⁺ T cells
****
MFI (CD124- PE)
E
IL-4Rα^WT
IL-4Rα^ΔCD8
CXCR3⁺ CD124⁺ 31.8%
CXCR3⁺ CD124⁺ 11.7%
CD124 (PE)
CXCR3 (FITC)
D
CD8⁺ CD3⁺ T cells
CD49d^low CXCR3⁺ T_VM
Cell # (×10⁷)
% in CD8⁺ T cells
Cell # (×10⁶)
F
IL-4Rα^WT
IL-4Rα^ΔCD8
CD124⁺
CD124⁻
CD124 (PE)
CD8α (FITC)
% of selected population
T_NAIVE
T_VM
G
Thymocytes
SP8
CD24⁻ SP8
CD124⁻ SP8
SP8
EOMES⁺ SP8
Cell # (×10⁷)
Cell # (×10⁶)
% in SP8
% in CD24⁻ SP8
MFI (EOMES - PE)
PBS
IL-4c
H
Splenocytes
CD8⁺ CD3⁺ T cells
CD49d^low CXCR3⁺ T_VM
CD49d^low CXCR3⁺ T_VM
EOMES
Cell # (×10⁷)
Cell # (×10⁶)
% in CD8⁺ T cells
MFI of CD8⁺ T cells (PE)
I
IL-4Rα^ΔCD8
% in CD8⁺ T cells
PBS
IL-4c
CD124⁻
CD124⁺
J
CD49d^low CXCR3⁺ T_VM
% in CD8⁺ T cells
PBS
IL-4c
H.polygyrus
S.mansoni eggs
K
IL-4Rα^ΔCD8
CD49d^low CXCR3⁺ T_VM
% in CD124^+/- CD8⁺ T cells
PBS
IL-4c
H.poly.
Sm eggs
CD124⁺
CD124⁻
L
Worm #
M
Total Flux (photons per sec. × 10⁶)
PBS
IL-4c
Days after MuHV-4 infection (10⁴ PFU i.t.)

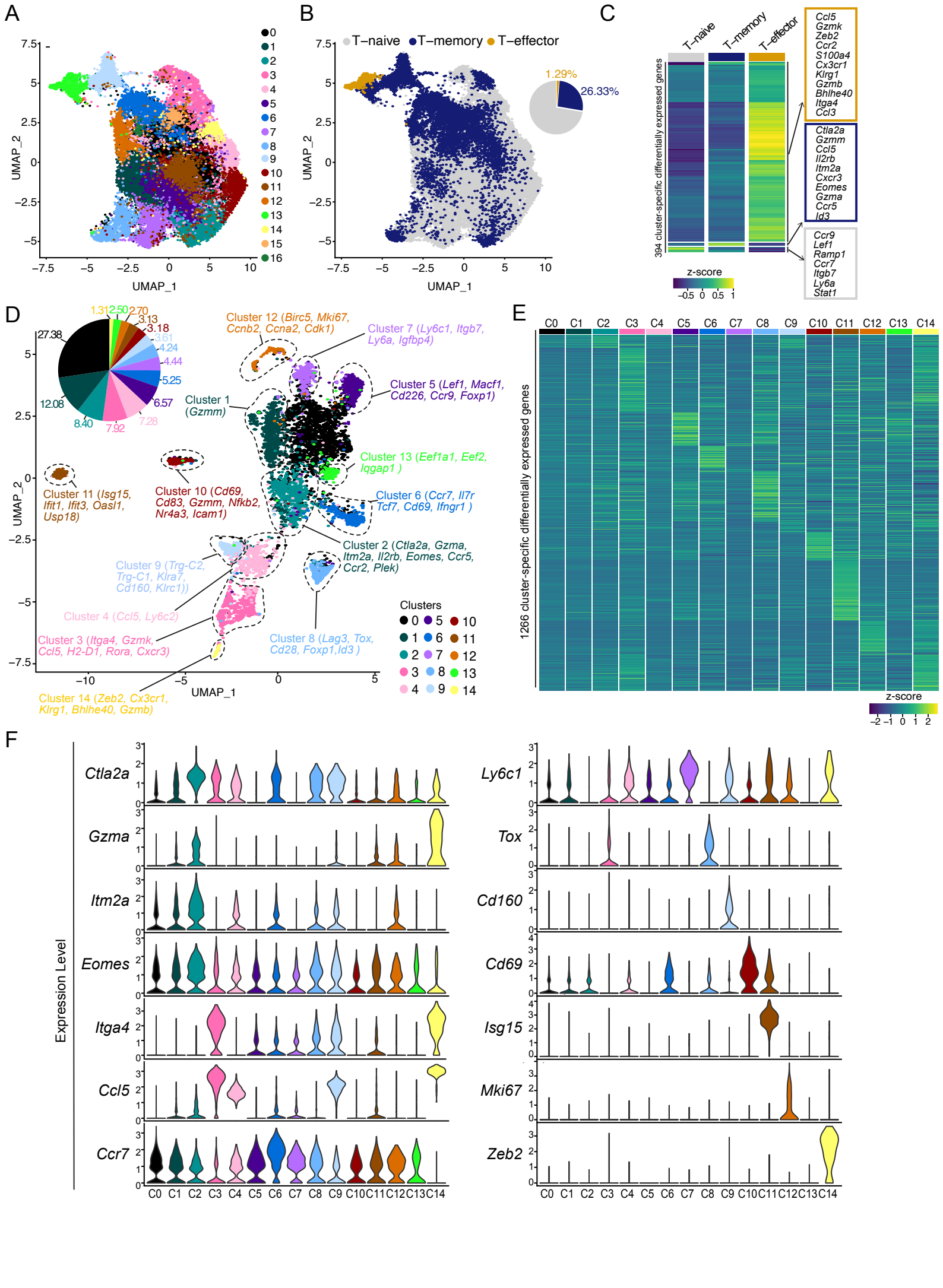
A
B
C
D
E
F
UMAP_1
UMAP_2
T−naive
T−memory
T−effector
1.29%
26.33%
394 cluster-specific differentially expressed genes
z-score
Ccl5 Gzmk Zeb2 Ccr2 S100a4 Cx3cr1 Klrg1 Gzmb Bhlhe40 Itga4 Ccl3
Ctla2a Gzmm Ccl5 Il2rb Itm2a Cxcr3 Eomes Gzma Ccr5 Id3
Ccr9 Lef1 Ramp1 Ccr7 Itgb7 Ly6a Stat1
Cluster 1 (Gzmm)
Cluster 2 (Ctla2a, Gzma, Itm2a, Il2rb, Eomes, Ccr5, Ccr2, Plek)
Cluster 3 (Itga4, Gzmk, Ccl5, H2-D1, Rora, Cxcr3)
Cluster 4 (Ccl5, Ly6c2)
Cluster 5 (Lef1, Macf1, Cd226, Ccr9, Foxp1)
Cluster 6 (Ccr7, Il7r Tcf7, Cd69, Ifngr1)
Cluster 7 (Ly6c1, Itgb7, Ly6a, Igfbp4)
Cluster 8 (Lag3, Tox, Cd28, Foxp1,Id3)
Cluster 9 (Trg-C2, Trg-C1, Klra7, Cd160, Klrc1))
Cluster 10 (Cd69, Cd83, Gzmm, Nfkb2, Nr4a3, Icam1)
Cluster 11 (Isg15, Ifit1, Ifit3, Oasl1, Usp18)
Cluster 12 (Birc5, Mki67, Ccnb2, Ccna2, Cdk1)
Cluster 13 (Eef1a1, Eef2, Iqgap1)
Cluster 14 (Zeb2, Cx3cr1, Klrg1, Bhlhe40, Gzmb)
Clusters
1266 cluster-specific differentially expressed genes
Expression Level
Ctla2a
Gzma
Itm2a
Eomes
Itga4
Ccl5
Ccr7
Ly6c1
Tox
Cd160
Cd69
Isg15
Mki67
Zeb2

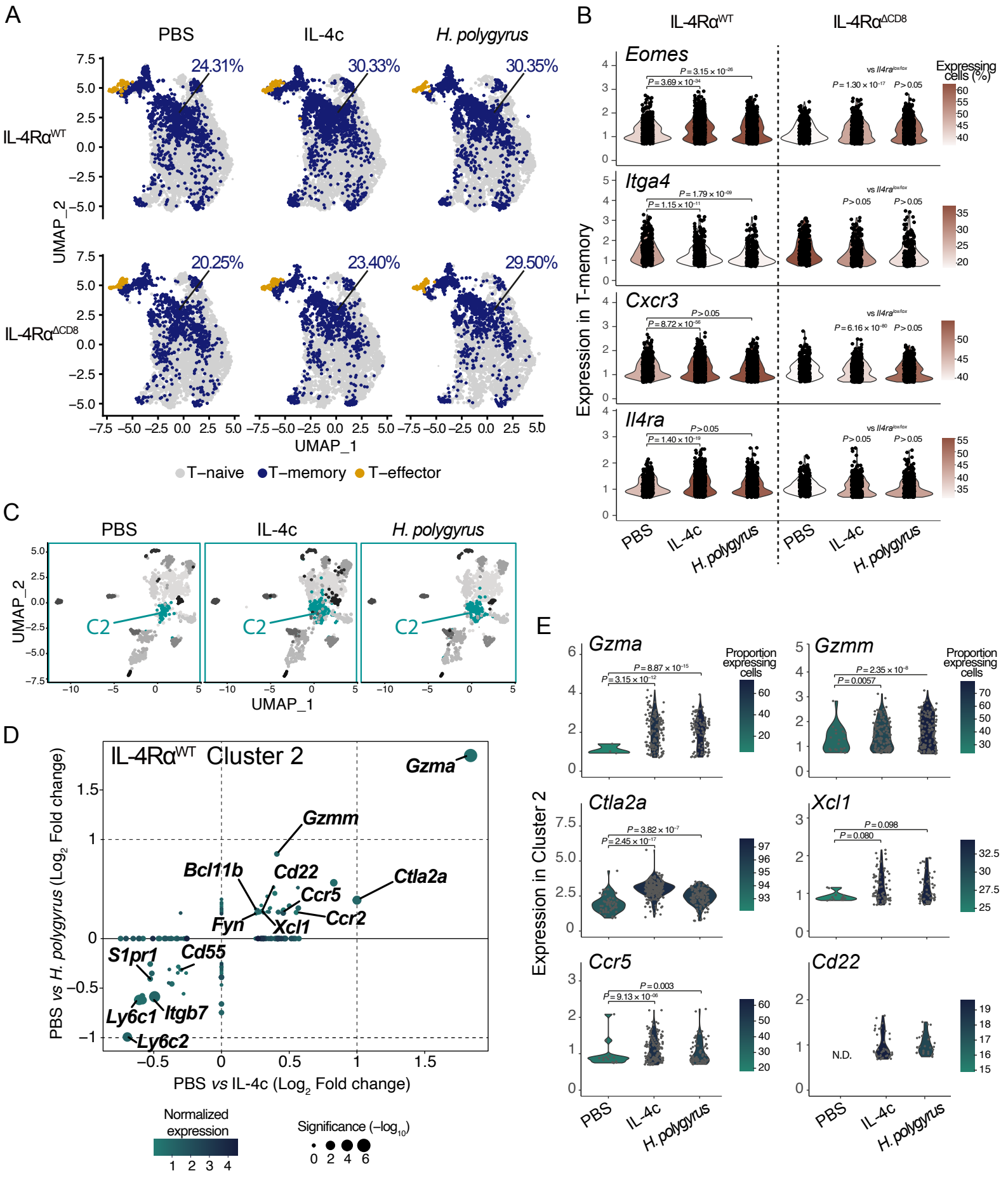
A
PBS
IL-4c
H. polygyrus
IL-4Rα^WT
IL-4Rα^ΔCD8
24.31%
30.33%
30.35%
20.25%
23.40%
29.50%
UMAP_2
UMAP_1
T–naive
T–memory
T–effector
B
IL-4Rα^WT
IL-4Rα^ΔCD8
Eomes
Itga4
Cxcr3
Il4ra
Expression in T-memory
Expressing cells (%)
vs Il4ra^lox/lox
PBS
IL-4c
H. polygyrus
C
PBS
IL-4c
H. polygyrus
C2
UMAP_2
UMAP_1
D
IL-4Rα^WT Cluster 2
Gzma
Gzmm
Bcl11b
Cd22
Ctla2a
Ccr5
Fyn
Xcl1
Ccr2
S1pr1
Cd55
Itgb7
Ly6c1
Ly6c2
PBS vs H. polygyrus (Log2 Fold change)
PBS vs IL-4c (Log2 Fold change)
Normalized expression
Significance (–log10)
E
Gzma
Gzmm
Ctla2a
Xcl1
Ccr5
Cd22
Expression in Cluster 2
Proportion expressing cells
N.D.
PBS
IL-4c
H. polygyrus

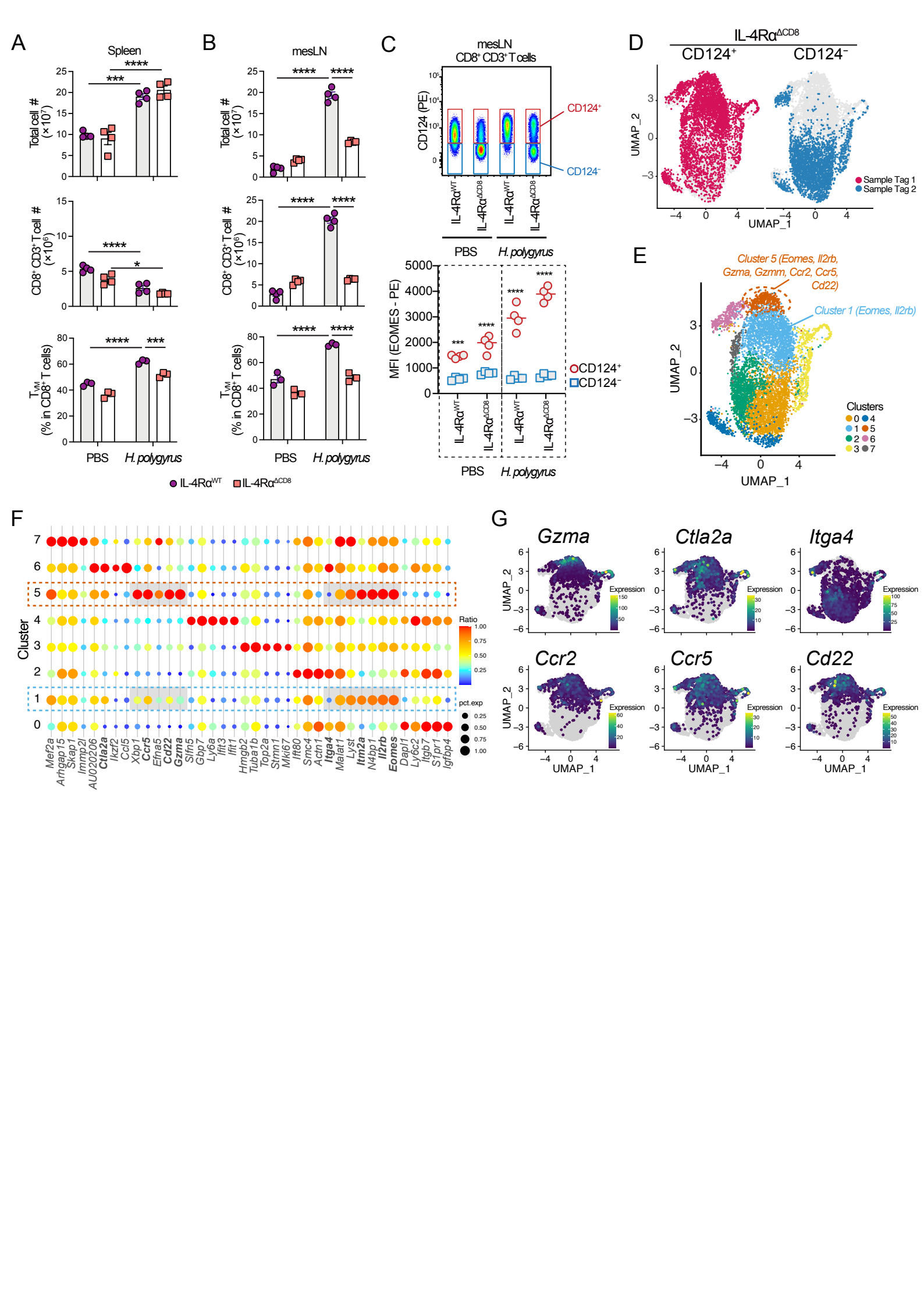
A
Spleen
Total cell # (×10^7)
CD8+ CD3+ T cell # (×10^6)
TVM (% in CD8+ T cells)
PBS
H. polygyrus
B
mesLN
C
mesLN
CD8+ CD3+ T cells
CD124 (PE)
CD124+
CD124−
IL-4Rα^WT
IL-4Rα^ΔCD8
MFI (EOMES - PE)
D
IL-4Rα^ΔCD8
CD124+
CD124−
UMAP_2
UMAP_1
Sample Tag 1
Sample Tag 2
E
Cluster 5 (Eomes, Il2rb, Gzma, Gzmm, Ccr2, Ccr5, Cd22)
Cluster 1 (Eomes, Il2rb)
Clusters
F
Cluster
Ratio
pct.exp
Mef2a
Arhgap15
Skap1
Immp2l
AU020206
Ctla2a
Ikzf2
Ccl5
Xbp1
Ccr5
Efna5
Cd22
Gzma
Slfm5
Gbp7
Ly6a
Ifit3
Ifit1
Hmgb2
Tuba1b
Top2a
Stmn1
Mki67
Ift80
Smc4
Actn1
Itga4
Malat1
Lyst
Itm2a
N4bp1
Il2rb
Eomes
Dapl1
Ly6c2
Itgb7
S1pr1
Igfbp4
G
Gzma
Ctla2a
Itga4
Ccr2
Ccr5
Cd22
Expression
UMAP_2
UMAP_1

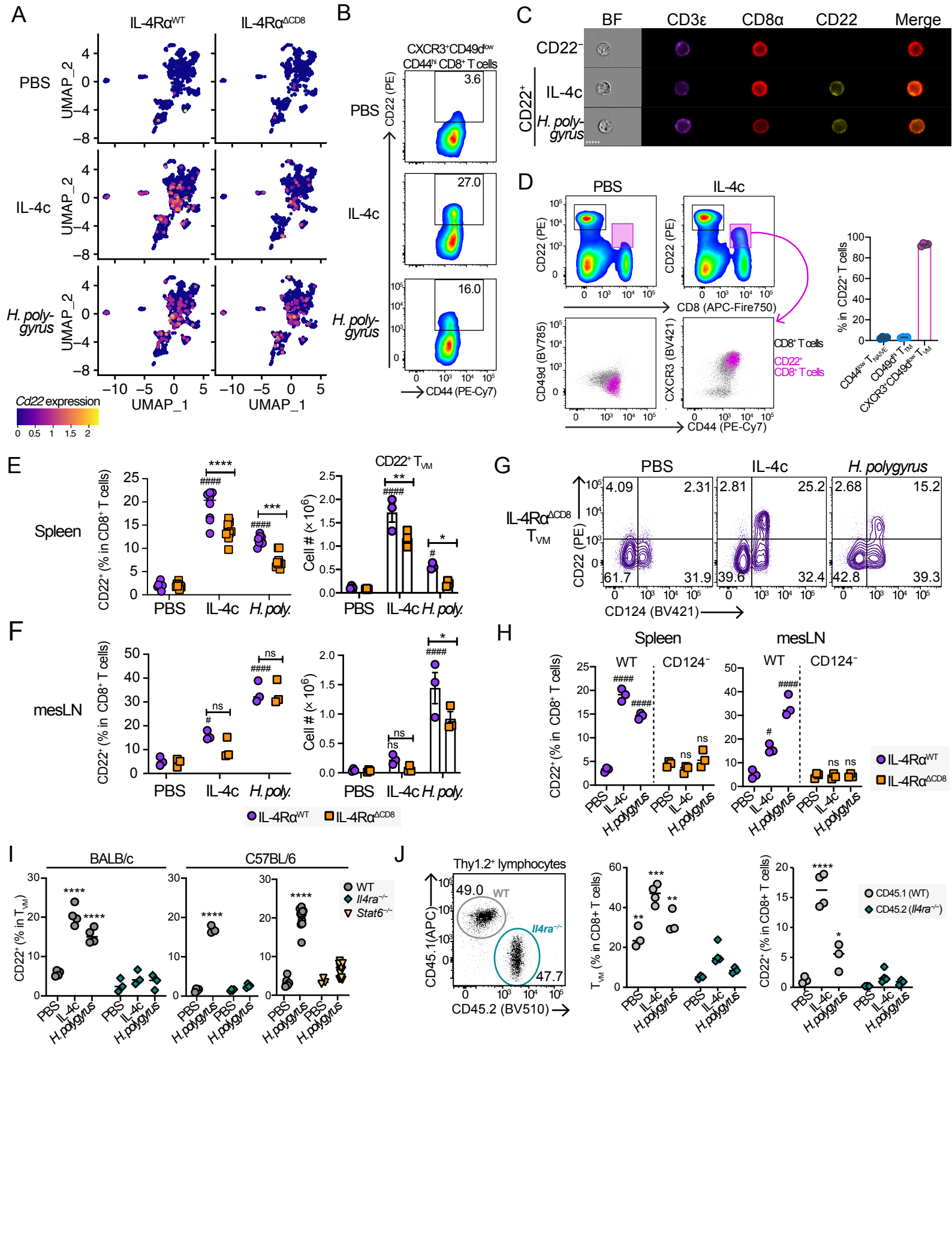
A
IL-4Rα^WT
IL-4Rα^ΔCD8
PBS
IL-4c
H. poly-gyrus
UMAP_2
UMAP_1
Cd22 expression
B
CXCR3+CD49dlow CD44hi CD8+ T cells
CD22 (PE)
CD44 (PE-Cy7)
3.6
27.0
16.0
C
BF
CD3ε
CD8α
CD22
Merge
CD22−
CD22+
IL-4c
H. poly-gyrus
D
PBS
IL-4c
CD22 (PE)
CD8 (APC-Fire750)
CD49d (BV785)
CXCR3 (BV421)
CD44 (PE-Cy7)
CD8+ T cells
CD22+ CD8+ T cells
% in CD22+ T cells
CD44low TNAIVE
CD49dhi TTM
CXCR3+CD49dlow TVM
E
Spleen
CD22+ (% in CD8+ T cells)
CD22+ TVM
Cell # (×10^6)
PBS
IL-4c
H. poly.
F
mesLN
CD22+ (% in CD8+ T cells)
Cell # (×10^6)
ns
IL-4RαWT
IL-4RαΔCD8
G
PBS
IL-4c
H. polygyrus
IL-4RαΔCD8 TVM
CD22 (PE)
CD124 (BV421)
4.09
2.31
61.7
31.9
2.81
25.2
39.6
32.4
2.68
15.2
42.8
39.3
H
Spleen
mesLN
WT
CD124−
CD22+ (% in CD8+ T cells)
PBS
IL-4c
H.polygyrus
IL-4RαWT
IL-4RαΔCD8
I
BALB/c
C57BL/6
CD22+ (% in TVM)
WT
Il4ra−/−
Stat6−/−
J
Thy1.2+ lymphocytes
CD45.1(APC)
CD45.2 (BV510)
49.0
WT
Il4ra−/−
47.7
TVM (% in CD8+ T cells)
CD22+ (% in CD8+ T cells)
CD45.1 (WT)
CD45.2 (Il4ra−/−)

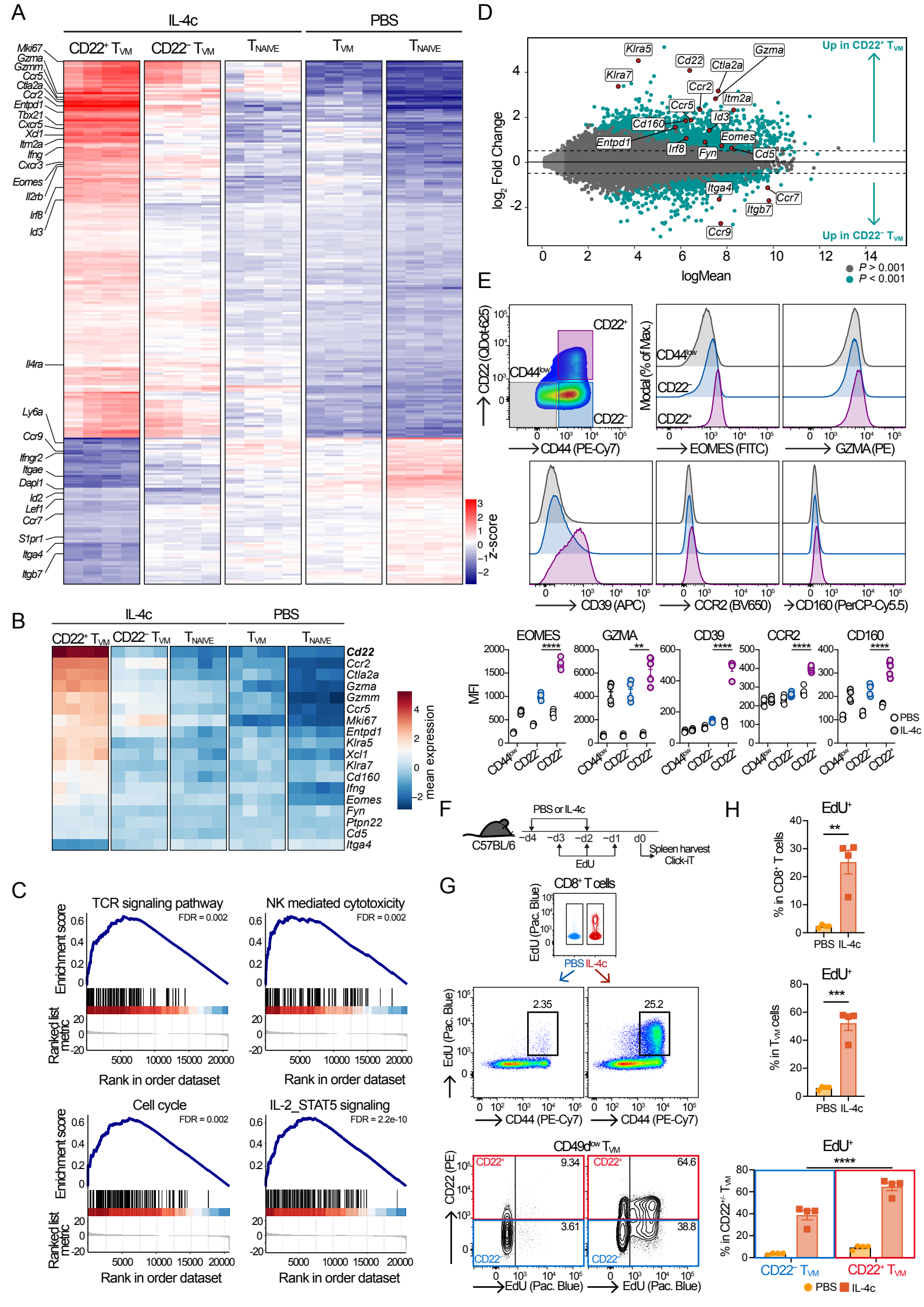
A
IL-4c
PBS
CD22+ TVM
CD22− TVM
TNAIVE
TVM
TNAIVE
Mki67
Gzma
Gzmm
Ccr5
Ctla2a
Ccr2
Entpd1
Tbx21
Cxcr5
Xcl1
Itm2a
Ifng
Cxcr3
Eomes
Il2rb
Irf8
Id3
Il4ra
Ly6a
Ccr9
Ifngr2
Itgae
Dapl1
Id2
Lef1
Ccr7
S1pr1
Itga4
Itgb7
z-score
B
IL-4c
PBS
CD22+ TVM
CD22− TVM
TNAIVE
TVM
TNAIVE
Cd22
Ccr2
Ctla2a
Gzma
Gzmm
Ccr5
Mki67
Entpd1
Klra5
Xcl1
Klra7
Cd160
Ifng
Eomes
Fyn
Ptpn22
Cd5
Itga4
mean expression
C
TCR signaling pathway
FDR = 0.002
NK mediated cytotoxicity
FDR = 0.002
Cell cycle
FDR = 0.002
IL-2_STAT5 signaling
FDR = 2.2e-10
Enrichment score
Ranked list metric
Rank in order dataset
D
Klra5
Cd22
Gzma
Klra7
Ctla2a
Ccr2
Itm2a
Ccr5
Id3
Cd160
Entpd1
Irf8
Fyn
Eomes
Cd5
Itga4
Ccr7
Itgb7
Ccr9
Up in CD22+ TVM
Up in CD22− TVM
log2 Fold Change
logMean
P > 0.001
P < 0.001
E
CD22 (QDot-625)
CD22+
CD44low
CD22−
CD44 (PE-Cy7)
Modal (% of Max.)
CD44low
CD22−
CD22+
EOMES (FITC)
GZMA (PE)
CD39 (APC)
CCR2 (BV650)
CD160 (PerCP-Cy5.5)
EOMES
GZMA
CD39
CCR2
CD160
MFI
PBS
IL-4c
CD44low
CD22−
CD22+
F
C57BL/6
PBS or IL-4c
−d4
−d3
−d2
−d1
d0
EdU
Spleen harvest
Click-iT
G
CD8+ T cells
EdU (Pac. Blue)
PBS
IL-4c
2.35
25.2
CD44 (PE-Cy7)
CD49dlow TVM
CD22 (PE)
CD22+
9.34
64.6
3.61
38.8
CD22−
EdU (Pac. Blue)
H
EdU+
% in CD8+ T cells
PBS
IL-4c
EdU+
% in TVM cells
PBS
IL-4c
EdU+
% in CD22+/− TVM
CD22− TVM
CD22+ TVM
PBS
IL-4c

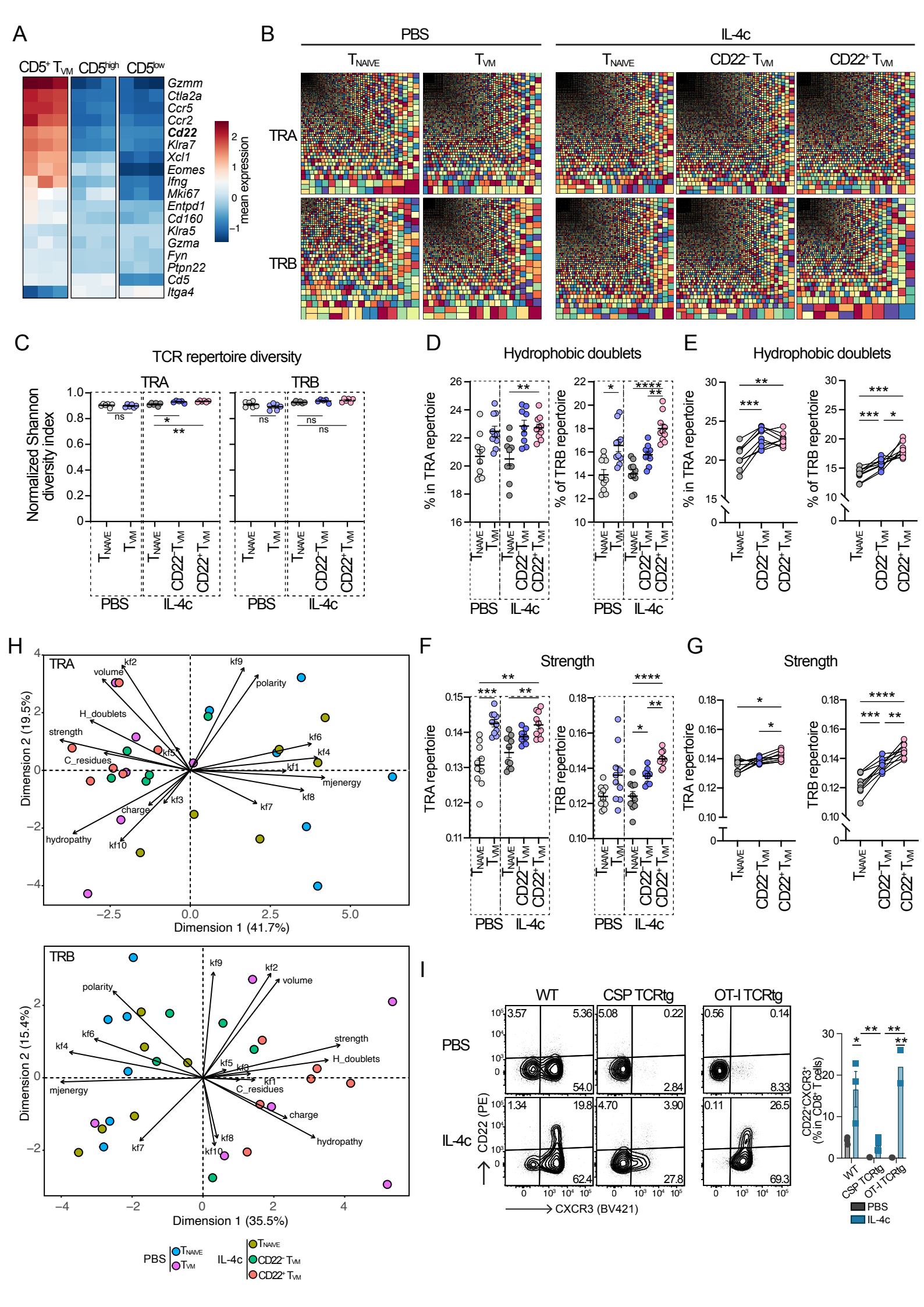
A
CD5+ TVM
CD5high
CD5low
Gzmm
Ctla2a
Ccr5
Ccr2
Cd22
Klra7
Xcl1
Eomes
Ifng
Mki67
Entpd1
Cd160
Klra5
Gzma
Fyn
Ptpn22
Cd5
Itga4
mean expression
B
PBS
IL-4c
TNAIVE
TVM
CD22- TVM
CD22+ TVM
TRA
TRB
C
TCR repertoire diversity
TRA
TRB
Normalized Shannon diversity index
ns
D
Hydrophobic doublets
% in TRA repertoire
% of TRB repertoire
E
Hydrophobic doublets
F
Strength
TRA repertoire
TRB repertoire
G
Strength
H
TRA
volume
kf2
kf9
polarity
H_doublets
strength
kf6
kf4
C_residues
kf5
kf1
mjenergy
kf8
kf3
charge
kf7
hydropathy
kf10
Dimension 1 (41.7%)
Dimension 2 (19.5%)
TRB
Dimension 1 (35.5%)
Dimension 2 (15.4%)
I
WT
CSP TCRtg
OT-I TCRtg
PBS
IL-4c
CD22 (PE)
CXCR3 (BV421)
CD22+CXCR3+ (% in CD8+ T cells)

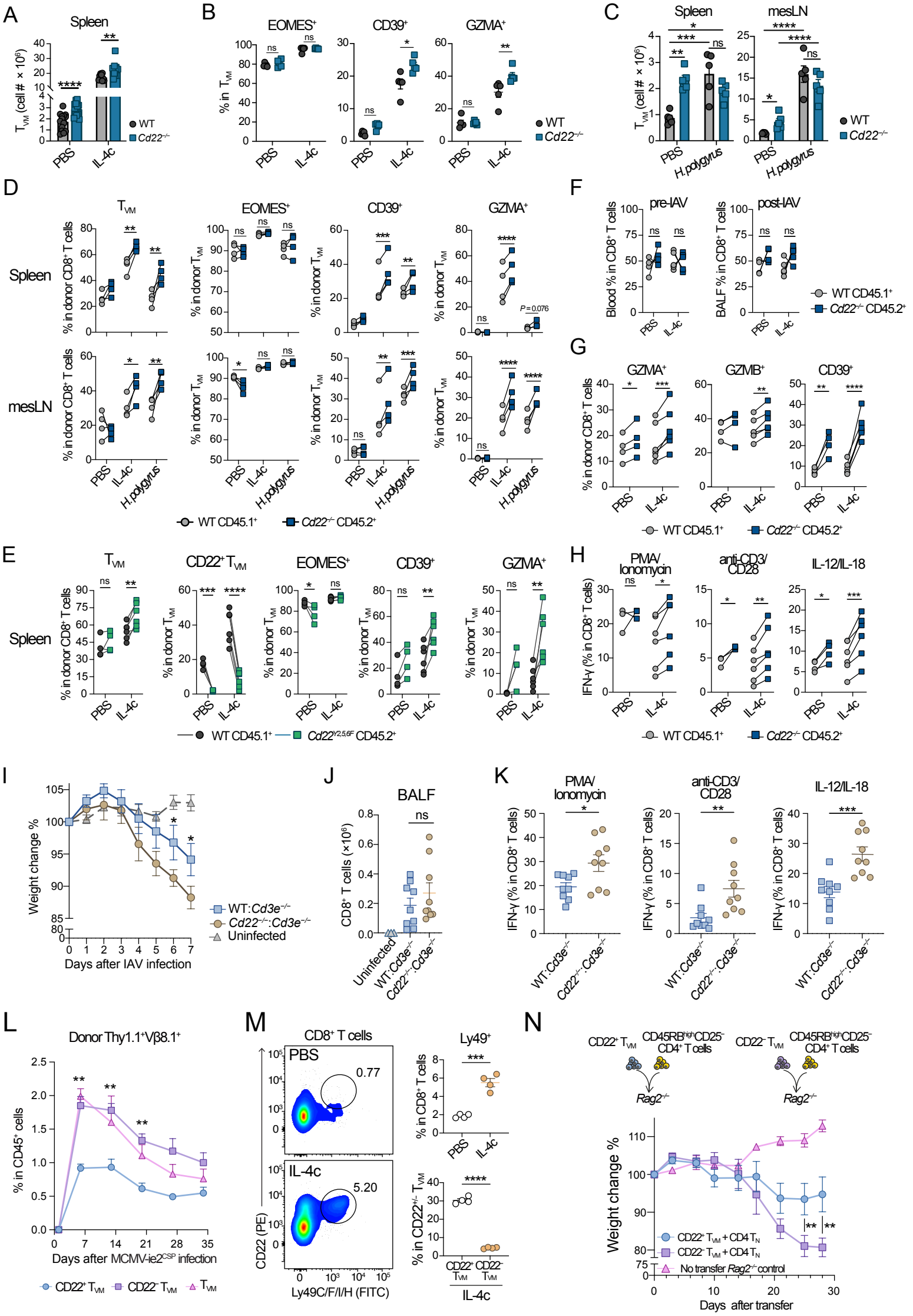
A
Spleen
B
EOMES+
CD39+
GZMA+
C
Spleen
mesLN
D
TVM
Spleen
mesLN
F
pre-IAV
post-IAV
G
GZMA+
GZMB+
CD39+
E
TVM
CD22+ TVM
EOMES+
CD39+
GZMA+
H
PMA/ Ionomycin
anti-CD3/ CD28
IL-12/IL-18
I
Weight change %
Days after IAV infection
J
BALF
K
PMA/ Ionomycin
anti-CD3/ CD28
IL-12/IL-18
L
Donor Thy1.1+Vβ8.1+
Days after MCMV-ie2CSP infection
M
CD8+ T cells
PBS
IL-4c
Ly49+
N
Weight change %
Days after transfer

Supplementary material

Materials and Methods

Mice

Female BALB/cAnNCrl and C57BL/6NCrl wild-type mice, 6–8 weeks old, were purchased from Charles River. *E8i*^{Cre} genitor mice were obtained from Prof. A. Thiel (C57BL/6-Tg(Cd8a-cre)1Itan/J, Charité Berlin, Germany). BALB/c CD45.1^{+} genitor mice were generously provided by Prof. U. Eriksson (Center for Molecular Cardiology, University of Zurich). CSPTg TCR transgenic Thy1.1 BALB/c mice were obtained from Prof. F. Zavala (Johns Hopkins University, USA) and Dr R. Amino (Institut Pasteur Paris, France). *Rag2*$^{-/-}$ (C57BL/6NRj-*Rag2*^{tm1Ciphe}*/Rj*) mice were obtained from Janvier Labs. OT-I TCR transgenic *Rag2*$^{-/-}$ and *Cd3e*$^{-/-}$ mice were obtained from Prof. S. Goriely and F. Andris (Université Libre de Bruxelles, Belgium). Thy1.2.1 (Thy1.1^{+}Thy1.2^{+}) BALB/c mice were obtained by crossing Thy1.1 BALB/c with WT BALB/c. *Il4ra*$^{-/-}$ BALB/c and *Il4ra*$^{lox/lox}$ BALB/c mice were initially obtained from Prof. F. Brombacher (University of Cape Town, South Africa). CD45.1.2 (CD45.1^{+}CD45.2^{+}) C57BL/6 mice were obtained by crossing CD45.1 with CD45.2 C57BL/6 mice. *Cd22*$^{-/-}$ (C57BL/6-*Cd22*^{tm1Lam} /J) mice and *Cd22*^{Y2,5,6F} knockin bone-marrow were obtained from colonies in Erlangen, Germany. Female BALB:B mice (C.B10-*H2*^{b}/LilMcdJ), that are BALB/c congenic for the C57BL/10-derived H-2^{b} region, were obtained from Dr O. Denis (Sciensano, Belgium). GREAT IFN-γ reporter mice (B6.129S4-*Ifng*$^{tm3.1Lky}$/J) have an IRES-eYFP reporter cassette inserted between the translational stop codon and 3' UTR/polyA tail of the *Ifng* gene and were obtained from Jax laboratories. *Ifnar1*$^{-/-}$ C57BL/6 mice were obtained from Kai Dallmeier (Rega Institute, KULeuven). WT C57BL/6 and *Stat6*$^{-/-}$ mice obtained from The Jackson Laboratory and germ-free obtained from the McGill Centre for Microbiome Research were handled with accordance with the McGill University Health Centre Research Institute Animal Resource Division with approved animal use permit no. 7977.

Parasites

S. mansoni-exposed Swiss-Webster mice were provided by the Schistosome Research Reagent Resource Center for distribution by BEI Resources, NIAID, NIH: *Schistosoma mansoni*, Strain NMRI exposed *Biomphalaria glabrata*, Strain NMRI (NR-21962), *S. mansoni*, Strain NMRI exposed Swiss-Webster mice (NR-21963). *S. mansoni* cercariae were collected from *S. mansoni* exposed *B. glabrata* and used for natural infection. *S. mansoni* eggs used for egg immunization, were collected from *S. mansoni*-exposed Swiss-Webster mouse liver and stored in PBS at −80 °C, as previously described with minor modifications (*6*). Treatment with *S. mansoni* eggs consisted of an intraperitoneal immunization on day 0 (5000 eggs per mouse) followed by one intravenous injection of 5000 eggs on day 14.

Viruses

The strain MHV-68 of Murid gammaherpesvirus-4 (MuHV-4) expressing luciferase under the control of the M3 promoter (MuHV-4-Luc) was propagated, semi-purified and titrated in BHK-21 cells, as described (*6*). The mouse cytomegalovirus (MCMV) BAC clone pSM3r 3.3 was used to insert the H-2Kb-restricted CSP peptide (SYVPSAEQI) from *Plasmodium yoelli* in frame of MCMV immediate early 2 (ie2) coding sequence using galK recombineering (*6*, *70*). The generated MCMV-ie2-CSP strain was propagated in M2-10B4 cells. The pSM3r 3.3 clone and M2-10N4 cells were generously provided by Prof. L. CiCin-Sain (Helmholtz Centre for Infection Research, Germany). Influenza H1N1 strain A/Puerto Rico/8/34 (PR8) was propagated and isolated from Madin–Darby canine kidney (MDCK) cells and titrated with standard plaque assay in MDCK cells. In brief, MDCK cells were cultivated in Dulbecco's modified Eagle's medium (DMEM; ThermoFisher Scientific), supplemented with 2 mM glutamine, 100 U penicillin, 100 mg streptomycin, and 5% heat-inactivated fetal calf serum (FCS) at 37°C in an atmosphere of 5% CO_2. For PR8 growth, TPCK (L-1-tosylamido-2-phenylethyl chloromethyl ketone)-treated trypsin (2 mg/mL) was added to culture medium. Mice were infected intratracheally (i.t.) under gas anesthesia (isoflurane) with 50 µL sterile PBS containing 10^4 PFU of MuHV-4 or 25 PFU of IAV. Luminescence signals after MuHV-4-Luc infection were measured after D-luciferin intraperitoneal injection (150 mg/kg) using an IVIS Spectrum system (Revvity).

Antibodies and flow cytometry.
The full list of antibodies is available in Table S1. Various panels for surface stainings were used including antibodies to CD3ε (145-2C11, 0.4 µg mL^{-1}, APC-Cy7, Armenian Hamster IgG1, κ), CD183 (CXCR3-173, 2 µg mL^{-1}, BV421 or PE, Armenian Hamster IgG1, κ), CD8α (53-6.7, 1 µg mL^{-1}, BUV615, Rat IgG2a, κ), CD49d (R1-2, 1 µg mL^{-1}, BV650 or BV786, CDF IgG2b, κ), CD124 (mIL4R-M1, 1 µg mL^{-1}, PE or BV421, Lewis IgG2a, κ), CD195 (C34-3448, 2 µg mL^{-1}, BV711, Rat IgG2c, κ), CD62L (MEL-14, 1 µg mL^{-1}, FITC or BV785, CDF IgG2a, κ), CD4 (GK1.5, 2 µg mL^{-1}, BUV395, Rat IgG2b, κ), CD44 (IM7, 0.4 µg mL^{-1}, BV786, Rat IgG2b, κ) all from BD Biosciences, antibody to CD3ε (145-2C11 or 17A2, 0.4 µg mL^{-1}, V450 or APC, Armenian Hamster IgG or Rat IgG2b, κ), KLRG1 (2F1, BV786, Syrian Hamster IgG2, κ), TCRβ chain (H57-597, 0.8 µg mL^{-1}, BV711, Armenian Hamster IgG), CD8α (53-6.7, 1 µg mL^{-1}, FITC or APC or BV785 or APC/Fire 750 or BV605, Rat IgG2a, κ), CD44 (IM7, 0.4 µg mL^{-1}, PE-Cy7, Rat IgG2b, κ), CD183 (CXCR3-173, 2 µg mL^{-1}, FITC or APC, Armenian Hamster IgG), CD124 (I015F8, 1 µg mL^{-1}, APC, Lewis IgG2a, κ), CD39 (Duha59, 2 µg mL^{-1}, APC or PE-Cy7, Rat IgG2a, κ), CD4 (GK1.5, 0.4 µg mL^{-1}, FITC or APC, Rat IgG2b, κ), CD24 (M1/69, 2 µg mL^{-1}, APC/Fire 750, Rat IgG2b, κ), CD45.1 (A20, 2 µg mL^{-1}, BV421 or APC-Cy7 or APC or Alexa Fluor 700, Mouse (A.SW) IgG2a, κ), CD45.2 (104, 1 µg mL^{-1}, BV510 or PE-Cy7 or Alexa Fluor 700, Mouse (SJL) IgG2a, κ), CD90.1 (OX-7, 2,5 µg mL^{-1}, APC or Alexa Fluor 700, Mouse IgG1, κ), CD90.2 (53-2.1, 1 µg mL^{-1}, BV421, Rat IgG2a, κ), CD122 (TM-β1, APC-Cy7, 1 µg mL^{-1}, Rat IgG2b, κ), CD192 (SA203G11, 2 µg mL^{-1}, BV650, Rat IgG2b, κ), CD160 (7H1, 2 µg mL^{-1}, PerCP-Cy5.5, Rat IgG2a, κ), TCR Vβ8.1, 8.2 (MR5-2, 2 µg mL^{-1}, PE, Mouse IgG2a, κ), Ly-49C/F/I/H (14B11, 2 µg mL^{-1}, FITC, Syrian Hamster IgG), CD45RB (C363-16A, 2 µg mL^{-1}, APC, Rat IgG2a, κ), CD25 (PC61, 2 µg mL^{-1}, FITC, Rat IgG1, λ) from BioLegend, CD45.2 (104, 2 µg mL^{-1}, eFluor450, Mouse IgG2a, κ), TCRβ chain (H57-597, 2 µg mL^{-1}, APC-eF780, Armenian Hamster IgG), CD49d (R1-2, 2 µg mL^{-1}, PerCP710 or PE, Rat IgG2b, κ), CD4 (RM4-5, 2 µg mL^{-1}, AF700, Rat IgG2a, κ), CD44 (IM7, 2 µg mL^{-1}, PE, Rat IgG2b, κ) from ThermoFisher and antibodies to CD22 (Cy34.1, 3 µg ml^{-1}, PE or biotinylated, isotype mouse IgG1κ) from Miltenyi Biotec. Biotinylated antibodies were detected using Qdot 625-conjugated streptavidin (5 nM, ThermoFisher). Dead cells were stained using Zombie Aqua Fixable Viability Kit (1000x dilution, Biolegend) or Fixable Viability Dye (1000× dilution, eFluor780 or eFluor 506, eBioscience). Antibiodies against cytoplasmic proteins: IFN-γ (XMG1.2, BV711 (2 µg mL^{-1}, Biolegend) or PE (2 µg mL^{-1}, Biolegend), or Alexa Fluor 488 (5 µg mL^{-1}, ThermoFisher) or APC (2 µg mL^{-1}, ThermoFisher), Rat IgG1, κ), GZMA (3G8.5, 2 µg mL^{-1}, PE (BioLegend) or APC ThermoFisher, Mouse IgG2b, κ), or GZMB (QA16102, 2 µg mL^{-1}, PE, Mouse IgG1 κ, BioLegend), or IL-4 (11B11, APC, Rat IgG1 κ, 2 µg mL^{-1}, ThermoFisher), or IL-5 (TRFK5, BV421, Rat IgG1 κ, 2 µg mL^{-1}, Biolegend), or IL-13 (eBio13A, Alexa Fluor 488, Rat IgG1 κ, 2 µg mL^{-1}, ThermoFisher). Antibody against nuclear proteins: EOMES (Dan11mag, 2 µg mL^{-1}, PE or PE-eFluor610, Rat IgG2a, κ, eBioscience, or X4-83, 2 µg mL^{-1}, Alexa Fluor 488, Mouse IgG1, κ, BD Biosciences) or GATA3 (TWAJ, 5 µL per test, Alexa Fluor 488 or PerCP-710, Rat IgG2b, κ, ThermoFisher). For tetramer stainings, cells were incubated with BV421-conjugated tetramers H-$2D^b$-$ORF6^{487-495}$ (AGPHNDMEI, 90 nM) or H-$2K^b$-$ORF61^{521-531}$ (TSINFVKI, 45 nM) (NIH Tetramer Core Facility) for 30min at RT before further staining.

***Ex vivo* restimulation and cytokine production**
Cytokine production upon restimulation was assessed by intracellular cytokine staining (ICCS) and flow cytometry. For ICCS, cells were cultured at 37°C, 5% CO_2 in IMDM complemented with 2 mM β-mercaptoethanol, 100 U mL^{-1} penicillin, 100 mg mL^{-1} streptomycin and 10% fetal calf serum for 4h in presence of brefeldin A (10 µg mL^{-1}, Sigma-Adlrich), monensin (2 µM, eBioscience). Unbiased restimulation was performed using phorbol 12-myristate 13-acetate (PMA, 20 ng mL^{-1}, Sigma-Adlrich) and ionomycin (1 µg mL^{-1}, Sigma-Aldrich). Innate restimulation was performed using IL-12 (5 ng mL^{-1}, BioLegend) and IL-18 (10 ng mL^{-1}, BioLegend) for 16h and brefeldin A was added for the last 3h of incubation. In some experiments, anti-CD107a (1D4B, 0.5 µg mL^{-1}, PerCP-Cy5.5, Rat IgG2a, κ) was added to the stimulation media. TCR-specific restimulation was done using anti-CD3 (145-2C11, 1 µg mL^{-1}, purified, BioLegend) and anti-CD28 (37.51, 1 µg mL^{-1}, purified, BioLegend) mixed with

brefeldin A and monensin for 4h. Following surface and viability stainings, cells were fixed in 2% paraformaldehyde overnight and washed with Permeabilization Buffer (eBioscience) before being incubated with antibodies against IFN-γ (clone XMG1.2, 2 μg mL^{-1}, BV711 or PE, Rat IgG1, κ, BioLegend) in Permeabilization Buffer for 20 min at 4°C.

Genotyping of *Il4ra* locus in peripheral $CD8^+$ T cells

$CD124^+$ or $CD124^-$ $CD8^+$ T cells of IL-4R$\alpha^{\Delta CD8}$ mice were FACS-sorted from spleens before DNA extraction using the QIAamp DNA mini kit (Qiagen). Then, 100 ng of DNA was subjected to genotyping PCRs. Standard mutiplex genotyping PCR was performed using the following primers to amplify the WT allele (Exon 7 Forward 1 – 5'-TGACCTACAAGGAACCCAGGC-3' and Exon 8 Reverse – 5'-CTCGGCGCACTGACC CATCT-3' primer) and the IL-4Ra KO allele (P1 – 5'-GGCTGCTGACCTGGAATAACC-3' and P2 – 5'-CCTTTGAGAACTGCGGGCT -3'), generating bands of 600 or 471 nt, respectively. Quantitative PCR was performed using iQ SYBR Green Supermix (Biorad) in a CFX96 Touch Real-Time PCR Detection System (Biorad). Knockout *Il4ra* alleles were amplified using primers intron6-2 Forward primer (5'-CCCTTCCTGGCCCTGAATTT-3') and P2 primer to generate an amplicon of 230 nt. Mouse β-actin genomic sequence was amplified using primers (5'-GGCTGTATTCCCCTCCATCG-3' and 5'-CCAGTTGGTAACAATGCCATGT-3').

Single-cell RNA-seq analysis

Raw data processing. For 10x Genomics platform, the sequencing run was processed using Cell Ranger (v3.0.2). For BD Rhapsody platform, sequencing run was processed using SevenBridges Genomics. First using mkfastq function to produce fastq files and then the count function to perform alignment, filtering, barcode counting, and UMI counting. The merged data were transferred to the R statistical environment for analysis using the package Seurat (v3.1.5) (*71*). *Doublet cell filtering.* Cell Hashing/HTO libraries were processed using CITE-seq Count python package v1.4.3 (https://github.com/Hoohm/CITE-seq-Count) and used in Seurat to remove identified Doublet cells. Sample Tag demultiplexing for BD Rhapsody platform was performed using the build-in function in SevenBridges Genomics. *Data cleaning.* We additionally applied two filtering steps as we selected cells with a total number of molecules detected within a range between 2000 and 10,000 and a percentage of reads that map to the mitochondrial genome lower than 10%. Doublets and contaminating non-$CD8^+$ T cells were excluded (exclusion of cells expressing *Cd19, Cd4, Ncr1, Itgax, Tcrg-C1, Tcrg-C3, Tcrg-C4, Trdc*) and a total of 33,553 cells were analysed in which ∼30-50,000 reads and ∼2,000 genes per cell were detected. Six datasets were obtained based on the treatment (PBS, IL-4c and *H. polygyrus*) and genotype (IL-4R$\alpha^{\Delta CD8}$ and littermate WT control). *Samples integration & Transcriptome-based clustering.* We used Seurat SCTransform workflow for Multiple Dataset Integration in order to merge all the datasets and proceed with joint analysis. We used FindIntegrationAnchors and IntegrateData functions based on SCT normalization. We then performed PC analysis with RunPCA algorithm producing 50 PCs and we applied FindNeighbors and FindClusters functions from Seurat with two chosen parameters (dims = 1:50; resolution = 0.5) to identify clusters. *Data visualization.* Data were then dimensionally reduced for visualization using RunUMAP function and using (dims = 1:50). UMAP figures were obtained using DimPlot function with UMAP reduction. Other plot types were generated using implemented Seurat functions, custom R scripts or combinations of both. *SingleR for cluster annotation and selection.* SingleR package was performed for unbiased annotation and was performed against the build-in ImmGen database in SingleR package. Clusters showing expression of CD8a and CD3e were selected, and other clusters were removed. Cells presenting T8.memory or T8.effector profiles were selected for additional analysis. New clustering of this subset of cells was performed using same methodology as previously described. *Single-cell differential gene expression analysis.* Cluster specific markers were obtained by the FindAllMarkers function of Seurat with default parameters. Pairwise single-cell differential gene expression analysis was performed between condition inside clusters using the FindMarkers function with default parameters. *Gene set enrichment analysis*. TF-gene interactions were extracted from mouse DoRothEA database (*72*), while filtering for high-confidence interactions (score A, B, or C). TF activities were then inferred from differential gene expression results using fgsea (*73*),

with signed logarithm of p-value used as the metric to rank the genes. Method details are available here https://github.com/BlanQwall/VM_T.

RNA sequencing

Libraries were quality checked on an Agilent Bioanalyzer, pooled at an equimolar ratio and sequenced on a Novaseq S4 V1.5 with 300 cycles XP workfow. Reads were mapped to the mouse reference genome (mm10) using STAR (version 3.4.0). Subsequently the analysis was performed with R Bioconductor packages Rsamtools (version 1.18.3) and GenomicAlignments (version 1.2.2) were used to count the reads by exons, and gene count datasets were then analyzed to determine DE genes (DEGs) using DESeq2 (version 1.16.1). A gene was determined to be a DEG by passing FDR < 0.01 and log 2-fold change ≥ ±1.

CDR3 sequence analysis

CDR3 sequences were extracted from raw sequencing fastq files after aligning the reads to reference V, D and J genes from 'TRA' or 'TRB' loci of GenBank database using the MiXCR software (version 3.0.12) (*74*). CDR3 sequences were further analyzed using VDJtools software version 1.2.1 (*75*). CDR3 extraction was also performed on raw fastq files derived from RNA-seq experiments to increase the robustness of the data in all analyzed groups, this analysis was performed following the standard pipeline for CDR3 extraction from RNA-seq data described in MiXCR documentation. In all cases out of frame sequences were excluded from the analysis, as well as non-functional TRA and TRB segments using IMGT (the international ImMunoGeneTics information system®) annotation. Cumulative gene segment plots were generated using the output from CalcSegmentUsage function. Tree maps were generated using the Treemap Package (version 2.4.3) on RStudio. Diversity read-outs (Normalized Shannon-Wiener, Inverse Simpson, Chao1 and efronThisted indexes) were obtained from the re-sampled file generated using CalcDiversityStats function. Cysteine usage was determined following previously described indications (*76*). Hydrophobic doublets in CDR3α and CDR3β sequences were determined by calculating the percentage of sequences using any of the 175 amino acid doublets previously identified as promoters of self-reactivity (*47*). Physicochemical properties were computed on the 5 central amino acids from the CDR3 sequences using CalcCdrAaStats function from VDJtools software. Principal component analysis of CDR3α and CDR3β repertoire was performed using R package FactoMineR (version 2.7) and using the variables described in Fig. S8i which were scaled to similar range using Z-score normalization prior to PCA analysis. PCA results were visualized using factoextra (version 1.0.7) R package.

Figure S1. Characterization of IL-4Rα$^{\Delta CD8}$ mice.

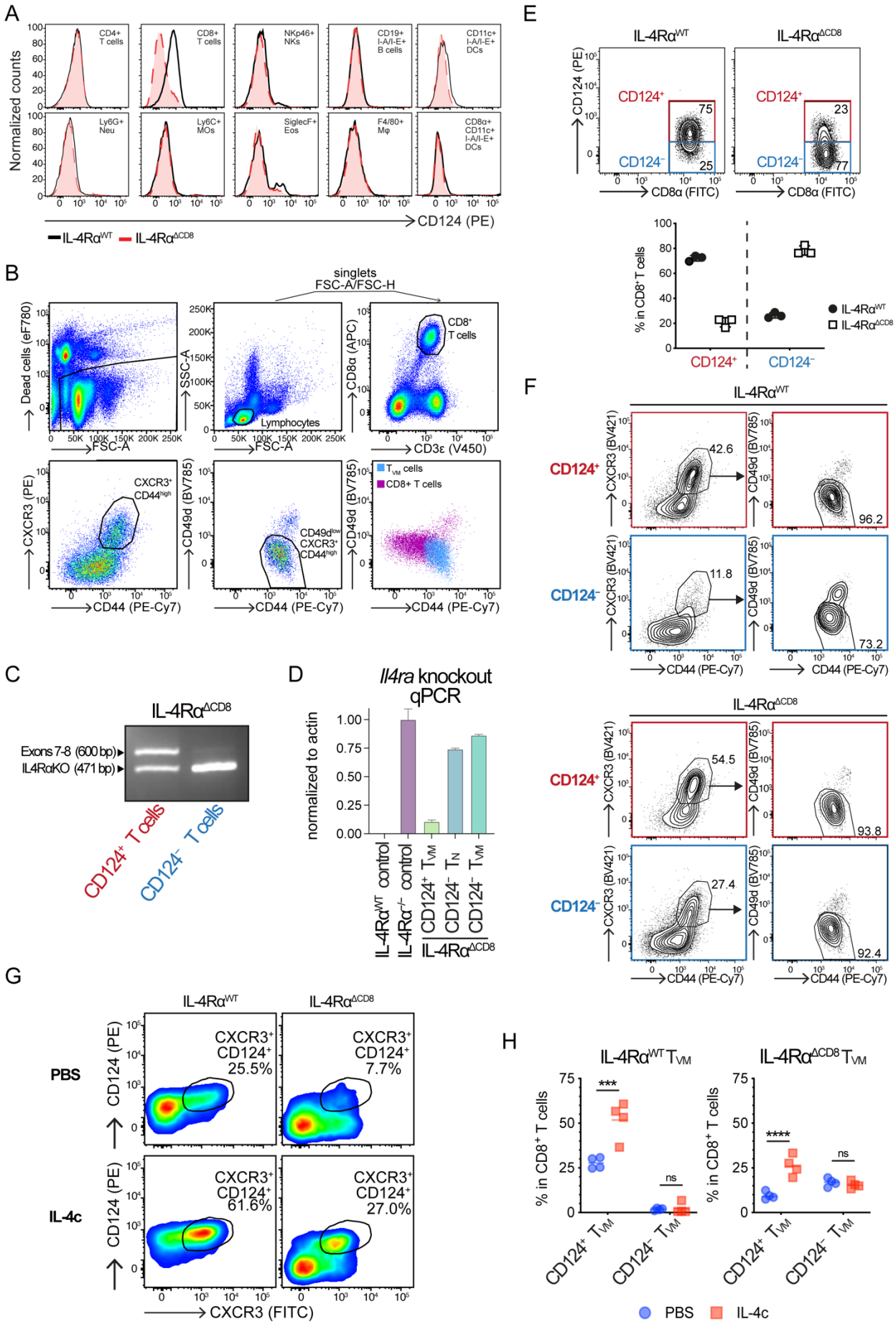

Figure S1. Characterization of IL-4Rα$^{\Delta CD8}$ mice.
(**A**) Representative histograms of CD124 expression in the indicated population from the spleen of IL-4Rα^{WT} or IL-4Rα$^{\Delta CD8}$ naive mice.
(**B**) Gating strategy for CD49d^{low}CXCR3^{+} T_{VM} detection. Singlets were selected on FSC-A/FSC-H.
(**C**) Genotyping PCR on DNA extracted from FACS-sorted CD124^{+} or CD124^{-} CD8 T cells of IL-4Rα$^{\Delta CD8}$ mice to amplify *Il4ra* wild-type (Exons 7-8) or knockout allele (IL-4RαKO), respectively.
(**D**) Quantitative PCR revealing *Il4ra* knockout allele. Data are presented as $2^{-\Delta Cq}$ normalized to actin.
(**E**) Representative contour flow plot of spleen CD8^{+} T lymphocytes. Numbers indicate percent of events in each gate. Percentages of CD124^{+} and CD124^{-} CD8^{+} T cells in IL-4Rα^{WT} and IL-4Rα$^{\Delta CD8}$ mice.
(**F**) Representative contour plots depicting the gating strategy of CD124^{+} and CD124^{-} CD49d^{low}CXCR3^{+} T_{VM} in the spleen of IL-4Rα^{WT} or IL-4Rα$^{\Delta CD8}$ mice.
(**G**) Representative pseudocolour flow plot of spleen CD8^{+} T lymphocytes of IL-4Rα^{WT} or IL-4Rα$^{\Delta CD8}$ mice following PBS or IL-4c treatment. Numbers indicate events percent in each gate.
(**H**) Summary data of CD124^{+} and CD124^{-} T_{VM} in the spleen of IL-4Rα^{WT} or IL-4Rα$^{\Delta CD8}$ mice, following PBS or IL-4c treatment.
Statistical significance calculated using two-way analysis of variance (ANOVA) and Tukey's multiple comparisons test. Data are representative of two independent experiments with 3-4 mice per group. Mean ± s.e.m., each symbol represents one individual mouse.

Figure S2. Single-cell RNA sequencing of spleen CD8$^+$ T cells upon IL-4 response.

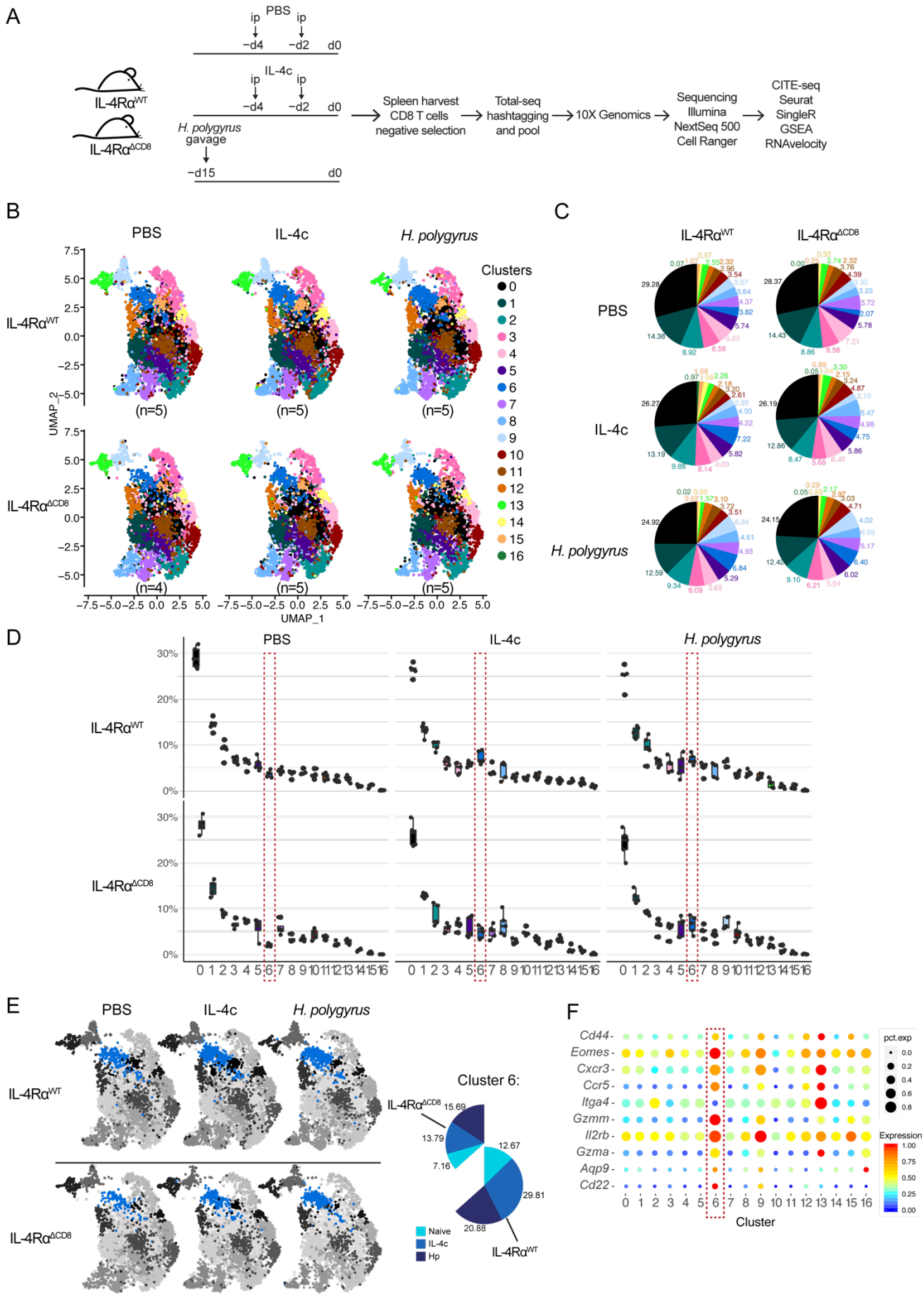

Figure S2. Single-cell RNA sequencing of spleen CD8$^+$ T cells upon IL-4 response.
(**A**) Experimental design of treatment with IL-4c or infection with *H. polygyrus* before CD8$^+$ T cell enrichment, hash-tagging, single cell capture, library preparation, and sequencing. The main packages used to analyze scRNA-seq data are listed.
(**B**) Split UMAP visualization of Seurat clustering analysis of combined single CD8$^+$ T cell transcriptomes of IL-4Rα^{WT} and IL-4Rα$^{\Delta CD8}$ mice, following treatment with PBS, IL-4c, or *H. polygyrus* infection. (n = 5, except IL-4Rα$^{\Delta CD8}$-PBS (n=4)).
(**C**) Pie charts of cell number proportions of each cluster in each dataset.
(**D**) Box plot distribution of the frequency of each cluster based on the hashtagging of each individual mouse sample included in each dataset.
(**E**) Split UMAP visualization of Seurat clustering analysis as in (b), highlighting cluster 6. The split pie chart shows the cell number proportion of cluster 6 in each dataset.
(**F**) Dot plot showing the average expression levels and percentage of expression of selected genes in each cluster obtained in Fig. 2a.

Figure S3. Single-cell RNA sequencing of spleen memory/effector CD8$^+$ T cells upon IL-4 response.

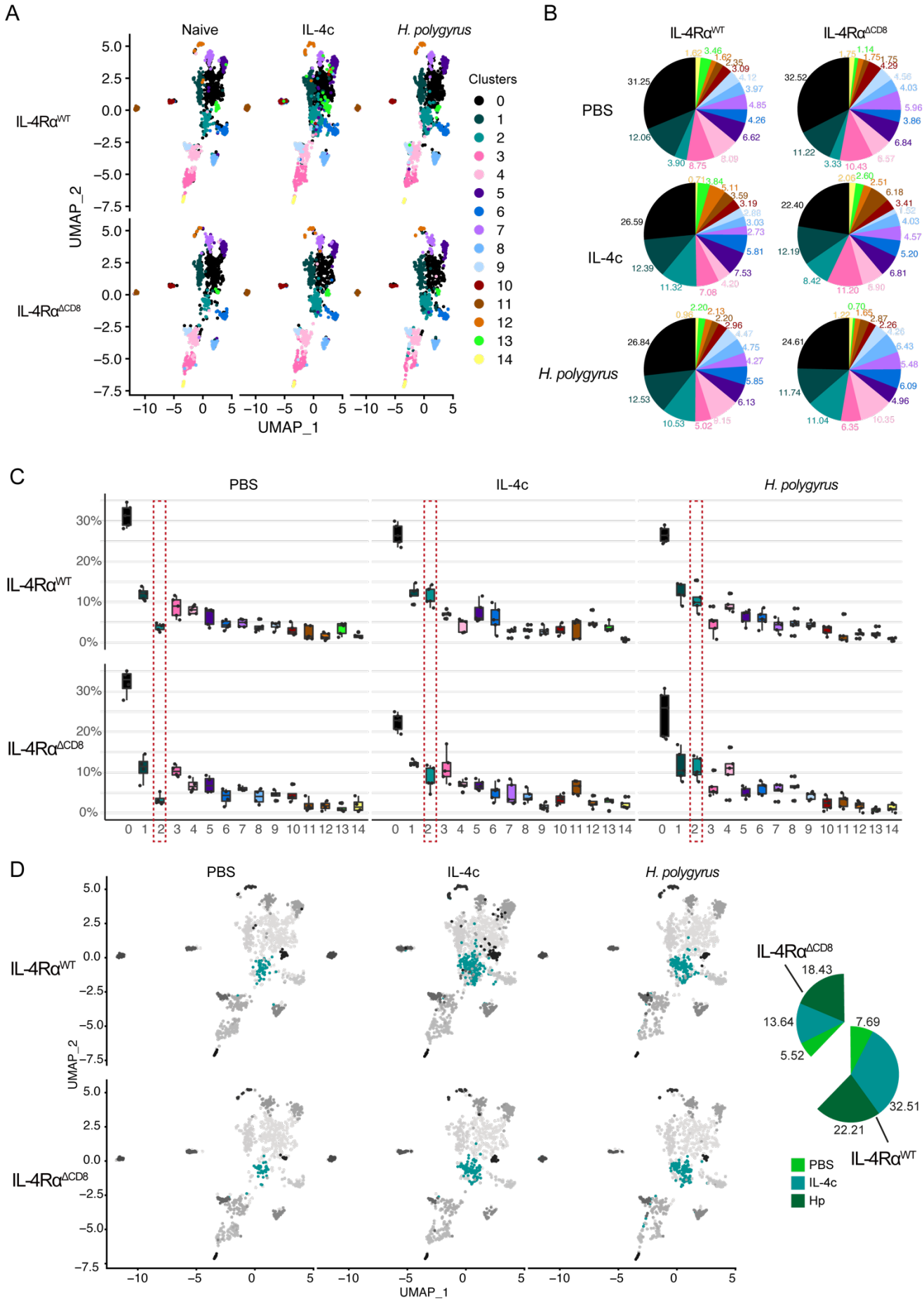

Figure S3. Single-cell RNA sequencing of spleen memory/effector CD8$^+$ T cells upon IL-4 response.
(**A**) Split UMAP visualization of Seurat clustering analysis of combined single memory/effector CD8$^+$ T cell transcriptomes of IL-4Rα^{WT} and IL-4Rα$^{\Delta CD8}$ mice as in Fig. 2d and following treatment with PBS, IL-4c, or *H. polygyrus* infection. (n = 5, except IL-4Rα$^{\Delta CD8}$-PBS (n=4)).
(**B**) Pie charts of cell number proportions of each cluster in each dataset.
(**C**) Box plot distribution of the frequency of each cluster based on the hashtagging of each individual mouse sample included in each dataset.
(**D**) Split UMAP visualization of Seurat clustering analysis as in (a), highlighting cluster 2. The split pie chart shows the cell number proportion of cluster 2 in each dataset.

Figure S4. Transcription regulation of memory/effector CD8$^+$ T cells upon IL-4 and *H. polygyrus* infection

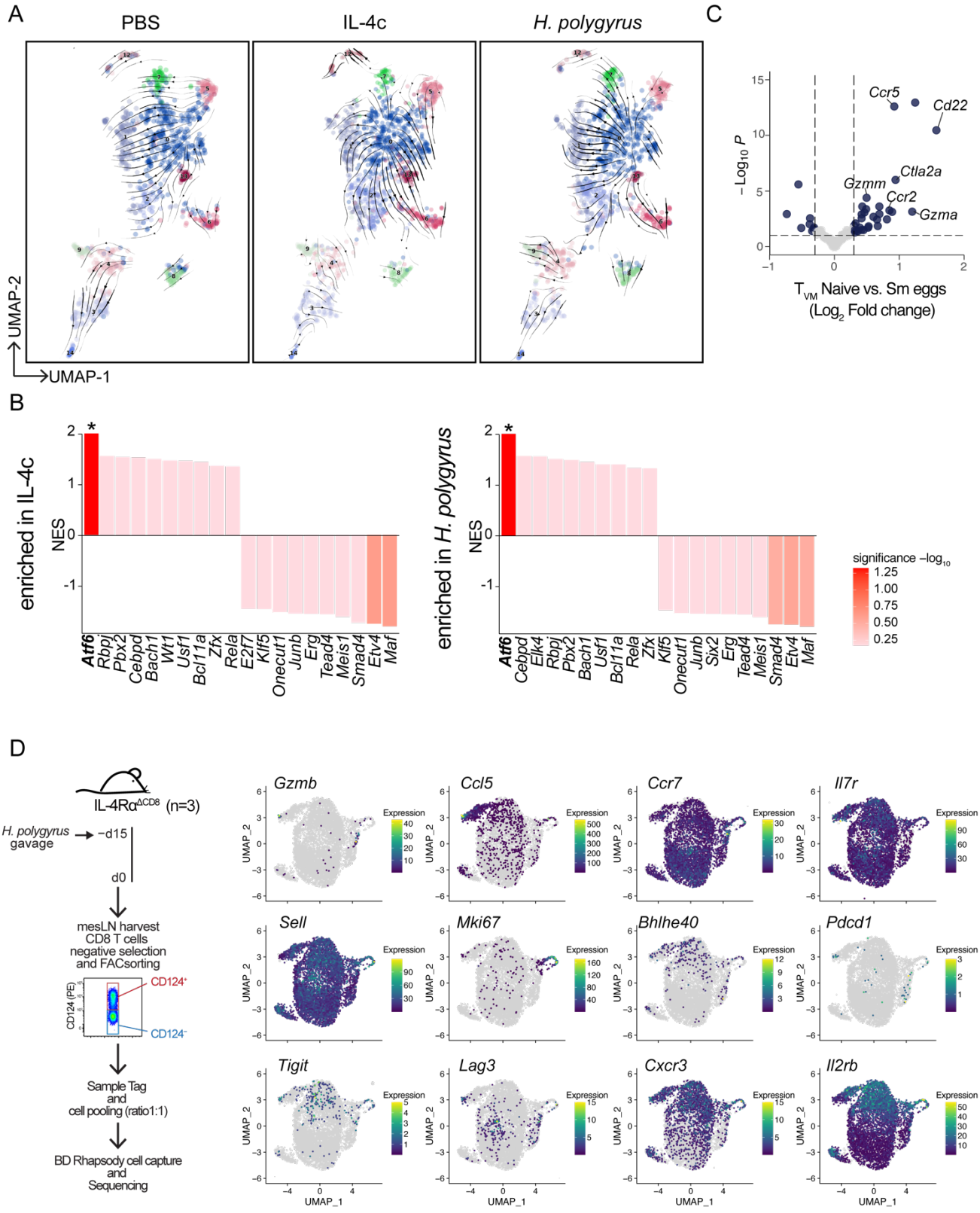

Figure S4. Transcription regulation of memory/effector CD8$^+$ T cells upon IL-4 and *H. polygyrus* infection

(**A**) Split UMAP visualization of RNAVelocity trajectory analysis of memory/effector CD8$^+$ T cell transcriptomes of IL-4Rα^{WT} mice.

(**B**) GSEA of the indicated transcription factor in the T_{VM} cluster 2. Top 10 gene set enrichment scores (NES) in scRNA-seq as in Fig. 2.

(**C**) Volcano plot of differentially expressed (DE) genes (P<0.1) showing DE genes in blue from bulk RNAseq data of sorted T_{VM} from PBS- or Sm-treated BALB/c WT mice, obtained in a previously published study(*6*).

(**D**) Experimental design before CD8$^+$ T cell enrichment, FACS-sorting and sequencing. UMAP visualizations show FeaturePlots of selected gene expression in single CD8$^+$ T cells from the mesLN of IL-4Rα$^{\Delta CD8}$ mice at day 15 after *H. polygyrus* infection, based on Fig. 3F.

Figure S5. Dynamics of CD22 expression in IL-4-induced T_{VM} during helminth infection.

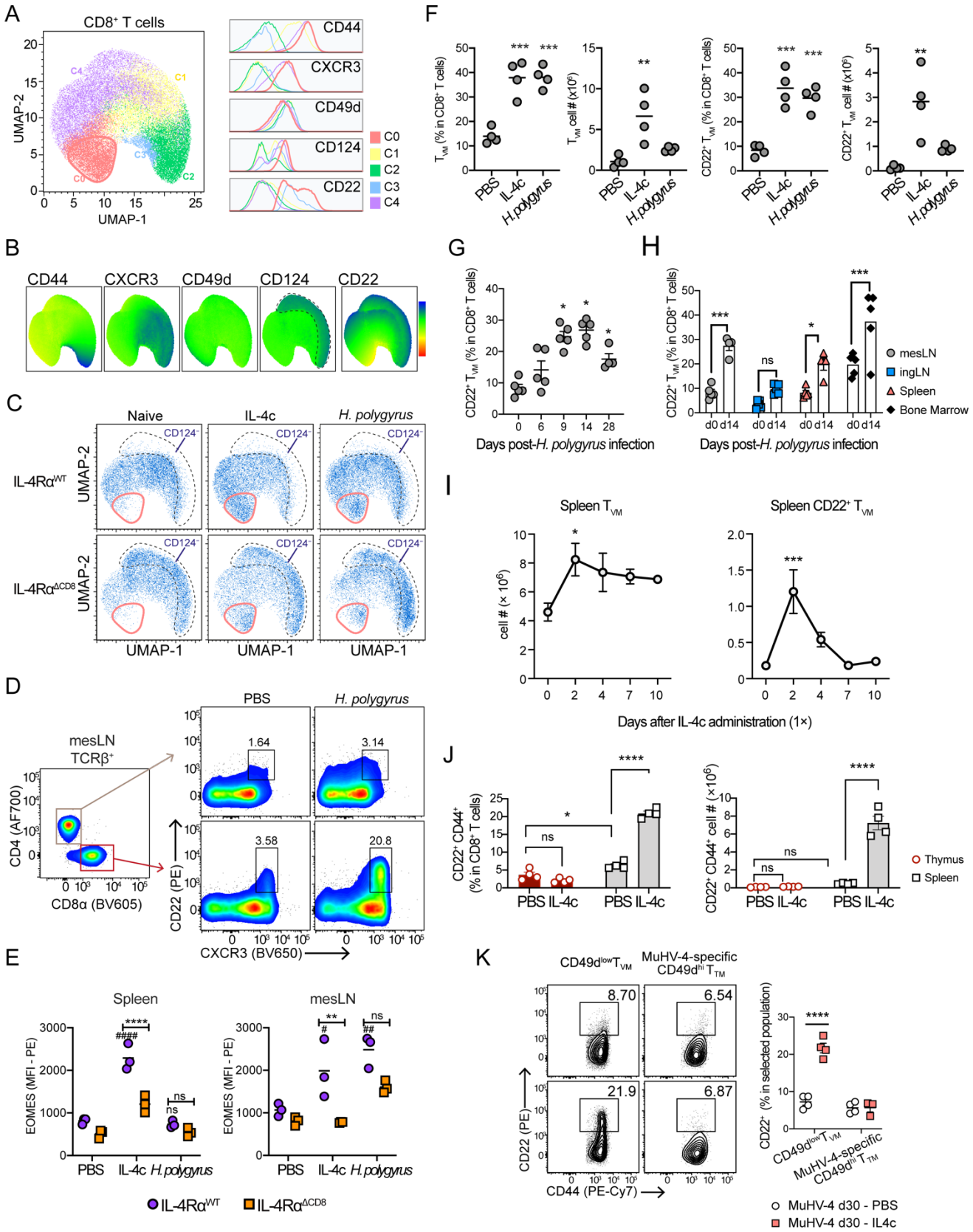

Figure S5. Dynamics of CD22 expression in IL-4-induced T_{VM} during helminth infection.
(**A**) UMAP visualization of concatenated spleen $CD8^+$ T cells analyzed by flow cytometry. FlowSOM clustering analysis was applied based on the fluorescence signals of CD3, CD8, CD44, CXCR3, CD49d, CD124, and CD22. Histograms show the expression levels of the given marker in each cluster.
(**B**) UMAP visualization of concatenated spleen $CD8^+$ T cells analyzed by flow cytometry. Color scale indicates relative expression for each marker.
(**C**) Split UMAP visualization of concatenated spleen $CD8^+$ T cells analyzed by flow cytometry. IL-4Rα negative ($CD124^–$) population is indicated by the dashed area. The area surrounded in red highlights $CD22^+$ events (cluster 0).
(**D**) Representative flow cytometry analysis of concatenated samples (n=5) for CD22 expression in $CD4^+$ and $CD8^+$ T cells in the mesLN of WT C57BL/6 mice at day 15 after *H. polygyrus* infection. Numbers indicate percent of events in each gate.
(**E**) Analysis EOMES expression in $CD22^+CD8^+$ T cells in spleen and mesLN of IL-$4R\alpha^{WT}$ and IL-$4R\alpha^{\Delta CD8}$ BALB/c mice at day 4 after PBS or IL-4c treatment, or at day 15 after *H. polygyrus* infection. Symbols indicate results from each individual mouse.
(**F**) Summary data of T_{VM} and $CD22^+$ T_{VM} percentages and numbers in the spleen of C57BL/6 WT mice after IL-4c and at day 15 after *H. polygyrus* infection.
(**G**) $CD22^+$ T_{VM} percentages in the spleen of *H. polygyrus*-infected WT C57BL/6 mice at different time points post-infection.
(**H**) $CD22^+$ T_{VM} percentages in the mesLN, spleen, inguinal LN, and bone marrow of WT C57BL/6 mice at day 15 after *H. polygyrus* infection.
(**I**) Persistence of T_{VM} and $CD22^+$ T_{VM} over time after one i.p. injection of IL-4c and day 0.
(**J**) Percentages and absolute numbers of spleen and thymic $CD22^+$ T cells after IL-4c treatment (2× at 2 days interval, analysis at day 4).
(**K**) WT BALB:B mice were infected with 10^4 PFU of MuHV-4-Luc intranasally, and treated with IL-4c (2× at 2 days interval) at day 30 after infection. Data show representative flow cytometry analysis and summary data of CD22 expression in spleen T_{VM} or in $D^bORF6^{487\text{-}495}$ and $K^bORF61^{524\text{-}531}$ MuHV-4-specific $CD8^+$ T cells. Numbers in gates indicate percentage of CD22 positive events. Scatter plots show mean ± s.e.m. are shown.
Statistical significance calculated using two-way analysis of variance (ANOVA) and Tukey's (E,K) or Sidak's (H,J) multiple comparisons test or one-way ANOVA with Dunnet's (F,I) or Dunn's (G) multiple comparisons test. Data are representative of three independent experiments with 3-5 mice per group (mean ± s.e.m.).

Figure S6. Unconventional activation of CD22^{+} T$_{VM}$ by IL-4.

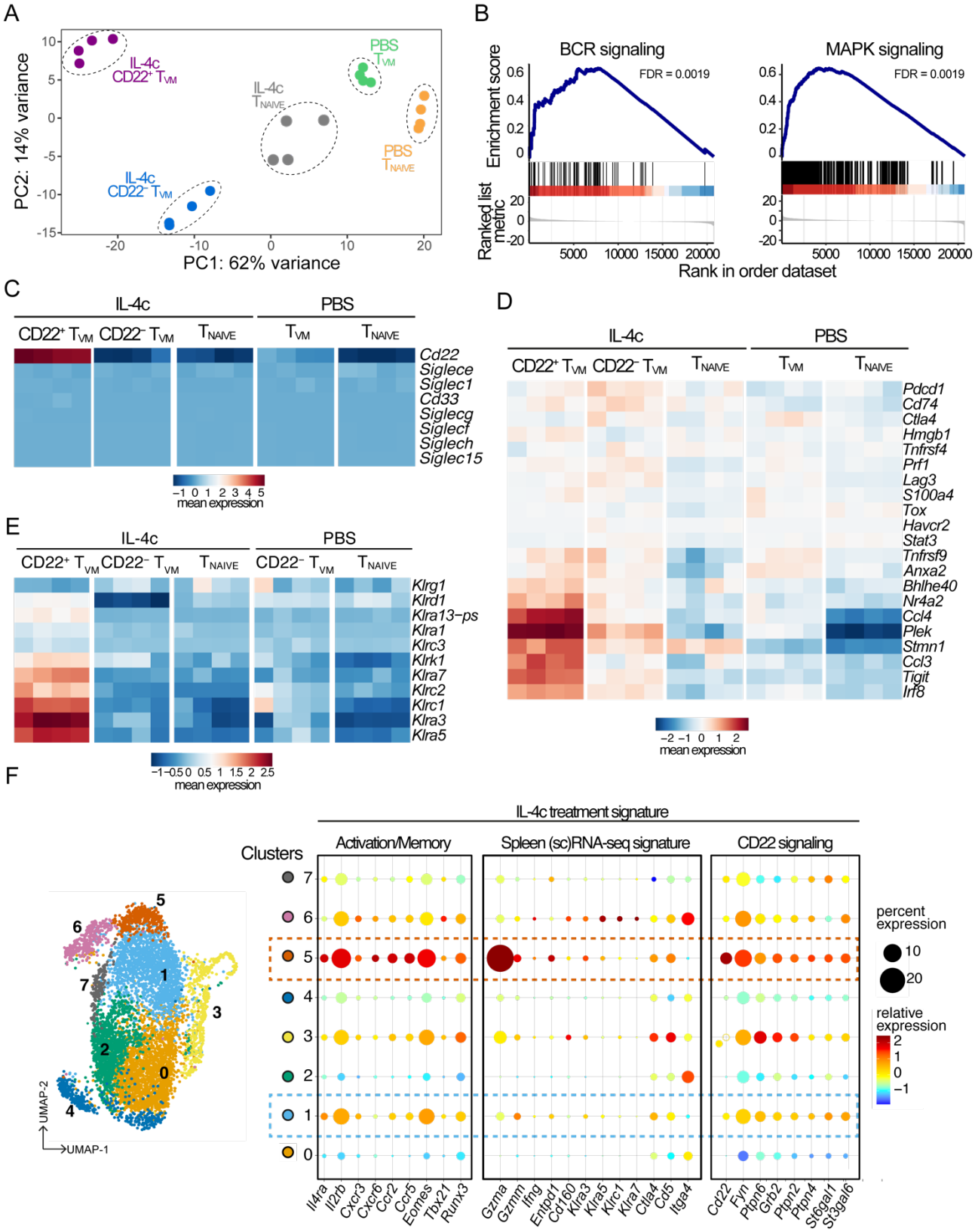

Figure S6. Unconventional activation of CD22^{+} T_{VM} by IL-4.
(**A**) Principal component analysis of the RNA-seq analysis on sorted CD44^{low} T_{NAIVE} and CD22^{-} and CD22^{+} CD44^{high}CD49d^{low} T_{VM} upon PBS or IL-4c treatment.
(**B**) GSEA enrichment score plots for the indicated KEGG gene sets between CD22^{-} and CD22^{+} T_{VM} in IL-4c treated mice.
(**C**) Heatmap of Siglec-encoding gene expression in *Mus musculus*. Color scale indicates normalized mean expression.
(**D**) Heatmap of curated T cell exhaustion gene expression. Color scale indicates normalized mean expression.
(**E**) Heatmap of gene expression of killer cell lectin-like receptor subfamily members (*Klr*). Color scale indicates normalized mean expression.
(**F**) Dot plot showing the average expression levels and percentage of expression of selected genes in each cluster from scRNA-seq experiment performed on mesLN CD124^{+} and CD124^{-} CD8^{+} T cells at day 15 after *H. polygyrus* infection, as depicted in Fig. 4 and Fig. S4. Selected genes are indicated by blocks based on signature genes identified in bulk RNA-seq on splenic CD22^{+} T_{VM} after IL-4c treatment, and genes involved in CD22 signaling in B lymphocytes.

Figure S7. Mechanisms of IL-4-driven CD22$^+$ T_{VM} expansion.

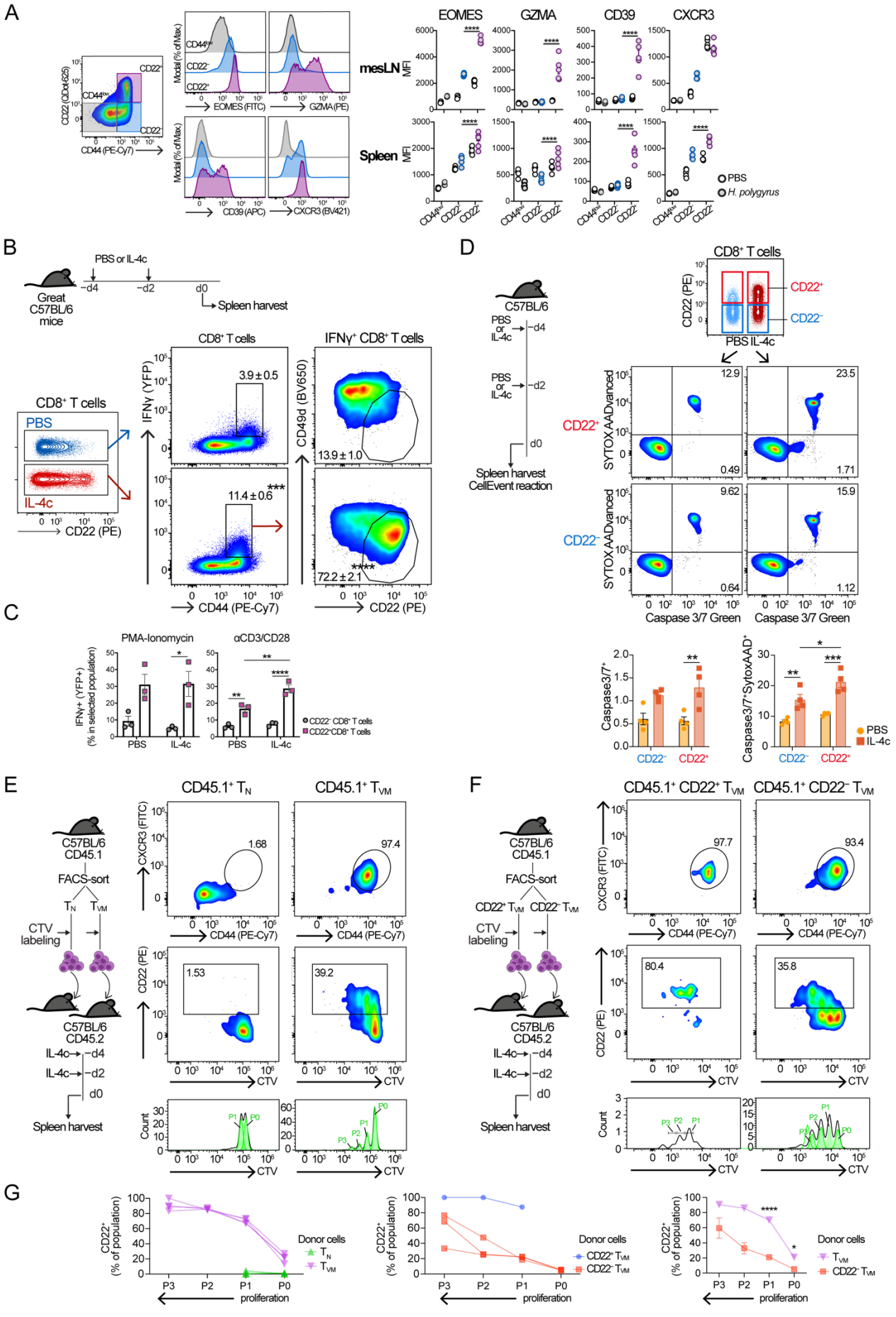

Figure S7. Mechanisms of IL-4-driven CD22^{+} T_{VM} expansion.
(**A**) Representative flow cytometry analysis of concatenated samples and summary data of the MFI of selected markers in mesLN CD44^{low} T_{NAIVE}, CD22^{-} T_{VM} and CD22^{+} T_{VM} of WT BALB/c mice at day 15 after infection with *H. polygyrus* (n=4-5).
(**B**) Representative flow cytometry analysis of concatenated samples revealing IFN-γ expression by eYFP detection in Great mice (n=3). Numbers in gates indicate mean percent of events (± s.e.m.). Data are representative of two independent experiments.
(**C**) Summary data of IFN-γ^{+} (eYFP^{+}) as in (F) upon restimulation with PMA and ionomycin or anti-CD3/CD28. Data are representative of two independent experiments.
(**D**) Representative flow cytometry analysis of concatenated samples showing CellEvent activated Caspase 3/7 and SYTOX-AADvanced dead cell stainings in CD8^{+} T cells and CD22$^{+/-}$ T_{VM} after PBS or IL-4c treatment (n=4). Numbers in gates indicate mean percent of events. Summary data of activated caspase 3/7^{+}SYTOX^{-} CD22$^{+/-}$ T_{VM} and caspase 3/7^{+}SYTOX^{+} CD22$^{+/-}$ T_{VM}.
(**E-G**) CD44^{low} naïve CD8^{+} T cells and CD49d^{low}CD44^{high} T_{VM} (E) or CD22^{+} T_{VM} and CD22^{-} T_{VM} (F) were FACS-sorted from naïve CD45.1 mice, labeled with CellTrace Violet (CTV) and transferred intravenously into CD45.2 recipient C56BL/6 mice before IL-4c treatment. Representative flow cytometry analysis of concatenated samples is shown (n= 3-4; except n=1 for CD22^{+} T_{VM} transfer). Numbers in gates indicate mean percent of events. Proliferation peaks were determined using the proliferation modeling tool in FlowJo software.
(**G**) Summary data of percents of CD45.1^{+} CD22^{+} T_{VM} cells in proliferating population as defined in (E) and (F).
Statistical significance calculated using two-way analysis of variance (ANOVA) and Tukey's (A,C,D) or Sidak's multiple (G) comparisons test (*$P < 0.05$, **$P < 0.01$, ***$P < 0.001$, ****$P < 0.0001$).

Figure S8. Activation of CD22$^+$ T_{VM} is IL-4Rα/STAT6-dependent but microbiota independent.

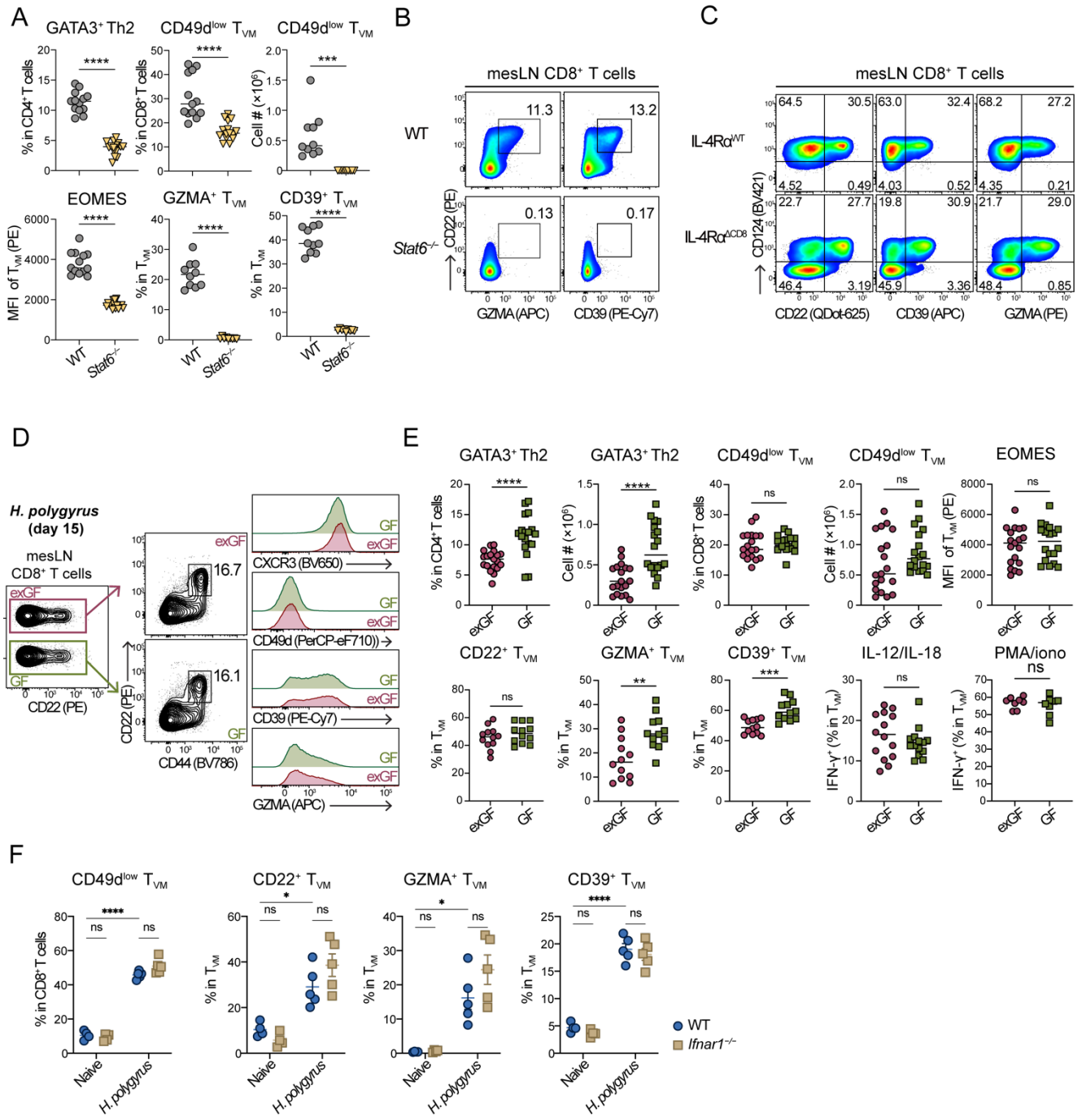

Figure S8. Activation of CD22^{+} T_{VM} is IL-4Rα/STAT6-dependent but microbiota independent.
(**A**) Summary data of GATA3^{+} Th2 and T_{VM} responses in mesLN of C57BL/6 WT and *Stat6*$^{-/-}$ mice at day 15 after infection with *H. polygyrus* (pooled data from 3 independent experiments, n=4-5).
(**B**) Representative flow cytometry analysis of concatenated samples for the co-expression of CD22 and GZMA and CD39 in mesLN of C57BL/6 WT and *Stat6*$^{-/-}$ mice at day 15 after infection with *H. polygyrus* (n=5).
(**C**) Representative pseudocolour flow plots of concatenated CD8^{+} T cells from mesLN of IL-4Rα^{WT} and IL-4Rα$^{\Delta CD8}$ BALB/c mice at day 15 after *H. polygyrus* infection. Numbers indicate percent of events in each quadrant (n=5).
(**D**) Representative flow cytometry analysis of concatenated samples revealing CD22 expression by T_{VM}, and coexpression of the indicated markers as shown by the histograms in mesLN of exGF and GF C57BL/6 mice at day 15 after infection with axenic *H. polygyrus* (n=5).
(**E**) Summary data of GATA3^{+} Th2 and T_{VM} responses in mesLN of exGF and GF C57BL/6 mice at day 15 after infection with axenic *H. polygyrus* (pooled data from 3 independent experiments, n=4-5).
(**F**) Summary data of T_{VM} responses in *Ifnar1*$^{-/-}$ mice at day 15 after *H. polygyrus* infection (n=5).
Statistical significance calculated using unpaired t test (A,E) or two-way analysis of variance (ANOVA) and Tukey's multiple comparisons test (F). Data are representative of 2 to 3 independent experiments including 3 to 5 mice per group (mean ± s.e.m.).

Figure S9. Diverse TCR repertoire in IL-4-induced CD22^{+} T_{VM} is enriched in self-reactive CDR3 sequences.

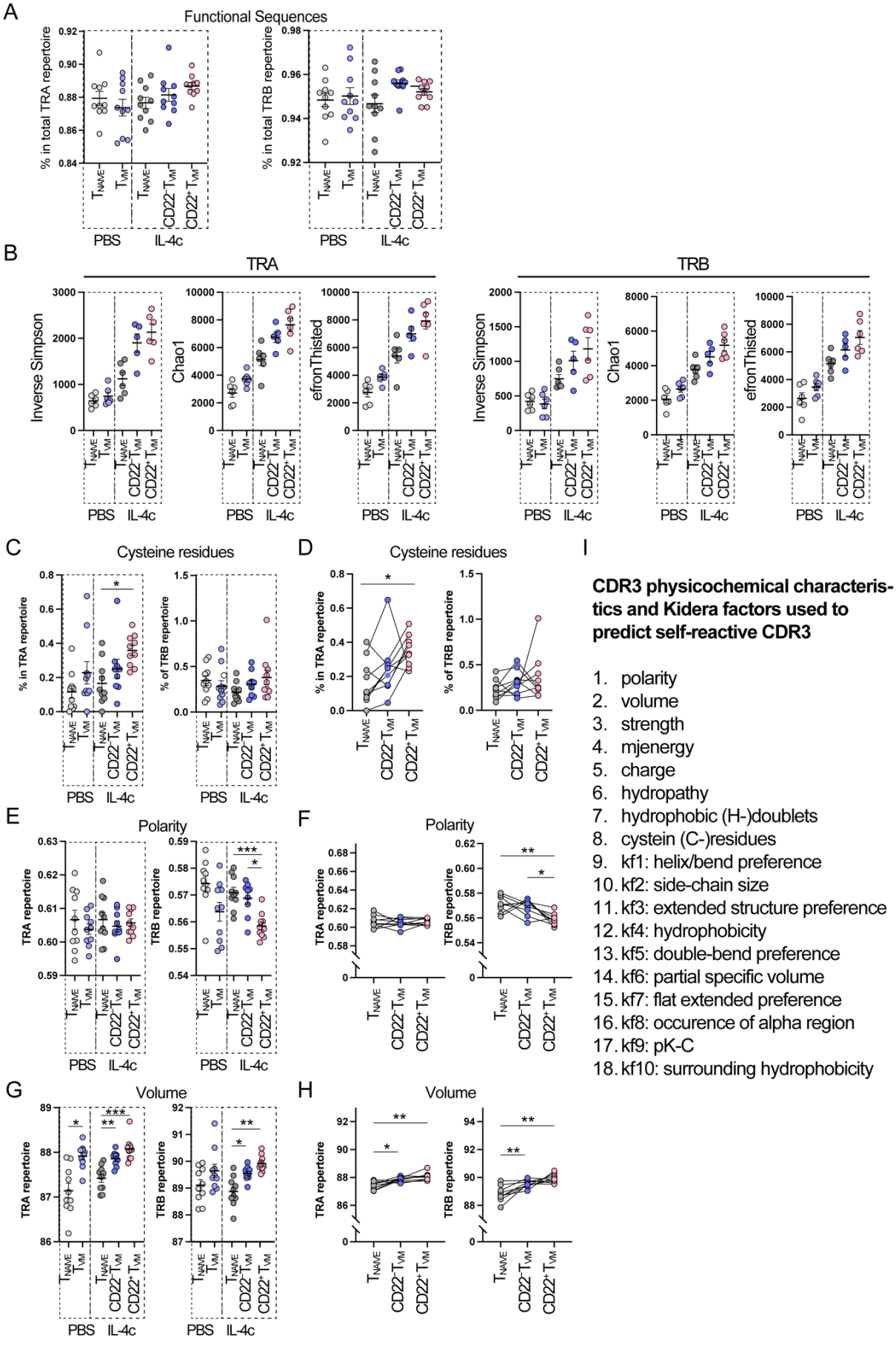

I

CDR3 physicochemical characteristics and Kidera factors used to predict self-reactive CDR3

1. polarity
2. volume
3. strength
4. mjenergy
5. charge
6. hydropathy
7. hydrophobic (H-)doublets
8. cystein (C-)residues
9. kf1: helix/bend preference
10. kf2: side-chain size
11. kf3: extended structure preference
12. kf4: hydrophobicity
13. kf5: double-bend preference
14. kf6: partial specific volume
15. kf7: flat extended preference
16. kf8: occurence of alpha region
17. kf9: pK-C
18. kf10: surrounding hydrophobicity

Figure S9. Diverse TCR repertoire in IL-4-induced CD22^{+} T_{VM} is enriched in self-reactive CDR3 sequences.

CD44^{low} T_{NAIVE}, CD22^{-} CD44^{high}CD49d^{low} T_{VM} and CD22^{+} CD44^{high}CD49d^{low} T_{VM} were purified by FACS from the spleen of PBS or IL-4c-treated WT BALB/c mice. CDR3α and CDR3β sequences were extracted from RNA-seq and TCR-seq.

(**A**) Summary plots of functional CDR3 sequences retrieved from the RNA-seq and TCR-seq experiments. Each symbol represents an individual mouse (n=10).

(**B**) Summary plots of inverse Simpson, Chao1 and efronThisted diversity indexes of TRA and TRB for the different T cell subsets in PBS- or IL-4c-treated mice. Each symbol represents an individual mouse. Data show CDR3α and CDR3β sequences obtained by TCR-seq. Mean ± s.e.m. is indicated (n=6).

(**C-D**) Summary plots of enrichment of cysteine residues of the central amino acids in CDR3α and CDR3β repertoire of the different T cell subsets in PBS- or IL-4c-treated mice (D) or of paired samples in IL-4c-treated mice (F).

(**E-F**) Summary plots of CDR3 polarity based on the presence of bulky amino acid side chains of CDR3α and CDR3β repertoire of the different T cell subsets in PBS- or IL-4c-treated mice (E) or of paired samples in IL-4c-treated mice (F).

(**G-H**) Summary plots of CDR3 volume based on the presence of bulky amino acid side chains of CDR3α and CDR3β of the different T cell subsets in PBS- or IL-4c-treated mice (G) or of paired samples in IL-4c-treated mice (H).

(**I**) CDR3 physicochemical characteristics used in Fig. 7H.

Statistical significance calculated using one-way analysis of variance (ANOVA) and Tukey's (B,D,F,H) or Dunnet's (C,E,G) multiple comparisons test.

Data are representative of two independent experiments including 4 to 6 mice per group (mean ± s.e.m.).

Figure S10. T_{VM} response in absence of CD22.

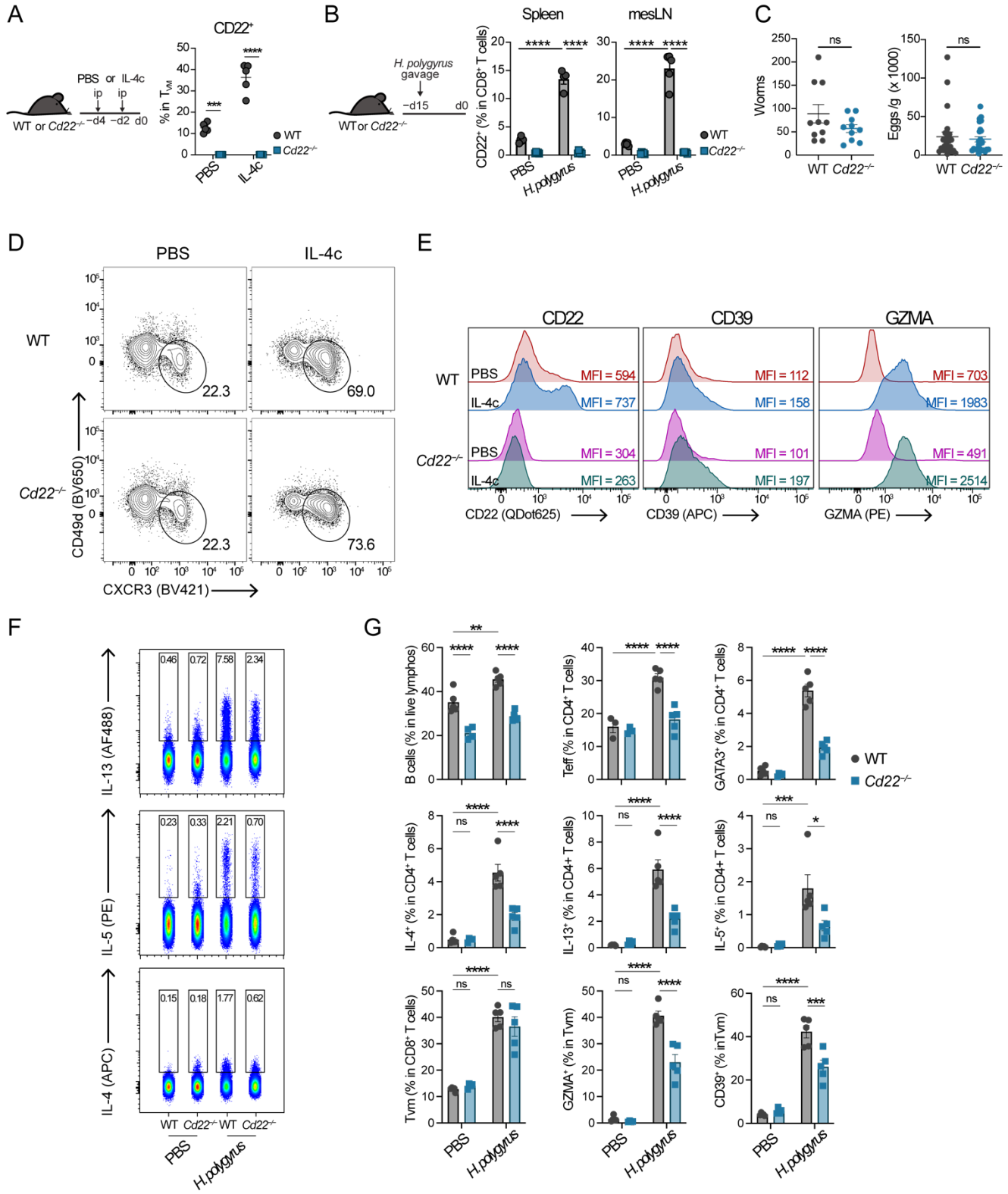

Figure S10. T_{VM} response in absence of CD22.
(**A**) WT or *Cd22*$^{-/-}$ mice treatment with IL-4c. Summary data of CD22^{+} CD8^{+} T cell percentages. Bar indicates mean ± s.e.m.
(**B**) WT or *Cd22*$^{-/-}$ mice were infected with *H. polygyrus* (200 × L3) by gavage and samples analysed at day 15 after infection. Summary data of CD22^{+} CD8^{+} T cell percentages. Bar indicates mean ± s.e.m.
(**C**) WT or *Cd22*$^{-/-}$ mice were infected with *H. polygyrus* (200 × L3) by gavage. *H. polygyrus* adult worm burden in the gut of WT and *Cd22*$^{-/-}$ mice at day 15 after infection, and fecal egg counts between day 10 and day 14 after infection.
(**D**) Contour plots of concatenated samples (n=5) of spleen samples from WT or *Cd22*$^{-/-}$ mice treated with PBS of IL-4c. Numbers indicate the percent of CD49d^{low}CXCR3^{+} T_{VM} cells in each gate.
(**E**) Half-off-set histograms adjusted to mode of concatenated samples (n=5) showing the fluorescence intensities of the indicated markers upon analysis by flow cytometry on spleen cells from WT or *Cd22*$^{-/-}$ mice treated with PBS of IL-4c. Numbers indicate median fluorescence intensities (MFI).
(**F-G**) WT or *Cd22*$^{-/-}$ mice were infected with *H. polygyrus* (200 × L3) by gavage. At day 15 after infection, mesLN were harvested and Th2 and T_{VM} responses analyzed by flow cytometry. Pseudocolour plots of concatenated samples (n=5) of CD4^{+} T cells show percentage of IL-13^{+}, IL-5^{+} and IL-4^{+} CD4^{+} T cells for each experimental condition (PBS or *H. polygyrus*) and for each mouse genotype (F). Summary data of the percentages of the indicated populations in the mesLN at 15 days after *H. polygyrus* infection (G).
Statistical significance calculated using Mann Whiney test (C) or one-way analysis of variance (ANOVA) and Tukey's multiple comparison test (A,B,G). Data are representative of 2 to 3 independent experiments including 3 to 6 mice per group (means ± s.e.m.).

Figure S11. Functional contribution of CD22^{+} T$_{VM}$ in competitive bone marrow chimeric mice.

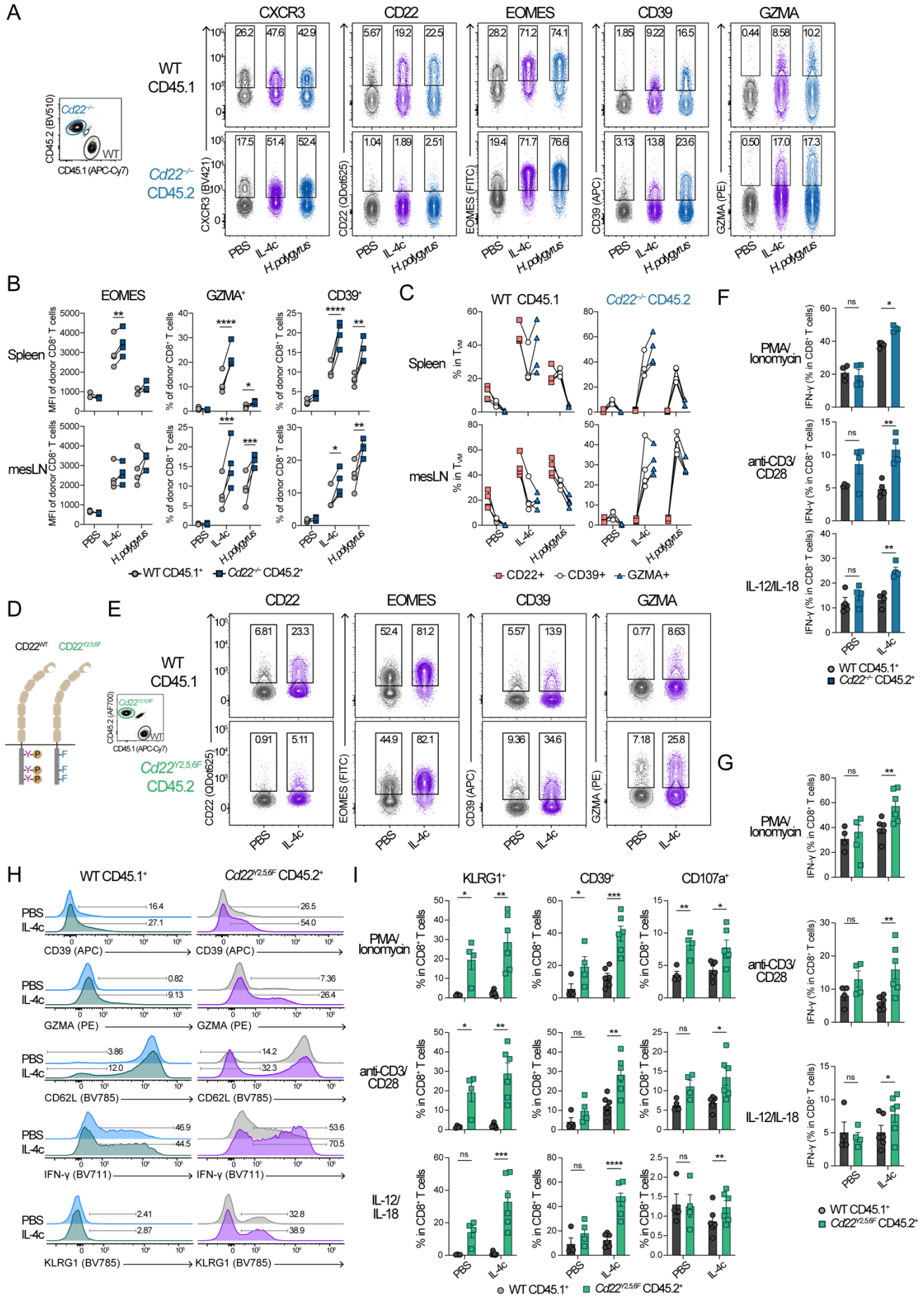

Figure S11. Functional contribution of CD22$^+$ T_{VM} in competitive bone marrow chimeric mice.
(**A)** Contour flow plots of CD8$^+$ T cells from mesLN of mixed bone marrow WT:*Cd22*$^{-/-}$ chimeric mice. Plots show concatenated samples of 4 mice per group, separated by experimental condition. Numbers indicate percent of events in each gate for each experimental condition (PBS, IL-4c or *H. polygyrus* at day 15 after infection).
(**B**) Summary data of EOMES median fluorescence intensity, percentage of GZMA$^+$ and CD39$^+$ cells in CD8$^+$ T cells from the spleen and mesLN of mixed bone marrow WT: *Cd22*$^{-/-}$ chimeric mice after treatment with IL-4c or infection with *H. polygyrus*.
(**C**) Summary data obtained from the spleen and mesLN of individual mixed bone marrow WT: *Cd22*$^{-/-}$ chimeric mice showing the co-expression of CD22, CD39 and GZMA.
Statistical significance calculated using two-way analysis of variance (ANOVA) and Sidak's multiple comparison test (ns, not significant, $^{**}P < 0.01$, $^{***}P < 0.001$, $^{****}P < 0.0001$). Each symbol represents an individual mouse. Data are representative of 2 independent experiments.
(**D**) Schematic representation of WT CD22 (CD22^{WT}) and CD22^{Y2,5,6F} knock-in.
(**E**) Contour flow plots of CD8$^+$ T cells from the spleen of mixed bone marrow WT:*Cd22*^{Y2,5,6F} chimeric mice. Plots show concatenated samples of 4 to 6 mice per group, separated by experimental condition. Numbers indicate percent of events in each gate for each experimental condition (PBS or IL-4c).
(**F**) Mixed bone-marrow WT:*Cd22*$^{-/-}$ chimeric mice were treated with PBS or IL-4c and spleen cells subjected to PMA and ionomycin, anti-CD3ε/CD28 or IL-12 and IL-18 stimulation *ex vivo*. Plots show the quantification of the percentages of IFN-γ$^+$ cells in CD8$^+$ T cells following the indicated *ex vivo* stimulation.
(**G**) Mixed bone-marrow WT:*Cd22*^{Y2,5,6F} chimeric mice were treated with PBS or IL-4c and spleen cells subjected to PMA-ionomycin, anti-CD3ε/CD28 or IL-12 and IL-18 stimulation *ex vivo*.
Plots show the quantification of the percentages of IFN-γ$^+$ cells in CD8$^+$ T cells following the indicated *ex vivo* stimulation.
(**H**) Half-off-set histograms adjusted to mode of concatenated samples (n=4 to 6) showing the fluorescence intensities of the indicated markers upon analysis by flow cytometry on spleen cells from WT:*Cd22*^{Y2,5,6F} chimeric mice. Data for IFN-γ and KLRG1 are from spleen cells restimulated with PMA and ionomycin. Bars indicate positive population set on isotype control. Numbers indicate percent of positive population.
(**I**) Summary data of the percentage of KLRG1$^+$, CD39$^+$ and CD107a$^+$ cells in CD8$^+$ T cells following the indicated *ex vivo* stimulation in WT:*Cd22*^{Y2,5,6F} chimeric mice.
Statistical significance calculated using one-way analysis of variance (ANOVA) and Sidak's multiple comparison test. Data are representative of 2 to 3 independent experiments including 3 to 6 mice per group (means ± s.e.m.).

Figure S12. Regulatory functions of CD22^{+} T$_{VM}$.

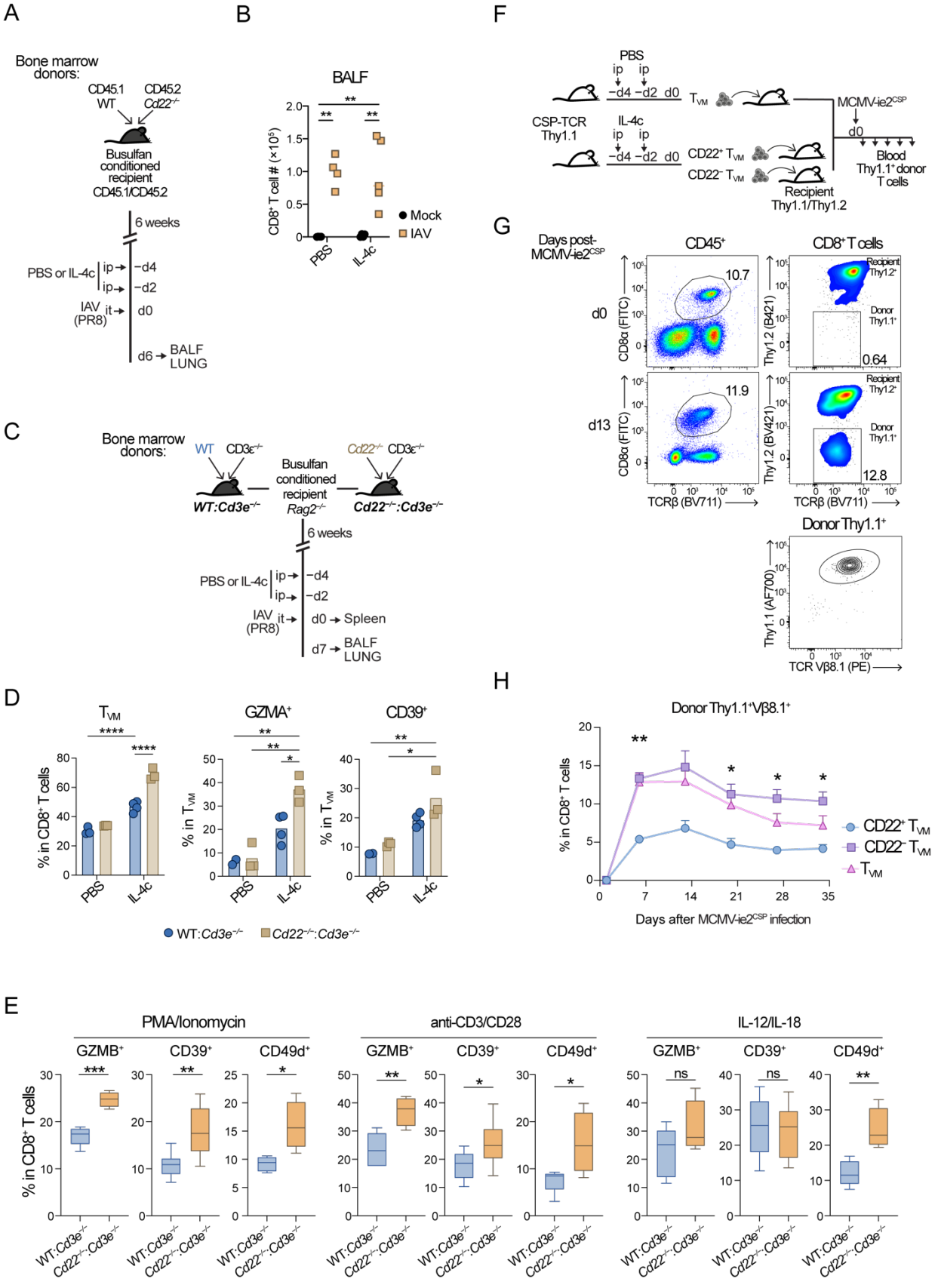

Figure S12. Regulatory functions of CD22$^+$ T_{VM}.
(**A-B**) Mixed bone marrow WT:*Cd22*$^{-/-}$ chimeric mice were treated with PBS or IL-4c before IAV infection intratracheally (25 PFU) and BALF and lung cells harvested at day 6 after IAV infection. (A) Experimental layout. (B) Absolute numbers of CD8$^+$ T cells collected from the airway (BALF) of mock-infected mice or mice at day 6 after IAV infection.
(**C-E**) Mixed bone marrow WT:*Cd3e*$^{-/-}$ and *Cd22*$^{-/-}$:*Cd3e*$^{-/-}$ chimeric *Rag2*$^{-/-}$ mice were treated with PBS or IL-4c before IAV infection intratracheally (25 PFU) and BALF and lung cells harvested at day 7 after IAV infection. (C) Experimental layout. (D) Quantification of T_{VM} percentages and GZMA$^+$ or CD39$^+$ T_{VM} in the spleen after IL-4c treatment. (E) Lung cells were isolated at day 7 after IAV infection and subjected to PMA-ionomycin, anti-CD3ε/CD28 or IL-12 and IL-18 stimulation *ex vivo*. Summary data of GZMB$^+$, CD39$^+$, and CD49d^{high} CD8$^+$ T cells are shown as box and whiskers.
(**F-H**) T_{VM} from naïve and CD22$^{+/-}$ T_{VM} from IL-4c-treated CSPTg-TCR Thy1.1 mice were FACS-sorted and transferred intravenously (10,000 cells per mouse) before infection with MCMV-ie2^{CSP} virus (5×10^5 plaque-forming units per mouse, intraperitoneally) and monitoring of anti-CSP Thy1.1$^+$ CD8$^+$ T cell responses over time. (F) Experimental layout. (G) Gating strategy to identify circulating Thy1.1$^+$Thy1.2$^-$ CSP-TCRtg cells upon MCMV-ie2^{CSP} infection. (H) Quantification of Thy1.1$^+$Vβ8.1$^+$ cells after T-cell transfer and MCMV-ie2^{CSP} viral infection.
Statistical significance calculated using one-way analysis of variance (ANOVA) and Tukey's (B, H) or Sidak's (D) multiple comparisons test or unpaired t test (E). Data are representative of 2 to 3 independent experiments including 3 to 6 mice per group (means ± s.e.m.).

Table S1. List of antibodies used in this study

Target	Clone	Format	RRID
BD Biosciences			
CD3ε	145-2C11, 17A2	APC-Cy7, V450	AB_396759, AB_10679120
CD183	CXCR3-173	BV421, PE	AB_268755, AB_10897140
CD8α	53-6.7	BUV615	AB_2870272
CD49d	R1-2	BV650, BV786	AB_2740185, AB_2738789
CD124	mIL4R-M1	PE, BV421	AB_10894018, AB_2739619
CD195	C34-3448	BV711	AB_2741681
CD62L	MEL-4	FITC, BV785	AB_394665, AB_2738598
CD4	GK1.5	BUV395	AB_2738426
CD44	IM7	BV786	AB_2738395
EOMES	X4-83	Alexa-Fluor 488	AB_2916486
Biolegend			
CD3ε	145-2C11, 17A2	Purified, APC	AB_312666, AB_312676, AB_2561455
KLRG1	2F1	BV786	AB_2629749
TCRβ	H57-597	BV711	AB_2629564
CD8α	53-6.7	FITC, APC, APC-Fire750, BV605, BV785	AB_312744, AB_312750, AB_11218801, AB_2572113, AB_2562609
CD44	IM7	PE-Cy7	AB_830786
CD183	CXCR3-173	FITC, APC	AB_2566565, AB_1088993
CD124	I015F8	APC	AB_2750451
CD39	Duha59	APC, PE-Cy7	AB_2750320, AB_2563393
CD4	GK1.5	FITC, APC	AB_312690, AB_312696
CD24	M1/69	APC-Fire 750	AB_2650876
CD25	PC61	FITC	AB_312854
CD28	37.51	Purified	AB_312866
CD45.1	A20	BV421, APC-Cy7, APC, Alexa-Fluor 700	AB_10896425, AB_313504, AB_313502, AB_493732
CD45.2	104	BV510, PE-Cy7, Alexa-Fluor 700	AB_2561393, AB_1186103, AB_493730
CD45RB	C363-16A	APC	AB_2565229
CD90.1	OX-7	APC, Alexa-Fluor 700	AB_1595470, AB_1626241
CD90.2	53-2.1	BV421	AB_2686992
CD122	TM-β1	APC-Cy7	AB_2750454
CD192	SA203G11	BV650	AB_2721553
CD160	7H1	PerCP-Cy5.5	AB_2562676
TCR Vβ8.1, 8.2	MR5-2	PE	AB_10639942
Ly-49C/F/I/H	14B11	FITC	AB_2254372
IFN-γ	XMG1.2	BV711, PE	AB_11219588, AB_315401
GZMA	3G8.5	PE	AB_2565309
GZMB	QA16102	PE	AB_2687031
CD107a	1D4B	PerCP-Cy5.5	AB_2572055
TotalSeq anti-mouse hashtag antibodies (A0301 to A0305)	M1/42; 30-F11	Purified	AB_2750032, AB_2750033, AB_2750034, AB_2750035, AB_2750036
Ultra-LEAF anti-interleukin-4	11B11	Purified	AB_11149679
CD16/CD32	clone 93	Purified	AB_312800
ThermoFisher			
CD45.2	104	eFluor450	AB_11042125
TCRβ chain	H57-597	APC-eF780	AB_1272173
CD49d	R1-2	PerCP-710, PE	AB_11150051, AB_465697
CD4	RM4-5	Alexa Fluor 700	AB_494000
CD44	IM7	PE	AB_465664
GZMA	3G8.5	APC	AB_2573228
IFN-γ	XMG1.2	Alexa Fluor 488, APC	AB_469932, AB_469504
EOMES	Dan11mag	PE, PE-eFluor610	AB_1603275, AB_2574614
GATA3	TWAJ	Alexa Fluor 488, PerCP-710	AB_2574493, AB_10804487
Interleukin-4	11B11	APC	AB_469494
Interleukin-5	TRFK5	BV421	AB_2563161
Interleukin-13	eBio13A	Alexa Fluor 488	AB_2016708
Miltenyi			
CD22	Cy34.1	PE, Biotin	AB_2656372, AB_2656376

Table S2. List of reagents used in this study

Reagents or materials	Company name	Catalog number
5-Ethynyl-2′-deoxyuridine (EdU)	ThermoFisher Scientific	A10044
Click-iT Plus EdU Pacific Blue Flow Cytometry Assay Kit	ThermoFisher Scientific	C10636
CellEvent Caspase-3/7 Green Flow Cytometry Assay Kit	ThermoFisher Scientific	C10740
CellTrace Violet Cell Proliferation Kit, for Flow Cytometry	ThermoFisher Scientific	C34571
10X RBC Lysis Buffer	Biolegend, eBioscience	420301, 00-4300-54
β-mercaptoethanol	ThermoFisher Scientific	31350010
Collagenase A	Roche	10103578001
DNAse	Roche	11284932001
Busulfan (1,4-dimethanesulfonate 1,4-butanediol)	Cayman Chemical	14843
DMEM	ThermoFisher Scientific	10566016
IMDM	ThermoFisher Scientific	31980030
10X Non-essential amino acids	ThermoFisher Scientific	11140050
Penicillin-Streptomycin (10,000U/mL)	ThermoFisher Scientific	15140122
L-1-tosylamido-2-phenylethyl chloromethyl ketone	Thermo Fisher Scientific	227800010
Trypsin-EDTA	ThermoFisher Scientific	15400054
EDTA, 0.5M	Sigma-Aldrich	E8008
HBSS	ThermoFisher Scientific	24020117
DPBS, no calcium, no magnesium	ThermoFisher Scientific	14190144
Fetal Calf Serum	ThermoFisher Scientific	A5256701
Foxp3/Transcription Factor Staining Buffer Set	ThermoFisher Scientific	00-5523-00
Paraformaldehyde	Sigma-Aldrich	158127
Saponin	Sigma-Aldrich	84510-100G
Brefeldin A	Biolegend	420601
Monensin	Biolegend	420701
Phorbol 12-myristate 13-acetate (PMA)	Biotechne - Tocris	1201/1
Ionomycin	Biotechne - Tocris	1704/1
MojoSort Mouse CD4 T Cell Isolation Kit	Biolegend	480006
MojoSort Mouse CD8 T Cell Isolation Kit	Biolegend	480008
K_2EDTA	Sigma-Aldrich	03660
Bovine serum albumin	Merck	A2153-100G
Recombinant mouse IL-4 (carrier-free)	Biolegend	574308
Recombinant Murine IL-12 (p70) (carrier-free)	Biolegend	577004
Recombinant Murine IL-18 (carrier-free)	Biolegend	767004
Isoflutek (Isoflurane)	Alivira	/
IVISbrite D-Luciferin Potassium Salt	Revvity	122799-5
RNAeasy Micro Kit	Qiagen	74104
QIAamp DNA Mini Kit	Qiagen	51304
Taq DNA Polymerase with Standard *Taq* Buffer	New England biolabs	M0273X
inNucleotide Set (dNTPs)	iST InnuScreen	845-AS-1100250
Ethanol absolute	VWR	20821.296
iQ SYBR Green Supermix	Biorad	1708880
Chromium Next GEM Single Cell 3' Kit	10X Genomics	PN-1000268
SMART-seq HT cDNA synthesis kit	Takara	634456
Mouse Immune Single-Cell Multiplexing Kit	BD Biosciences	633793
BD Rhapsody Enhanced Cartridge Reagent kit	BD Biosciences	633887
Rhapsody Cartridge Kit	BD Biosciences	633733
Rhapsody cDNA Kit	BD Biosciences	633773
BD Rhapsody WTA Amplification Kit	BD Biosciences	633801